universität wien

MASTERARBEIT / MASTER'S THESIS

Titel der Masterarbeit / Title of the Master's Thesis

„Simulation and Design of the High Voltage Post-acceleration Electrode for NoMoS “

verfasst von / submitted by

Raluca Maria Jiglău, BSc

angestrebter akademischer Grad / in partial fulfilment of the requirements for the degree of

Master of Science (MSc)

Wien, 2020 / Vienna, 2020

Studienkennzahl lt. Studienblatt / degree programme code as it appears on the student record sheet:	A 066 876
Studienrichtung lt. Studienblatt / degree programme as it appears on the student record sheet:	Masterstudium Physik
Betreut von / Supervisor:	Priv.-Doz. Dr. Johann Zmeskal

Abstract

The standard model of particle physics (SM) comprises our current understanding of elementary particles and fields. Precision experiments in the low energy regime, such as studies of the free neutron beta decay, are important tools for tests of the SM and searches of physics beyond.

NoMoS, the neutron decay products momentum spectrometer, is a new experiment designed to determine multiple observables from the spectra of the charged neutron decay products with high precision. It uses a novel technique of momentum spectroscopy, based on the R$\times$B effect, to separate decay electrons and protons according to their momentum.

One key component of the experimental design is the high voltage electrode required for the post-acceleration of decay protons to detectable energies. A careful design of the electrode is required to suppress systematic effects introduced by the high voltage. The aim of this thesis was to study multiple electrode geometries for the simultaneous and individual measurement of the charged decay particles based on a set of design criteria using numerical simulations.

Electrostatic potential computations were performed to evaluate systematic effects, such as the emergence of particle traps or radial inhomogeneities of the electrostatic potential. The adiabatic particle transport and E$\times$B drift effects were studied using particle-tracking simulations which rely on computations of electric and magnetic fields. Investigations performed in this thesis serve as a base for future electrode design studies.

Zusammenfassung

Das Standardmodell der Teilchenphysik (SM) umfasst unser derzeitiges Verständnis von Elementarteilchen und Feldern. Präzisionsexperimente in dem Bereich niedriger Energien, wie Studien zu dem Beta-Zerfall freier Neutronen, sind wichtige Werkzeuge für Tests des SM und für die Suche nach Erweiterungen des Modells.

NoMoS, das neutron decay products momentum spectrometer, ist ein neues Experiment für die Bestimmung mehrerer Observablen aus den Spektren der geladenen Neutronenzerfallsprodukte mit hoher Präzision. Es verwendet eine neuartige Technik der Impulsspektroskopie, die auf dem R×B-Effekt basiert, um die Zerfalls-Elektronen und Protonen nach ihrem Impuls zu trennen.

Eine Schlüsselkomponente des Experiments ist die Hochspannungselektrode, die für die Nachbeschleunigung der Zerfallsprotonen auf nachweisbare Energien erforderlich ist. Ein sorgfältiges Design der Elektrode ist erforderlich, um systematische Effekte zu unterdrücken, die von der Hochspannung induziert werden. Ziel dieser Arbeit war es, mehrere Elektrodengeometrien für die gleichzeitige und individuelle Messung der Zerfallsprodukte zu untersuchen, anhand von Designkriterien und unter Verwendung numerischer Simulationen.

Elektrostatische Potentialberechnungen wurden durchgeführt, um systematische Effekte, wie das Auftreten von Teilchen-Fallen oder Inhomogenitäten des Potentials zu untersuchen. Der adiabatischen Teilchentransport und E×B-Drifteffekte wurden mithilfe von Teilchen-Tracking Simulationen untersucht, die auf Berechnungen elektrischer und magnetischer Felder beruhen. Die in dieser Arbeit durchgeführten Untersuchungen dienen als Grundlage für zukünftige Studien des Elektrodendesign.

Contents

1 Introduction **1**

2 Theoretical Background **2**
2.1 The Neutron Beta Decay . . . 2
2.2 Motion of Charged Particles in Magnetic and Electric Fields . . . 3
2.2.1 Magnetic Field . . . 4
2.2.2 Electric and Magnetic Fields . . . 6
2.2.3 Adiabatic Particle Transport . . . 6

3 The NoMoS Experiment **8**
3.1 Measurement Principles . . . 8
3.2 Requirements for the Post-acceleration Electrode . . . 11
3.2.1 Adiabatic Particle Transport . . . 11
3.2.2 Homogeneity of the Electrostatic Potential . . . 12
3.2.3 E×B Drift Effect . . . 13
3.2.4 Particle Traps . . . 14
3.2.5 Electrostatic Potential inside the R×B Drift Region . . . 16
3.3 Simulation Tools . . . 16
3.3.1 Electric and Magnetic Fields Calculations . . . 17
3.3.2 Particle-Tracking Simulations . . . 18

4 Electrode Designs for Simultaneous Particle Measurement **19**
4.1 Possible Detector Configurations . . . 19
4.2 Geometrical and Electrical Setup of the Detection System . . . 21
4.3 Electrode Requirements Studies . . . 24
4.3.1 Proton Post-acceleration . . . 24
4.3.2 Homogeneity of the Electrostatic Potential . . . 25
4.3.3 Electrostatic Potential at large Distances from the Electrode . . . 29
4.3.4 Particle Traps . . . 30
4.3.5 E×B Drift Effect . . . 33
4.4 Summary . . . 43

5 Electrode Designs for Single Proton Measurement **46**
5.1 Possible Electrode Types . . . 46
5.1.1 Cylinder Electrode . . . 47
5.1.2 Field Degrader . . . 47
5.2 Geometrical and Electrical Setup of the Detection System . . . 49
5.3 Electrostatic Potential Studies . . . 51
5.3.1 Proton Post-acceleration . . . 51
5.3.2 Electrostatic Potential at large Distances from the Electrode . . . 52
5.3.3 Particle Traps . . . 54

5.3.4 Homogeneity of the Electrostatic Potential . . . 57
5.4 Adiabatic Particle Transport Studies . . . 62
5.4.1 Adjustments to the Cylinder Electrode . . . 66
5.4.2 Adjustments to the Field Degrader . . . 70
5.5 E×B Drift Effect Studies . . . 75
5.5.1 Adjustments to the Cylinder Electrode . . . 77
5.5.2 Adjustments to the Field Degrader . . . 81
5.6 Further Studies . . . 86
5.6.1 Proton Beam Size . . . 87
5.6.2 Proton Beam Shift . . . 88
5.7 Summary . . . 93

6 Conclusions and Outlook **96**

A E×B Drift **101**

B Particle-Tracking Simulations **103**
B.1 Particle Initialization . . . 103
B.2 Data Post-Processing . . . 104

C Electrode Setups **106**
C.1 Field Degrader . . . 106
C.2 Wire Grid Field Degrader . . . 106
C.2.1 Single Wire Grid . . . 106
C.2.2 Double Wire Grid . . . 107

D Additional Plots **110**
D.1 Magnetic Field . . . 110
D.2 Cylinder Electrode . . . 110
D.3 Wire Grid Field Degrader . . . 112
D.3.1 Transmission . . . 112
D.3.2 Electric Field . . . 112

Acknowledgements **117**

Chapter 1

Introduction

The Standard Model of particle physics (SM) is the theory that describes elementary particles (quarks and leptons) and their interaction via the electromagnetic, weak and strong force. Currently, it is the best description of subatomic particles and fields and many predictions made by the theory have been experimentally confirmed. However, multiple phenomena, such as gravity, dark matter and dark energy, neutrino oscillations and the baryon asymmetry of the universe, are not explained within the current SM. Extensions of the SM and theories beyond attempt to explain these phenomena. Measurements in both the high and low energy regime aim to search for hints of new physics.

The free neutron beta decay is a useful tool for tests of the weak interaction and for searches of physics beyond the SM. Multiple observables of the neutron decay, such as the neutron lifetime or correlation coefficients, can be derived from precision experiments in the low energy regime and can be used to determine various parameters of the SM [1]. This task has been the focus of a large variety of precision experiments, such as aSPECT [2, 3], Nab [4], aCORN [5] and many more. Existing experiments aim to measure these observables to higher precision while new experiments based on novel techniques are designed to enable a systematically independent measurement.

NoMoS , the neutron decay products momentum spectrometer, is a new experiment designed to determine several correlation coefficients of the free neutron beta decay by measuring the momentum spectra of the charge decay products [6, 7]. It uses uniformly curved magnetic fields to separate the oppositely charged decay products according to their momentum. The resulting drift distance spectra are measured on spatially resolving detectors. Decay protons are low energetic and require post-acceleration by electric fields to detectable energies. The focus of this thesis lies on the design of the high voltage post-acceleration electrode for protons, considering both the individual and simultaneous measurement of the charged decay particles.

This thesis begins with a short introduction to the theoretical background of the free neutron beta decay and on the motion of charged particles in electromagnetic fields (Chapter 2). Chapter 3 gives an overview of the experimental setup of NoMoS and its measurement principles. The main focus of this chapter lies in the derivation of crucial requirements to the design of the post-acceleration electrode for protons. Investigations of systematic effects introduced by the electrode rely on detailed computations of electromagnetic fields and particle-tracking simulations. Numerical methods used for the required simulations are, additionally, described in this chapter. In Chapters 4 and 5, multiple electrode designs for both the simultaneous and individual particle measurement, respectively, are proposed and systematic effects are evaluated based on the derived electrode design criteria. Conclusions on the feasibility of the proton measurement are presented in Chapter 6.

Chapter 2

Theoretical Background

The Standard Model of particle physics (SM) describes the free neutron beta decay in the framework of the electroweak interaction. The beta decay of the free neutron is a useful tool to test this interaction and to search for hints towards new physics. The neutron lifetime and correlation coefficients in the differential decay rate of the neutron are required to determine parameters of the SM. The NoMoS experiment aims to derive several correlation coefficients of the neutron decay from the electron and proton drift distance spectra.

A short introduction to the neutron beta decay and the correlation coefficients connected to it is given Section 2.1. The experiment utilizes magnetic and electric fields to guide the charged decay particles towards detectors and to post-accelerate the protons prior to detection. The motion of charged particles in electric and magnetic fields is described in Section 2.2.

2.1 The Neutron Beta Decay

The free neutron n decays into a proton p^+, an electron e^- and an electron-antineutrino $\overline{\nu}_\mathrm{e}$

$$\mathrm{n} \longrightarrow \mathrm{p}^+ + \mathrm{e}^- + \overline{\nu}_\mathrm{e}. \tag{2.1}$$

Fig. 2.1 shows the decay on quark level. The decay was first correctly described as a V−A (vector minus axial vector) interaction in the framework of the electroweak interaction by George Sudarshan and Robert Marshak [8] and independently by Richard Feynman and Murray Gell-Mann [9].

An expression for the differential decay rate of the neutron, which comprises multiple observables of the neutron, has been worked out in detail by Jackson *et al* [11]:

$$\begin{aligned} d^3\Gamma &= \frac{1}{(2\pi)^5}\frac{G_F^2|V_{ud}|^2}{2} p_e E_e (E_0 - E_e)^2 dE_e d\Omega_e d\Omega_\nu \\ &\times \xi\left[1 + a\frac{\boldsymbol{p_e}\boldsymbol{p_\nu}c^2}{E_e E_\nu} + b\frac{m_e c^2}{E_e} + \frac{\langle \boldsymbol{s_n}\rangle}{s_n}\left(A\frac{\boldsymbol{p_e}c}{E_e} + B\frac{\boldsymbol{p_\nu}c}{E_\nu} + D\frac{\boldsymbol{p_e}\times\boldsymbol{p_\nu}c^2}{E_e E_\nu}\right)\right]. \end{aligned} \tag{2.2}$$

Here, G_F denotes the Fermi coupling constant and V_ud is the relevant element of the Cabibbo-Kobayashi-Maskawa CKM matrix. The momenta and total energies of the electron and the electron-antineutrino are given by $\boldsymbol{p}_\mathrm{e}$, $\boldsymbol{p}_\nu$, E_e and E_ν, respectively, and E_0 denotes the electron maximum total energy. Further parameters are the electron mass m_e and the neutron spin $\boldsymbol{s}_\mathrm{n}$. Solid angles are represented by Ω_i and c is the speed of light in vacuum. The parameter a denotes the electron-antineutrino correlation coefficient and b is the Fierz interference term. Further angular correlation coefficients are A, B and D. In the SM, various correlation coefficients

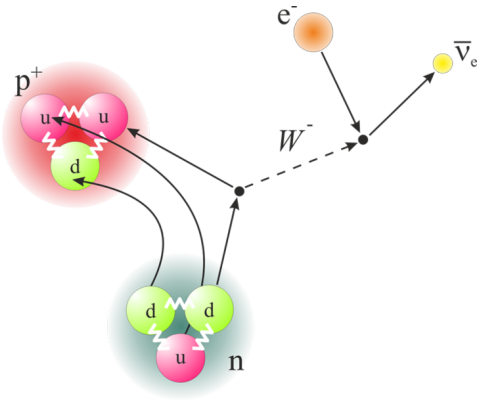


Figure 2.1: Neutron beta decay on quark level: The neutron (n) is composed of two down quarks (d) and one up quark (u). One of the two down quarks converts to an up quark by emission of a W boson. The up quark is held together with the remaining d and u quark by gluons to form a proton (p^+). The W boson decays into an electron (e^-) and electron anti-neutrino ($\overline{\nu}_\mathrm{e}$). Figure taken from [10].

in Eq. (2.2) can be expressed in terms of the ratio $\lambda = g_\mathrm{A}/g_\mathrm{V}$, where g_A and g_V denote the axial and the vector coupling constants, respectively [1]. Thus, one way to determine λ is from precise measurements of correlation coefficients present in the neutron decay rate. A significant discrepancy between the values of λ derived from precision measurements might hint to the need of an adapted theory.

The angular correlation coefficient a can be inferred from the measured proton spectrum, since it affects the shape of the spectrum [1]. The fraction of higher energetic decay protons increases if the coefficient a is positive while the opposite holds for a negative value [12]. The current average value of the correlation coefficient a is -0.1059 ± 0.0028 [13].

The Fierz interference term b vanishes in the present form of the SM. A non-zero value of b would indicate the existence of additional couplings (scalar and tensor) in the electroweak interaction. The term can be derived from the measurement of the electron spectrum [14].

The NoMoS experiment aims to determine both observables from the spectra of decay electrons and protons. It uses magnetic fields to guide the charged decay products through the spectrometer towards detectors, where the particles are measured. Electrons and protons emerge from the decay with a maximum kinetic energy of 782 keV and 751 eV, respectively [15]. Since decay protons are low energetic they require a post-acceleration by electric fields to detectable energies. The electric field is provided by the high voltage post-acceleration electrode. An understanding of the measurement principles of NoMoS and of the criteria derived for the electrode design requires a short description of the motion of charged particles in magnetic and electric fields. This is provided in the following section.

2.2 Motion of Charged Particles in Magnetic and Electric Fields

Magnetic and electric fields can be used to guide charged particles along specific paths. The trajectory followed by a particle of mass m and charge q moving in an electric field $\boldsymbol{E}$ and magnetic field $\boldsymbol{B}$ with velocity $\boldsymbol{v}$ is determined by the Lorentz force $\boldsymbol{F}_\mathrm{L}$ [16]:

$$\boldsymbol{F}_\mathrm{L}(\boldsymbol{r}) = m\frac{\mathrm{d}\boldsymbol{v}}{\mathrm{d}t} = q[\boldsymbol{E}(\boldsymbol{r}) + \boldsymbol{v}(\boldsymbol{r}) \times \boldsymbol{B}(\boldsymbol{r})]. \tag{2.3}$$

The NoMoS experiment uses static magnetic fields to guide the charged decay particles from

the point of decay towards detectors. Additionally, an electric field is required for the post-acceleration of decay protons. The motion of charged particles inside a static magnetic field (for $\boldsymbol{E}(\boldsymbol{r}) = 0$) and in static electromagnetic fields is described in Sections 2.2.1 and 2.2.2, respectively. A simple model for the transport of the decay particles inside the experiment can be constructed if the transport is adiabatic. This notion is described in more detail in Section 2.2.3.

2.2.1 Magnetic Field

NoMoS uses both uniform and curved static magnetic fields to guide and disperse decay electrons and protons. The motion of charged particles in both magnetic field environments is described in the following.

Uniform Magnetic Field

In the absence of electric fields Eq. (2.3) reduces to:

$$\boldsymbol{F}_{\mathrm{L}}(\boldsymbol{r}) = q[\boldsymbol{v}(\boldsymbol{r}) \times \boldsymbol{B}(\boldsymbol{r})]. \tag{2.4}$$

A charged particle moving in a static, uniform magnetic field experiences the force $\boldsymbol{F}_{\mathrm{L}}$, which acts on the particle in the direction perpendicular to both its velocity vector $\boldsymbol{v}$ and the magnetic field vector $\boldsymbol{B}$. The force $\boldsymbol{F}_{\mathrm{L}}$ causes the particle to gyrate around a magnetic field as it moves in the direction of the magnetic field vector B. The center of the circular orbit is referred to as the guiding center. The resulting path is helical as shown in Fig. 2.2. Note that the magnitude of the particle velocity and its total energy are constant when the particle moves in a static magnetic field [16].

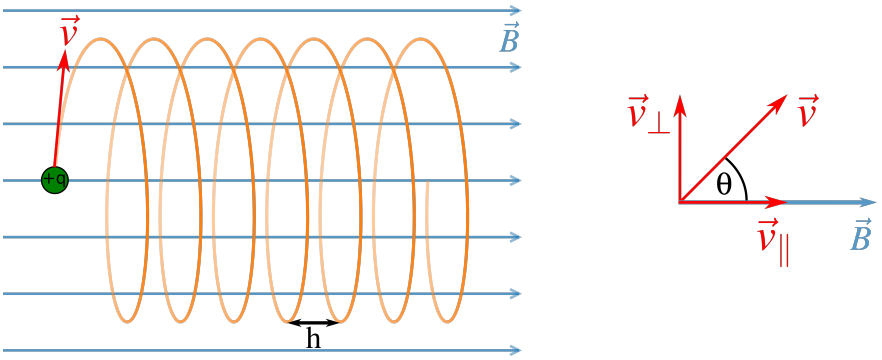


Figure 2.2: Helical trajectory of a charge q moving with velocity $\boldsymbol{v}$ in a uniform magnetic field $\boldsymbol{B}$: The magnetic force acts on the particle in the direction normal to both the particle velocity $\boldsymbol{v}$ and magnetic field $\boldsymbol{B}$. The resulting particle trajectory is helical, whit gyration radius r_{g} and pitch height h. The pitch angle θ is determined by the orientation of $\boldsymbol{v}$ relative to the magnetic field vector $\boldsymbol{B}$. The particle velocity $\boldsymbol{v}$ can be decomposed into the transversal and longitudinal velocity $\boldsymbol{v}_\perp$ and $\boldsymbol{v}_\parallel$, respectively, relative to the magnetic field vector.

The helical path can be described in terms of the radius of gyration r_{g} and the pitch height h. The gyration radius depends, among other parameters, on the transversal particle velocity $v_\perp$ and the magnetic field B[1]:

$$r_g = \frac{m \cdot v_\perp}{q \cdot B}. \tag{2.5}$$

The transversal velocity $v_\perp$ is given by:

$$v^2 = v_\parallel^2 + v_\perp^2 \tag{2.6}$$

[1]The gyration radius is obtained by assuming that the magnetic force $F_{\mathrm{L}} = qv_\perp B$ and the centripetal force $F_{\mathrm{C}} = mv_\perp^2/r_{\mathrm{g}}$, experienced by the particle when following a curved path, are equal.

and

$$v_\perp = v \sin\theta, \tag{2.7}$$
$$v_\parallel = v \cos\theta. \tag{2.8}$$

Here, v denotes the absolute particle velocity and $v_\parallel$ represents the particle velocity in the direction parallel to the magnetic field, as shown in Fig. 2.2. The particle pitch angle θ is determined by the orientation of the particle velocity vector $\boldsymbol{v}$ with respect to the magnetic field vector $\boldsymbol{B}$. The pitch height h of the helical path is defined as the distance by which the particle moved in the direction parallel to the magnetic field after one gyration:

$$h = \frac{2\pi \cdot m \cdot v_\parallel}{q \cdot B}. \tag{2.9}$$

The particle gyration radius, pitch angle and the pitch height of the helical path are constant if the charged particle moves in a static, uniform magnetic field.

The NoMoS experiment uses a uniformly curved magnetic field to disperse the charged decay particles according to their charge and momentum. The motion of charged particles moving in such a field is described in the following.

Curved Magnetic Field

Charged particles which gyrate inside a curved magnetic field experience an additional drift. The so called R×B drift effect can be described as a centrifugal acceleration of the particle guiding center which occurs when the particle tends to gyrate around a curved magnetic field line [16]. A particle of charge q moving in a magnetic field of magnitude B and local curvature radius R (see Fig. 2.3) drifts with velocity

$$\boldsymbol{v}_{\mathrm{R\times B}} \propto \frac{\boldsymbol{R} \times \boldsymbol{B}}{qR^2B^2} \tag{2.10}$$

in the direction perpendicular to both the magnetic field vector $\boldsymbol{B}$ and the curvature radius vector $\boldsymbol{R}$. Note that positively and negatively charged particles drift in opposite directions. Thus, particles can be separated based on their charge q using curved magnetic fields.

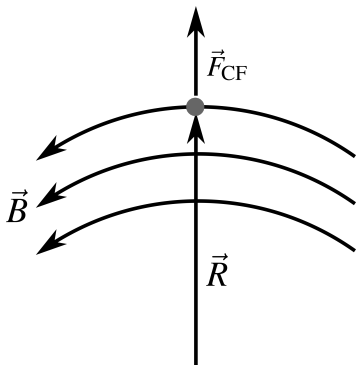


Figure 2.3: A charged particle experiences a centrifugal force $\boldsymbol{F}_{\mathrm{CF}}$ when it moves in a curved magnetic field $\boldsymbol{B}$ of local curvature radius vector $\boldsymbol{R}$. Figure adapted from [17].

In the NoMoS experiment, decay protons require additional post-acceleration by electric fields to detectable kinetic energies. The motion of charged particles moving in electromagnetic fields is shortly described in the following.

2.2.2 Electric and Magnetic Fields

The motion of a charged particle moving in electromagnetic fields is determined at any point $\boldsymbol{r}$ by the Lorentz force $\boldsymbol{F}_{\mathrm{L}}(\boldsymbol{r})$ given in Eq. (2.3). The trajectory followed by the particle depends, among others, on the orientation of the electric field vector $\boldsymbol{E}$ relative to the magnetic field vector $\boldsymbol{B}$:

- $\boldsymbol{E} \parallel \boldsymbol{B}$: The charged particle gyrates around a magnetic field line and is accelerated by the electric field in the direction of the electric field vector $\boldsymbol{E}$.
- $\boldsymbol{E} \nparallel \boldsymbol{B}$: The particle guiding center experiences an additional drift in the direction perpendicular to both the magnetic field vector $\boldsymbol{B}$ and electric field vector $\boldsymbol{E}$. The drift velocity $\boldsymbol{v}_{\mathrm{E\times B}}$ is given by [16]:

  $$\boldsymbol{v}_{E\times B} = c\frac{\boldsymbol{E}\times\boldsymbol{B}}{B^2}, \tag{2.11}$$

  with c denoting the speed of light in vacuum. Note that particles of opposite charge q drift in the same direction.

The description of the particle trajectory in terms of the guiding center is an approximation and holds under certain assumptions which are discussed in the following section.

2.2.3 Adiabatic Particle Transport

Properties of charged particles, such as kinetic energy and pitch angle, moving in electromagnetic fields can be determined analytically if the particle transport is adiabatic. The periodic motion of a gyrating charged particle can be used to construct invariants of the motion. Such an invariant is the particle magnetic moment μ, defined by the ratio between the transversal particle kinetic energy component $T_\perp$ and the magnetic field B

$$\mu = \frac{T_\perp}{B}, \tag{2.12}$$

if relative variations of the electric and magnetic fields are small within one particle gyration (adiabatic approximation) [16, 18]:

$$\frac{\Delta E}{E} \ll 1 \text{ and } \frac{\Delta B}{B} \ll 1. \tag{2.13}$$

In Eq. (2.12), the transversal energy component $T_\perp$ is given by:

$$T^2 = T_\parallel^2 + T_\perp^2 \tag{2.14}$$

where

$$T_\perp = T\sin^2\theta, \tag{2.15}$$
$$T_\parallel = T\cos^2\theta. \tag{2.16}$$

Here, T and $T_\parallel$ denote the total particle kinetic energy and the longitudinal kinetic energy, respectively. Strong variations of the magnetic and electric fields break the invariance of the magnetic moment. This causes oscillations of the particle magnetic moment with an amplitude increasing with increasing relative variations of the electric and magnetic fields [18].

In the NoMoS experiment, protons are post-accelerated by an electric field and gain kinetic energy as they gyrate towards the sensor. In the adiabatic approximation, the longitudinal kinetic

energy $T_{\parallel}(z)$ and the pitch angle $\theta_{\mathrm{ad}}(z)$ of a particle with initial kinetic energy T_0 and pitch angle θ_0 can be determined analytically at any point z of the particle trajectory using:

$$T_{\parallel}^{ad}(z) = T_0 - q(U(z) - U_0) - \frac{B(z)}{B_0} T_0 \sin^2(\theta_0) \tag{2.17}$$

and

$$\theta_{ad}(z) = \arcsin \sqrt{\frac{B(z)}{B_0} \cdot \frac{T_0 \sin^2(\theta_0)}{T_0 - q(U(z) - U_0)}}. \tag{2.18}$$

A complete derivation of the two quantities is provided in [19]. Here, U_0 and B_0 denote the electrostatic potential and magnetic field at the start of the particle trajectory while $U(z)$ and $B(z)$ represent the potential and magnetic field at any point z of the trajectory. The particle pitch angle $\theta_{\mathrm{ad}}(z)$ changes as a consequence of the particle acceleration.

The NoMoS experiment uses both uniform and curved magnetic fields to guide and disperse the charged decay products and electric fields to post-accelerate the decay protons to detectable energies. An overview of the experimental setup and a detailed discussion of the requirements for the electrode design are provided in the following chapter.

Chapter 3

The NoMoS Experiment

The NoMoS experiment aims to measure the spectra of the charged decay products of the free neutron beta decay. The charged decay products are dispersed according to their charge and momentum using the R×B drift effect, which occurs in curved magnetic fields, and are measured on spatially resolving detectors. Protons emerge from the decay with a maximum kinetic energy of 751 eV and require post-acceleration by electric fields to detectable energies. The main focus of this thesis lies on the design of the proton post-acceleration electrode for protons. The electrode should fulfill a set of design criteria and systematic effects induced by the electrode should be understood and suppressed to achieve the desired measurement sensitivity. After a short outline of the measurement principles of NoMoS in Section 3.1, a detailed discussion of multiple requirements for the electrode design is given in Section 3.2. Simulation tools used for computations of electric and magnetic fields and for particle tracking, required for systematic effects studies, are presented in Section 3.3.

3.1 Measurement Principles

An overview of the experimental setup of NoMoS is shown in Fig. 3.1. The experiment is divided in multiple areas: the decay volume, the magnetic filter and aperture, the R×B drift region and the detection region. A brief description of each area is given below.

Decay Volume

The neutron beam passes the decay volume, a region of uniform magnetic field, where a fraction of the neutrons decays isotropically into electrons (e), protons (p) and electron-antineutrinos ($\bar{\nu}_e$). A particle emerges from the decay with kinetic energy T_0, pitch angle θ_0 and phase angle φ_0. The phase angle is determined by the orientation of the particle velocity vector $\boldsymbol{v}$ with respect to the system axis x. The charged decay particles are guided by magnetic field lines from the decay volume either towards the back detector (BD), where they are measured, or towards the main part of the spectrometer.

Magnetic Filter and Aperture

A magnetic filter (MF) is used to transmit particles based on their initial pitch angle θ_0. In this region, particles move in an increasing magnetic field which changes the particle pitch angle. The magnetic field is design such that the adiabatic condition given in Eq. (2.13) is fulfilled. Hence, the particle magnetic moment is constant at every point along the particle trajectory. A relation between the transversal velocities of a particle at the point of decay, $\boldsymbol{v}_{\perp,0}$, and at any

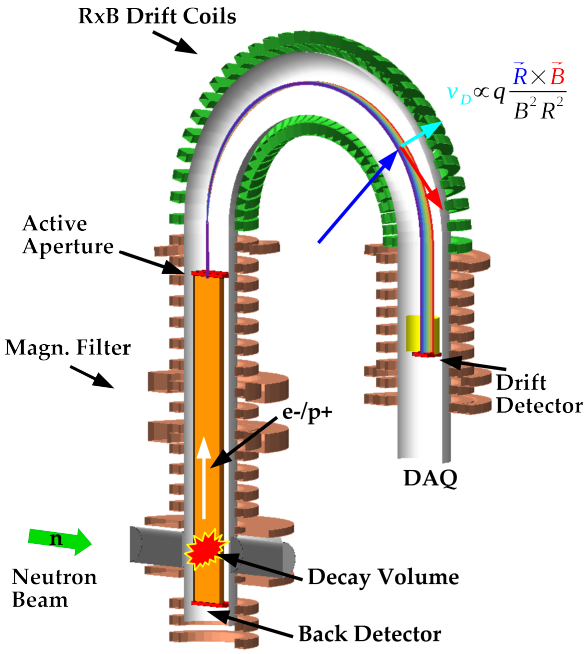


Figure 3.1: Overview of the experimental setup of NoMoS : Neutrons (n) pass the apparatus at the decay volume where a fraction of the neutrons decays into electrons (e^-), protons (p^+) and electron-antineutrinos ($\overline{\nu}_\mathrm{e}$). The charged decay products are either magnetically guided towards the main area of the spectrometer or directly measured at the back detector. Particles are selected at the magnetic filter and an aperture is used to geometrically shape the electron and proton beams. In the R×B region, electrons and protons drift in opposite directions according to their momentum and charge. The resulting drift distance spectra are measured in the detection region on spatially resolving sensors. A high voltage electrode provides the electric field required for the post-acceleration of decay protons to detectable energies. Figure courtesy of Daniel Moser.

point z in the MF region, $\boldsymbol{v}_\perp(z)$, can be derived from Eq. (2.12) using $T_\perp = mv_\perp/2$ and yields:

$$\boldsymbol{\mu} = \frac{m\boldsymbol{v}_{\perp,0}^2}{2B_0} = \frac{m\boldsymbol{v}_\perp^2(z)}{2B(z)}. \tag{3.1}$$

Here, B_0 and $B(z)$ denote the magnetic field at the point of decay and at any point z of the magnetic filter, respectively. By substituting $v_\perp$ from Eq. (2.7) into Eq. (3.1), the relation between the magnetic fields and the particle pitch angles θ_0 and $\theta(z)$ can be derived:

$$\frac{B(z)}{B_0} = \frac{\sin^2\theta(z)}{\sin^2\theta_0}. \tag{3.2}$$

It can be seen that the particle pitch angle $\theta(z)$ increases with the magnetic field. This results in an increase of the transversal particle velocity $v_\perp(z)$. On the other hand, Eq. (2.6) and conservation of momentum yield a decrease of the longitudinal velocity $v_\parallel(z)$. Hence, as the particle moves in the direction of increasing magnetic field more of the longitudinal particle motion is converted into rotational motion [16]. A particle is magnetically reflected by the magnetic field if $v_\parallel$ decreases to zero and, subsequently, changes sign. Only particles with an initial pitch angle θ_0 smaller than the critical angle θ_c are transmitted at the filter. The critical angle can be derived from Eq. (3.2) at the point of reflection, i.e., when $\theta(z) = \frac{\pi}{2}$,

$$\theta_c < \arcsin\left(\sqrt{\frac{B_\mathrm{F}}{B_0}}\right), \tag{3.3}$$

with B_{F} denoting the maximum strength of the magnetic field at the filter. In the current design of the experiment, $B_{\mathrm{F}} = 2B_0$ and, thus, only particles with initial pitch angles up to 45° are transmitted at the magnetic filter. Particles that are reflected by the magnetic field are guided towards the back detector. Transmitted particles are guided by a decreasing magnetic field towards the aperture. The field gradient causes a decrease of the particle pitch angle as dictated by Eq. (3.2). The initial pitch angle is restored if the magnetic fields at the decay point and aperture are equal, as in the current design of the experiment. The aperture is used to shape the electron and the proton beam geometrically.

R×B Drift Region

The particles are guided from the aperture towards a region of curved magnetic field. Here, decay electrons and protons are spatially separated according to their momentum and charge using the R×B drift effect described in Section 2.2.1. The particles drift with a drift velocity $\boldsymbol{v}_{\mathrm{R\times B}}$ as given by Eq. (2.10). Assuming a constant drift velocity, the distance by which the particles have drifted at the end of the R×B region can be obtained by integrating $\boldsymbol{v}_{\mathrm{R\times B}}$ over time and yields [6]:

$$D_{R\times B} \propto \frac{p}{qB}. \tag{3.4}$$

The drift distance is linear in the particle momentum p and it is indirectly proportional to the magnetic flux density B and charge q. At the end of the R×B region, decay electrons and protons have drifted in opposite directions by a distance proportional to their momentum. An example of the resulting drift momentum spectra is shown in Fig. 3.2 for a magnetic field of 200 mT and under the assumption of the current average values derived for the correlation coefficient a and the Fierz interference term b (see also Section 2.1) [20]. This figure shows, additionally, the effect of a positive coefficient a and a non-zero term b on the shape of the proton and electron spectra, respectively.

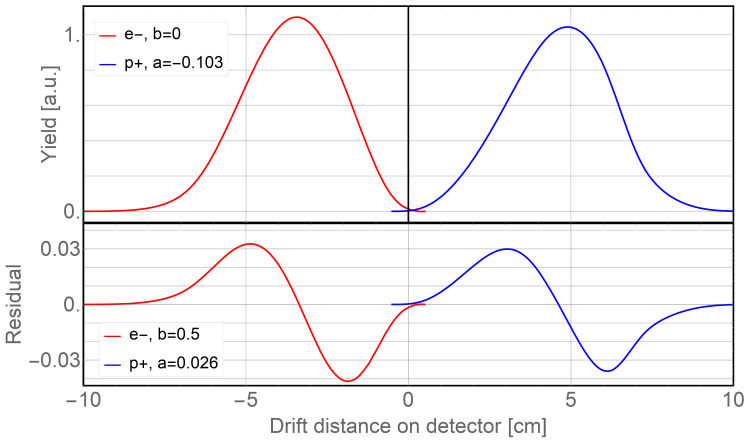


Figure 3.2: Drift distance spectra: Electrons and protons drift in opposite directions as they gyrate inside the curved magnetic field present in the R×B drift region. The decay particles drift by a distance proportional to their momentum. Note that the two spectra overlap at the central axis z. This region corresponds to low energetic electrons and protons. Figure courtesy of Daniel Moser.

Detection Region

The charged decay products are guided through the detection region towards spatially resolving detectors by a uniform magnetic field. Decay electrons have energies in the order of keV and can be directly measured on the electron detector. Decay protons are, however, low energetic and require post-acceleration by an electric field to penetrate the sensor and to generate a measurable signal. The electric field is provided by the high voltage post-acceleration electrode, which surrounds the proton detector. The required final proton energy is determined by the mean free path of the particles inside the detector material. Post-acceleration potentials used in comparable experiments lie in the range of $-10\,\mathrm{kV}$ to $-30\,\mathrm{kV}$ [2, 4, 5].

The NoMoS experiment yields multiple options for the measurement of the electron and proton drift distance spectra. The two spectra can be measurement simultaneously, either on a common detector surface or on spatially separated sensors, or individually. The aim of this thesis are studies of several geometries of the proton post-acceleration electrode both in the context of the simultaneous and single particle measurement and of systematic effects introduced by the electrode. These effects, combined with requirements for the electrode design, are discussed in the following section.

3.2 Requirements for the Post-acceleration Electrode

The goal of NoMoS is to measure the drift distance spectra of electrons and protons emitted in the neutron decay. The electrostatic potential (and, thus, the electric field) generated by the post-acceleration electrode should shift the proton spectrum to detectable energies. However, it should not introduce systematic effects which significantly change the spatial distribution of the proton and electron spectra. Such effects need to be understood and suppressed to achieve the desired precision in the determination of the neutron observables mentioned in Section 2.1. A list of requirements for the electrode design considered in this thesis is given below:

- Adiabatic particle transport
- Homogeneity of the electrostatic potential
- Suppression of E×B drift effects
- Omission of particle traps
- Vanishing electrostatic potential inside the R×B drift region

A detailed description of each electrode requirement and its influence on the charged decay particles is given in the following.

3.2.1 Adiabatic Particle Transport

The particle transport inside the detection region should be adiabatic. This enables an analytical description of particle properties, such as kinetic energy and pitch angle, as mentioned in Section 2.2.3. The electric field induced by the post-acceleration electrode and the magnetic field used to guide the particles towards the detector require a careful design to achieve good adiabaticity conditions. The longitudinal kinetic energy and the pitch angle of a particle moving in an electromagnetic field can only be evaluated analytically if spatial variations of the electric and magnetic fields experienced by the particle over one gyration period are small. The fields should, therefore, fulfill the adiabatic conditions

$$\frac{\Delta E}{E} \ll 1, \ \frac{\Delta B}{B} \ll 1 \tag{3.5}$$

within one particle gyration.

The following quantities are analyzed using particle-tracking simulations to determine if the particle transport is adiabatic:

- $\Delta E/E$ and $\Delta B/B$: Relative spatial variations of the electric and magnetic fields are evaluated after each gyration period of a tracked proton. This method is, however, limited to low energetic protons which follow trajectories of large gyration radii (and, thus, pitch angles) and small pitch heights.

- $\Delta T_\parallel/T_\parallel^{\mathrm{ad}}$ and $\Delta\theta/\theta_{\mathrm{ad}}$: Non-adiabatic effects are reflected in deviations of the longitudinal kinetic energy $T_\parallel^{\mathrm{traj}}$ and pitch angle θ_{traj} of a tracked proton from the adiabatic quantities $T_\parallel^{\mathrm{ad}}$ and θ_{ad} introduced in Eqs. (2.17) and (2.18).

- $\Delta r_{\mathrm{g}}/r_{\mathrm{g}}$: The particle gyration radius r_{g} is constant at every point of the particle trajectory if the adiabatic conditions Eq. (3.5) are fulfilled. The particle gyration radius r_{g} comprises both particle properties mentioned above and is useful for investigations of further systematic effects. Relative changes of the particle gyration radius are evaluated along the particle trajectory and at the detector with respect to the gyration radius at the start of the trajectory.

The construction of an effective model of the particle transport requires thorough investigations of the quantities mentioned above in dependence of multiple initial properties of the decay protons. To reduce the complexity of the model, such dependencies should be small.

3.2.2 Homogeneity of the Electrostatic Potential

The homogeneity of the electrostatic potential in radial cross sections of the proton beam is one important aspect of the electrode design. It ensures an adiabatic transport of both the decay protons and of protons which backscatter at the sensor and, thus, enables an analytical description of multiple particle properties. The following requirement should be fulfilled by the electrostatic potential generated by the post-acceleration electrode:

- Variations of the electrostatic potential in (preferably) every radial plane traversed by decay protons (and electrons) should be sufficiently small.

Inhomogeneities in radial cross sections of the proton beam can be estimated by the quantity:

$$\Delta U_{\mathrm{rel}}(z) = \frac{U(r,z) - U(r_{\mathrm{ref}},z)}{U(r_{\mathrm{ref}},z)}. \tag{3.6}$$

Here, $U(r,z)$ and $U(r_{\mathrm{ref}},z)$ denote the electrostatic potentials at the radial coordinate r and at the center of the proton beam r_{ref} evaluated at the axial coordinate z.

As already mentioned, a homogeneous radial potential is additionally required for backscattered protons. Particle backscattering occurs when a particle reaches the detector but does not deposit all its energy inside the detector material and is, subsequently, reflected. The backscattering probability of a particle depends on its kinetic energy and pitch angle (impact angle) as well as on the detector composition and geometry. Particles with large pitch angles and low energies have a higher probability of being backscattered. A backscattered proton gyrates away from the detector in the direction of increasing electrostatic potential, induced by the post-acceleration electrode, and experiences a deceleration. The backscattered proton is reflected by the electrostatic potential back towards the detector if its longitudinal velocity decreases to zero and, subsequently, changes sign. Protons with identical longitudinal kinetic energy, which backscatter from different positions on the sensor, are reflected in the same radial plane if the particle

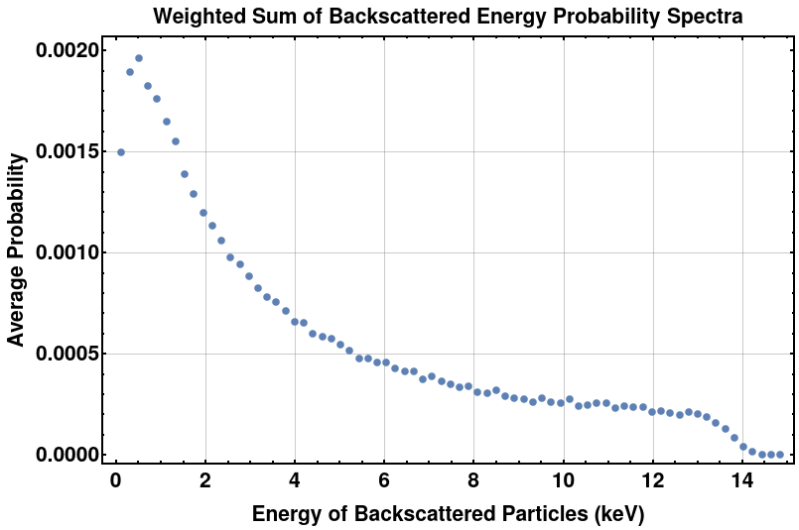


Figure 3.3: Energy probability distribution of protons which are backscattered on a sensor for a post-acceleration potential $U = -15\,\mathrm{kV}$. Simulation performed by Waleed Khalid using IMSIL for a detector composed of 15 nm of aluminum on top of silicon. Figure courtesy of Waleed Khalid.

transport is adiabatic and radial variations of the electrostatic potential are sufficiently small. Under these assumptions, the location of the particle guiding center on the sensor at re-entry could be described analytically. The particle position at the sensor can be than reconstructed from the guiding center using the particle gyration radius and phase angle. The latter depends on the total number of pitch heights performed by the particle from the sensor to the plane of reflection and back. Non-adiabatic effects and E×B drifts might change the particle trajectory significantly causing the particle to re-enter the sensor at a position that is not representative of that particle's energy. To minimize such effects, it is required that:

- The electrostatic potential induced by the electrode should be designed such that the distance covered by a backscattered proton from the detector to the point of reflection is small.

The plane of reflection depends on the longitudinal kinetic energy of the backscattered proton, assuming adiabatic conditions. The energy probability distribution of the backscattered particles is shown in Fig. 3.3 for a post-acceleration potential of $-15\,\mathrm{kV}$. It can be seen that the probability of a decay proton of being backscattered is small. Backscattered protons have the largest probability to leave the sensor with kinetic energies in the order of 0.5 keV.

3.2.3 E×B Drift Effect

The electric field generated by the high voltage post-acceleration electrode should not introduce systematic effects which change the spatial distribution of the proton (and electron) drift distance spectrum. Such an effect is the E×B drift of the particle guiding center which can occur when the particle is moving in non-aligned electric and magnetic fields (see Section 2.2.2). Protons might either be measured at a detector position which is not representative of that particle energy or might even miss the detector if they drift by significant amounts. This affects the measurement sensitivity. The post-acceleration electrode and, thus, the electric field should be designed as to fulfill the following condition:

- The E×B drift effect needs to be understood and suppressed to preserve the spatial distributions of the electron and proton drift distance spectra. Thus, the post-acceleration

electrode should generate a uniform electric field which is predominantly aligned with the magnetic field, especially in the regions covered by the decay protons.

This condition additionally ensures that drifts experienced by the decay protons do not depend significantly on initial particle properties, such as kinetic energy or pitch angle.

An approximation of the distance $D_{\mathrm{E\times B}}$ by which the guiding center of a particle of mass m and charge q drifts inside the detection region can be derived from the drift velocity $\boldsymbol{v}_{\mathbf{E\times B}}$ given in Eq. (2.11). A complete derivation is provided in Appendix A and yields:

$$D_{\mathrm{E\times B}} = c \cdot \frac{1}{B_{\mathrm{z}}} \cdot \frac{E_{\perp}}{\sqrt{\frac{2[T_0 - q(U-U_0)]}{m}}} \cdot \Delta s \cdot \hat{\mathbf{e}}_x. \tag{3.7}$$

Here, $E_{\perp}$ and $B_{\parallel}$ denote the normal electric field and the axial magnetic field, T_0 is the initial particle kinetic energy and U_0 and U represent the electrostatic potential at the initial particle position and at the detector, respectively. Further parameters are the speed of light c and the distance Δs by which a particle with longitudinal velocity $v_{\parallel}$ has drifted in the direction of the magnetic field vector $\boldsymbol{B}$. The magnitude of the magnetic field is denoted by B_{z}[1]. Note that the derived quantity $D_{\mathrm{E\times B}}$ does not account for the initial particle pitch angle θ_0. Additionally, changes in the longitudinal particle velocity due to E×B drift effects are assumed to be sufficiently small. This equation can be used to approximate the distance by which the particles drift without requiring particle-tracking simulations.

In particle-tracking simulations, E×B drifts experienced by protons can be estimated at the end of the particle trajectory as follows. Protons are tracked inside the detection region both in the presence and in the absence of electric fields. E×B drifts of the particle guiding center are estimated by the quantity:

$$D^{\mathrm{gc}}_{\mathrm{E\times B}} = \sqrt{\Delta x^2_{\mathrm{gc}} + \Delta y^2_{\mathrm{gc}}} \tag{3.8}$$

which denotes the distance by which the particle guiding center has drifted in the presence of the electric field, compared to the case where the electric field is turned off. The quantities

$$\Delta x_{\mathrm{gc}} = x^{\mathrm{on}}_{\mathrm{gc}} - x^{\mathrm{off}}_{\mathrm{gc}}, \tag{3.9}$$

$$\Delta y_{\mathrm{gc}} = y^{\mathrm{on}}_{\mathrm{gc}} - y^{\mathrm{off}}_{\mathrm{gc}}, \tag{3.10}$$

are evaluated at the end of the trajectory of a particle moving inside the detection region using the guiding center position coordinates in the presence of the electric field ($x^{\mathrm{on}}_{\mathrm{gc}}$, $y^{\mathrm{on}}_{\mathrm{gc}}$) and in its absence ($x^{\mathrm{off}}_{\mathrm{gc}}$, $y^{\mathrm{off}}_{\mathrm{gc}}$). The coordinates of the particle guiding center at the end of the trajectory can be reconstructed from the final particle velocities v_{x} and v_{y}, as described in Appendix B.2.

3.2.4 Particle Traps

Specific combination of electric and magnetic fields can confine the motion of charged particles to a particular region of space. Such particle traps can lead to a loss in the number of detected charged decay particles and to generation of background effects. The decay electrons and protons can ionize rest gas molecules through elastic and inelastic collisions. The particle traps considered in this thesis are especially relevant for ionized background particles. A careful design of the electromagnetic field in the NoMoS experiment is required to avoid the formation of particle traps. Additionally, good vacuum conditions are required to reduce the probability of collisions between the decay particles and residual gas molecules and to achieve the desired measurement sensitivity. Two trapping mechanisms which are relevant for the NoMoS experiement are studied in this thesis:

[1] A uniform magnetic field is assumed, which points in axial direction z.

- Penning trap: This type of trap is relevant for particles which are ionized inside the trap. It occurs when the electrostatic potential has an extremum with the opposite sign of the interacting charged particle along a magnetic field line.
- Electromagnetic trap: Charged particles can be trapped between the detection region and the magnetic filter if they are reflected by the negative electrostatic potential generated by the electrode and, subsequently, by the increasing magnetic field at the filter.

The two types of traps are described in more detail in the following.

Penning Trap

The mechanism of a Penning trap is described in the following for positively charged particles[2]. Fig. 3.4 illustrates a Penning trap. A decay electron can interact with a rest gas molecule inside the potential valley. In this process, an electron might be emitted from the rest gas molecule and a positively charged ion is left behind. The ion is trapped inside the valley if its kinetic energy is smaller than the trap depth $\Delta U = |U_{\mathrm{max}} - U_{\mathrm{min}}|$. A region of positive space charge can form if a large amount of positively charged ions accumulates inside the trap. This can lead to fluctuations in the local electrostatic potential environment and, eventually, to a discharge of the Penning trap.

Trapped ions can be a source of background and, thus, affect the measurement sensitivity. A trapped ion might gain sufficient kinetic energy by collision with protons (or electrons), escape the trap and experience an acceleration towards the sensor where it might leave a measurable signal. Photons and electrons can also be emitted from (inside) the Penning trap and contribute to additional background.

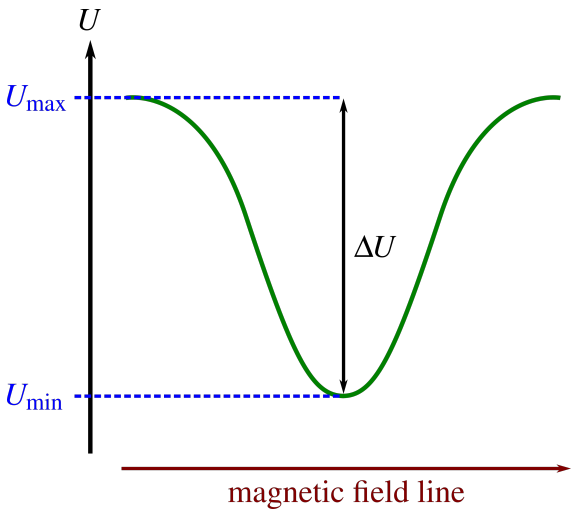


Figure 3.4: Illustration of a Penning trap for positively charged particles: A positively charged particle might be confined to a region of space if the electrostatic potential has a minimum along the magnetic field line followed by the particle. The depth of the Penning trap is estimated by the quantity $\Delta U = |U_{\mathrm{max}} - U_{\mathrm{min}}|$.

[2]The trapping mechanism is analogous for negatively charged particles if the minimum and maximum potentials U_{min} and U_{max} are interchanged.

Electromagnetic Trap

An electromagnetic trap for charged particles can occur between the detection region and the magnetic filter and might affect the measurement sensitivity. This type of trap occurs if charged particles are reflected by the decreasing electrostatic potential present inside the detection region and have a pitch angle larger than the critical angle θ_{c} (see Eq. (3.3)) when they encounter the magnetic filter. This electromagnetic trap is most relevant for ionized particles which result from collisions between the charged decay products and rest gas molecules. However, decay electrons might also be trapped if their pitch angle changes as a result of collisions with rest gas molecules and are reflected at the filter. If a charged particle is reflected between the two regions multiple times, it experiences large drifts inside the R×B drift region and, eventually, hits the vacuum tube. A careful design of the electrode-detector system is required to minimize the fraction of decay electrons reflected by the electrostatic potential inside the detection region.

3.2.5 Electrostatic Potential inside the R×B Drift Region

The amount of R×B drift experienced by a particle in a curved magnetic field is linear in the particle momentum (see Eq. (3.4)). The electrostatic potential and the electric field generated by the post-acceleration electrode in the R×B drift region should be sufficiently small to avoid influencing effects (such as the acceleration of the decay particles or E×B drift effects) during the R×B drift. This conditions translate into the following requirement:

- The electrostatic potential U induced by the electrode at the interface between the detection region and the R×B drift region should not exceed $-10\,\mathrm{mV}$.

This condition is used to determine the minimum length required for the detection region. To do so, the maximum axial distance d_{f} between the electrode and the radial plane, where $U = -10\,\mathrm{mV}$ is fulfilled, is evaluated. The following requirement should be fulfilled in the design of the detection region:

- The detection region should be short ($\approx 1\,\mathrm{m}$) to facilitate the design of a homogeneous magnetic field and to reduce the number of required coils and, thus, manufacturing costs.

In the process of the electrode design, numerical computations are used to simulate the electrostatic potential and electric field generated by the post-acceleration electrode inside the detection region and to study the various systematic effects presented in this chapter. The following section gives an overview over the methods and software used to compute electric and magnetic fields and to track particles inside the system.

3.3 Simulation Tools

The design of the post-acceleration electrode for NoMoS and investigations of systematic effects rely on detailed computations of the electric field generated by the electrode inside the detection region. Additionally, tracking of particles in the static electromagnetic field present in this region is required for the study of effects, such as E×B drifts and the adiabatic transport of decay protons. Since the geometry of the post-acceleration electrode and coils can become complex, numerical simulations are used to approximate the induced electric and magnetic fields in regions of interest. The Finite Element Method (FEM) and the Boundary Element Method (BEM) are two techniques suited for numerical simulations of electromagnetic fields and are used by a large variety of software. Simulations presented in this thesis are performed using COMSOL Multiphysics® [21] and multiple software packages developed by F. Glück in the scope of the

KATRIN experiment [22, 23]. This section provides a short description of electric and magnetic field calculations using FEM and BEM (Section 3.3.1) and of the software used for particle-tracking simulations (Section 3.3.2).

3.3.1 Electric and Magnetic Fields Calculations

Electric and magnetic fields are described in the framework of electromagnetism using partial differential equations. The FEM and BEM are used to approximate electric and magnetic fields present in the detection region of NoMoS from an input geometry (e.g., electrodes and coils) and from the physical quantities (e.g., electrostatic potentials and current densities) assigned to each component. Both techniques use a discretization of the input geometry into either finite elements (FEM) or boundary elements (BEM).

In the FEM, field computations require a discretization ("meshing") of the full volume taken up by the user-defined geometry into finite elements. Finite elements are geometrical shapes, such as triangles or tetrahedrals, which contain nodes. The physical quantity of interest is computed only at element nodes while the value inside the finite element is obtained by interpolation of nodal values. Convergence tests have to be conducted to avoid inaccurate results which arise if the mesh is not chosen fine enough. The discretization of the full volume and the requirement of a fine mesh can result in a large computational time.

In contrast, BEM uses for field calculations only a discretization of the two-dimensional surface (boundary) of the input geometry into boundary elements. This reduces the dimensionality of the problem to be studied. The physical quantity of interest at an arbitrary point outside the boundary is determined from contributions of each boundary element. As in the FEM, a fine enough discretization is required to obtain accurate results.

For electrostatic potential and electric field computations performed in this thesis, both numerical methods are used. The methods used for electromagnetic field computations, which partially rely on the BEM, and for particle-tracking simulations are described in detail in [23, 22, 24, 25]. These methods are summarized in the following and descriptions closely follow those provided in the references mentioned above.

Electric Field Computations

To compute the electrostatic potential and electric field generated by the electrode inside the detection region, the electrode surface is divided into N boundary elements, each with a charge density σ_j. These charge densities need to be determined to obtain the electrostatic potential at an arbitrary point outside the boundaries of the input electrode. Each charge density σ_j induces a potential U_i at the center of an element i. The latter is determined by the electrostatic potential applied at a given electrode segment in the input. These two quantities are related by the following equation:

$$U_i = \sum_{j=1}^{N} C_{ij}\sigma_j. \tag{3.11}$$

Thus, the Coulomb matrix elements C_{ij}, which are defined as

$$C_{ij} = \frac{1}{4\pi\epsilon_0}\int_{a_j} \frac{d^2\boldsymbol{x}_j}{|\boldsymbol{x}_i - \boldsymbol{x}_j|}, \tag{3.12}$$

need to be computed to determine the charge density σ_j of element j. Finally, the electrostatic potential generated by the electrode at an arbitrary point outside the electrode boundary can be obtained by summing over the contributions from all computed charged densities. The electric field is obtained by derivation of the calculated electrostatic potential.

Magnetic Field Computations

The software used for computations of magnetic fields was designed for axially symmetric coil geometries and is described in detail in [24]. In the NoMoS experiment, the magnetic field required for the guiding of the decay particles towards the detector inside the detection region is provided by a set of cylindrical coils. The coils are divided into small elements with current I. Each element is described by the element of length $d\boldsymbol{l}$, which points in the direction of the current I, and contributes to the determination of the magnetic field. The magnetic field $d\boldsymbol{B}$ induced by each element at a point $\boldsymbol{x}$ can be obtained using Biot-Savart's law [16]:

$$d\boldsymbol{B} = \frac{\mu_0 I}{4\pi} \frac{d\boldsymbol{l} \times \boldsymbol{x}}{x^3}. \tag{3.13}$$

The magnetic field components B_x, B_y and B_z at a point $\boldsymbol{x}$ can be computed analytically using Eq. (3.13) combined with either the elliptic integral method or the zonal harmonic method (based on Legendre polynomial expansion).

3.3.2 Particle-Tracking Simulations

Investigations of systematic effects introduced by the post-acceleration electrode, such as E×B drifts and non-adiabatic effects, rely on particle-tracking simulations. For studies performed in this thesis, protons are tracked in combined electric and magnetic fields inside the detection region. A short description of the methods used to calculate exact particle trajectories is provided in the following. A complete description of the numerical methods used by this software package is provided in [23].

The motion of a charged particle of mass m moving in an electric field $\boldsymbol{E}$ and magnetic field $\boldsymbol{B}$ is described by the set of first order differential equations as follows:

$$\frac{d\boldsymbol{x}}{dt} = \boldsymbol{v}, \tag{3.14}$$

$$\frac{d\boldsymbol{p}}{dt} = \boldsymbol{F}_\mathrm{L}. \tag{3.15}$$

Here, $\boldsymbol{x}$ and $\boldsymbol{v}$ denote the particle position vector and velocity vector, respectively, $\boldsymbol{F}_\mathrm{L}$ represents the Lorentz force experienced by the particle (see Eq. (2.3)). Particle-tracking simulations are used to integrate the equations of motion numerically. The numerical integration is performed using integrators of the Runge-Kutta type. Before each Runge-Kutta step, the electric and magnetic fields at the current particle position are computed. The new particle position $\boldsymbol{x}'$ and velocity $\boldsymbol{v}'$ (among other parameters) are than determined in each Runge-Kutta step and are stored to multiple files for data post-processing.

For the initialization of the trajectory computation, a set of particle properties, such as the initial particle position and kinetic energy, need to be defined. These parameters are presented in Appendix B.1. The structure of the output files and routines used for data post-processing are described in Appendix B.2.

Chapter 4

Electrode Designs for Simultaneous Particle Measurement

The NoMoS experiment uses a uniformly curved magnetic field to separate the charged particles emitted in the neutron decay according to their momentum and charge and, thus, facilitates a simultaneous measurement of the particles. As neutron decay experiments are, in general, confronted with low statistics, a simultaneous particle measurement is very attractive: the signal rate cumulated from the same decay rate doubles. Such a measurement requires a well conceived configuration of particle detectors and of the proton post-acceleration electrode to achieve the desired precision in the determination of the neutron decay observables mentioned in Section 2.1. Two simple detector configurations are proposed in Section 4.1. In Section 4.2, two post-acceleration electrodes suited for each detector setup are presented together with geometrical and electrical parameters of the individual detection components. Studies of systematic effects are performed for the proposed setups and variations thereof in Section 4.3 based on the electrode requirements described in Section 3.2. Findings are summarized in Section 4.4.

4.1 Possible Detector Configurations

NoMoS aims to measure the electron and proton drift distance spectra (see Fig. 3.2) on spatially resolving detectors. One important factor in the design of the detection system is the alignment between the two particle detectors and the two particle beams. A well conceived detector configuration is required to achieve the desired precision in the determination of the neutron decay observables a and b.

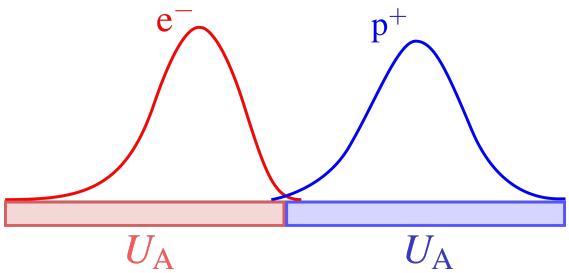


Figure 4.1: Scheme of detector setup A: The electron (red rectangle) and proton (blue rectangle) sensors, which form a common detection surface, are positioned such that both the electron and the proton drift distance spectra are completely mapped onto the detector surface. A surface potential U_A is applied to both detectors.

The most simple detector configuration consists of the electron and proton sensors joined to form a common detection surface, as shown in Fig. 4.1. In such a setup, denoted in the

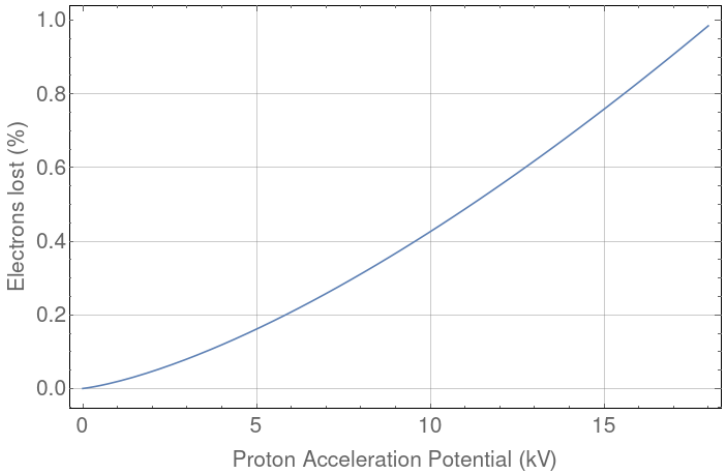


Figure 4.2: Relative electron loss as a function of the proton acceleration potential U_{A} applied at the detector surface. The number of electrons lost due to reflection by the electrostatic potential increases with U_{A}. Figure courtesy of Daniel Moser.

following as setup A, both drift distance spectra can be completely mapped onto the sensors. The detector size is determined by the size of the aperture and that of the two spectra. Since protons require post-acceleration to detectable energies, a negative electrostatic potential U_{A} is applied to the sensor surface. This affects the number of detected electrons, since a fraction of the electron spectrum is reflected by the negative potential. The number of electrons lost by electrostatic potential reflection increases with the post-acceleration potential $|U_{\mathrm{A}}|$, as show in Fig. 4.2. For a post-acceleration potential of 15 kV about 0.8 % of electrons are lost to reflection. Thus, a longer measurement of decay electrons is required to obtain the same statistics as in a measurement in which no electrons are lost ($|U_{\mathrm{A}}| = 0$ kV). Additionally, the effect might become significant in the determination of the Fierz interference term b. First approximations show that this systematic effect is, however, small and more detailed studies will be included in [26]. Since there is no electron loss when the electron detector is operated at zero-potential, an alternative detector configuration is proposed.

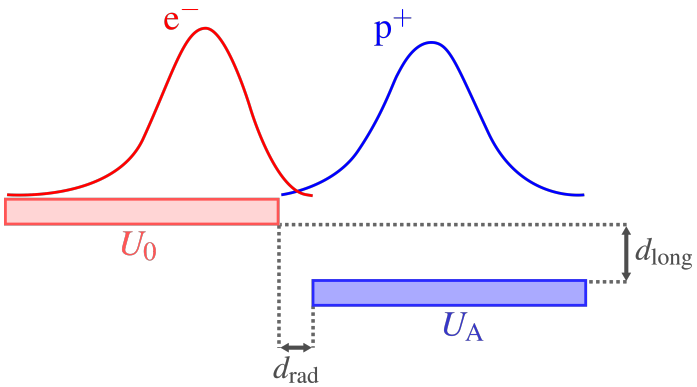


Figure 4.3: Scheme of detector setup B: The electron detector (red rectangle) and the proton detector (blue rectangle) are positioned such that the electron and the proton spectra are mapped onto the corresponding detector. The two particle detectors are separated in longitudinal and radial direction, denoted by d_{long} and d_{rad}, respectively. Note that a complete mapping of both particle spectra onto the detectors is not possible in such a configuration.

The two particle detectors need to be spatially separated to shield the electron beam from the proton post-acceleration potential U_{A}. Such a configuration, denoted as setup B, together with the two drift distance spectra is shown in Fig. 4.3. Here, the electron detector is shifted by

a radial and longitudinal distance d_{rad} and d_{long}, respectively, away from the proton sensor. Since the two spectra overlap at the center, it is not possible to completely map both particle beams onto the sensors. Particles are lost due to detector shadowing. This affects the shape of the measured proton spectrum and, thus, the measurement sensitivity. This effect is studied in more detailed in [26]. First results indicate that in a configuration where the electron detector blocks 0.5 cm of the proton spectrum, the effect in the determination of the correlation coefficient a is about 6×10^{-6} (see Fig. 4.4) and, therefore, negligible. Such a configuration requires a precise alignment of the two sensors relative to both the particle spectra.

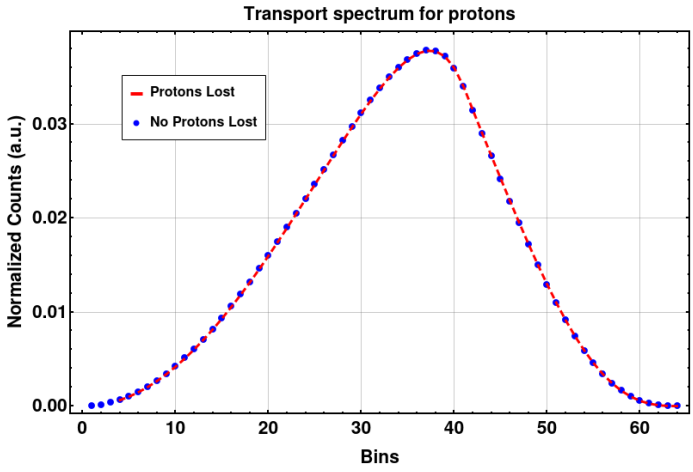


Figure 4.4: Measured proton spectrum with and without proton loss due to shadowing of the proton detector by the electron sensor in setup B: A cut of 0.5 cm of the proton beam, which corresponds to a loss of a fraction of low energetic protons, does not significantly affect the shape of the measured spectrum. The effect in the determination of the correlation coefficient a is estimated to 6×10^{-6} and is, thus, negligible. Figure courtesy of Waleed Khalid.

In the following section, two simple post-acceleration electrodes are proposed for each detector configuration.

4.2 Geometrical and Electrical Setup of the Detection System

The detection system is composed of the electron and proton detectors and the proton post-acceleration electrode and is surrounded by a cylindrical vacuum tube. Two simple cylinder electrodes are proposed for the two possible detector configurations. The geometry of the detection region in both setups is described in the following.

Fig. 4.5a shows a top view of the detection region in the x-y-plane for setup A. The two detectors are located inside the post-acceleration electrode, which is surrounded by the vacuum tube. The geometry of this configuration is axially symmetric. A cross section of the geometry in the y-z-plane is shown in Fig. 4.5b. Both particle sensors are placed on top of the electrode end plate. The cylinder electrode is defined by the diameter D, the length L and has a thickness w. The surface potential U_{A} is applied at the electrode-detector system while the vacuum tube is connected to ground potential. The electrode diameter is limited on the one hand by the size of the two particle detectors and on the other hand by the vacuum tube of diameter D_{vt}. Additionally, in order to avoid strong electric fields between the high voltage electrode and the grounded vacuum tube the two components are separated by a distance d.

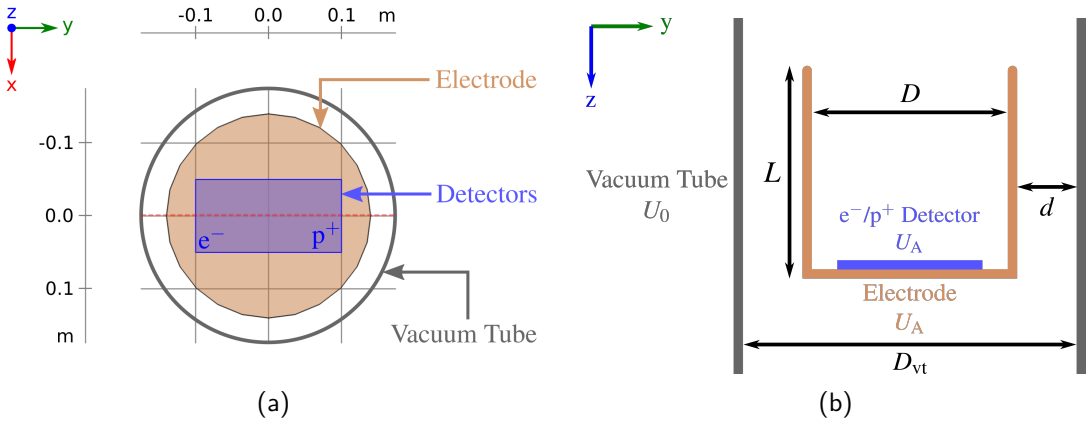


Figure 4.5: (a) A top-view in the x-y-plane of setup A. The geometry is axially symmetric. The cylindrical post-acceleration electrode (orange) is located inside the vacuum tube (gray cylinder). The two particle detectors (blue) are centered inside the electrode. (b) A sketch of the detection system in the y-z-plane at $x = 0$, indicated by the red dashed line in (a). The detector is located at the bottom of the electrode of diameter D and length L. The electrode-detector system is operated at the potential U_{A}. The surrounding vacuum tube has a diameter D_{vt} and is connected to zero-potential.

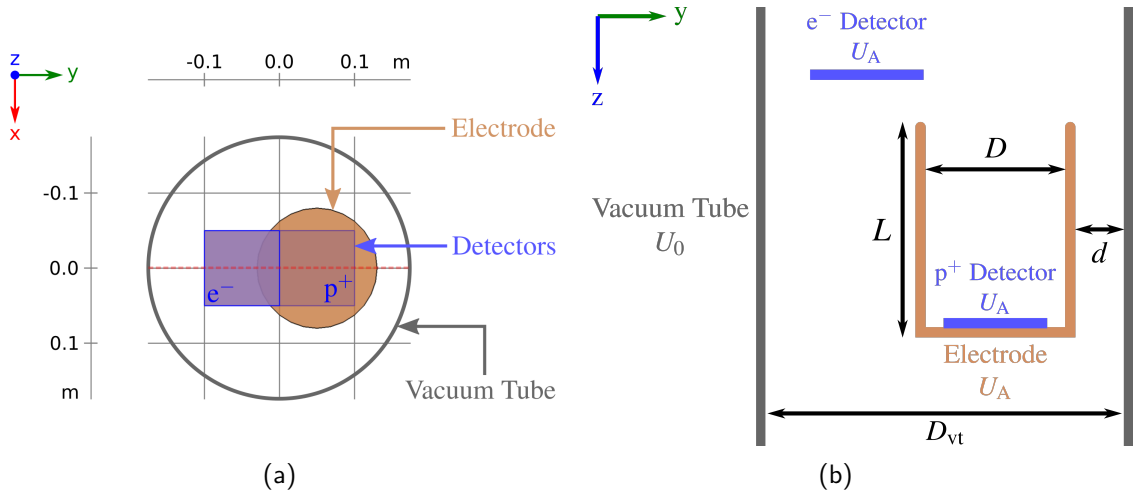


Figure 4.6: (a) A top-view in the x-y-plane of setup B. The proton detector (light blue) is centered inside the cylindrical post-acceleration electrode (orange). The electron detector (blue) is located above the electrode. A cylindrical vacuum tube surrounds the two detectors and the electrode. (b) A sketch of the detection system in the y-z-plane at $x = 0$, indicated by the red dashed line in (a). The proton detector is located at the bottom of the electrode of diameter D and length L. The two particle sensors are spatially separated both in longitudinal and radial direction. A surface potential U_{A} is applied to the electrode and proton detector while the electron sensor is operated at zero-potential. The surrounding vacuum tube has a diameter D_{vt} and is grounded.

A sketch of the detection region including setup B is shown in Fig. 4.6. The geometry of this configuration is no longer axially symmetric: the cylindrical electrode surrounds the proton detector and is located off the central axis z, as can be seen in Fig. 4.6a. The proton and electron detectors are spatially separated, both in radial and longitudinal direction, whit the proton sensor located at the electrode end plate, as shown in Fig. 4.6b. The cylinder electrode has diameter D, length L and thickness w. The surface potential U_{A} is applied to both the electrode and proton detector. The electron detector and the vacuum tube are connected to zero-potential.

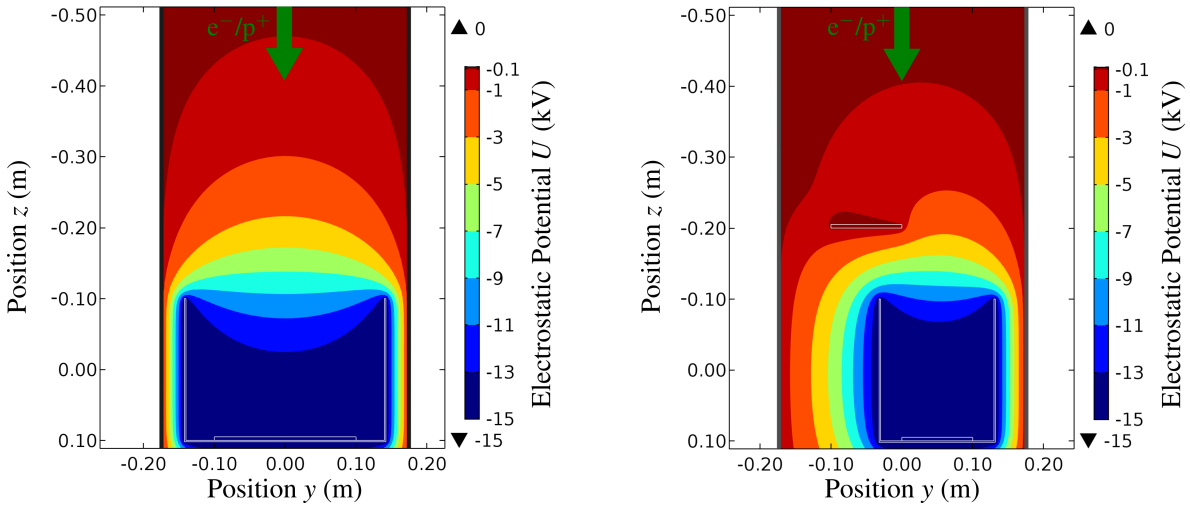


Figure 4.7: Electrostatic potential U generated by the post-acceleration electrode (white) inside the detection region in (a) detector setup A and (b) detector setup B, viewed in y-z-plane for $x = 0$ for. The decay particles enter the detection region from the top as indicated by the green arrow. White regions represent areas outside the detection region. A comparison between (a) and (b) shows that the electrostatic potential generated by the electrodes extends far into the detection region. The electron detector of setup B, which is operated at zero-potential, constraints the potential in its vicinity and contributes to the shielding of the detection region from large electrode potentials.

The vacuum tube diameter is given by D_{vt}. As in setup A, a distance d is considered to avoid strong electric fields between the high voltage electrode and the vacuum tube.

To illustrate the difference in the electrical properties of the two detection setups, the electrostatic potential U generated by the two cylinder electrodes inside the detection region is shown in Fig. 4.7. The geometrical and electrical parameters of setups A and B are listed in Table 4.1. In both setups, the electron and proton sensors have an area of $10 \times 10\,\mathrm{cm}^2$ and a thickness of 5 mm. The vacuum tube has a diameter D_{vt} and length L_{vt} of 35 cm and 300 cm, respectively. Decay particles enter the detection region from the top and their spatial distribution corresponds to the drift distance spectra shown in Fig. 3.2.

Table 4.1: Geometrical and electrical parameters of detection setup A and B shown in Figs. 4.5b and 4.6b, respectively.

Parameter		Setup	
		A	B
Electrode Diameter D (cm)		28	16
Electrode Length L (cm)		20	20
Post-acceleration Voltage U_{A} (kV)		-15	-15
Detector Separation	d_{long} (cm)	-	30
	d_{rad} (cm)	-	0

Multiple features of the electrostatic potential, which are discussed in more detail in the following section, are mentioned below:

- Protons experience a decreasing electrostatic potential and are accelerated as they move towards the sensor.

- Equipotential lines are curved, indicating inhomogeneities of the electrostatic potential. This effect is more pronounced in regions close to the electron detector of setup B where the electrode potential is constrained by the zero-potential applied to the sensor.
- The electrostatic potential extends far into the detection region.

Note that decay electrons are decelerated by the electrostatic potential before reaching the detector, independent on the chosen setup. Although low energetic electrons are reflected by the negative potential, the fraction of electrons lost is smaller in setup B. This is due to the lower electrostatic potential generated by the electrode in the vicinity of the electron sensor.

4.3 Electrode Requirements Studies

The post-acceleration electrode should be designed to fulfill the requirements discussed in Section 3.2. The focus of this section lies on investigations of multiple electrode requirements, considering detection setups A and B and adjustments thereof. Results presented in the following were obtained from simulations performed using COMSOL Multiphysics.

4.3.1 Proton Post-acceleration

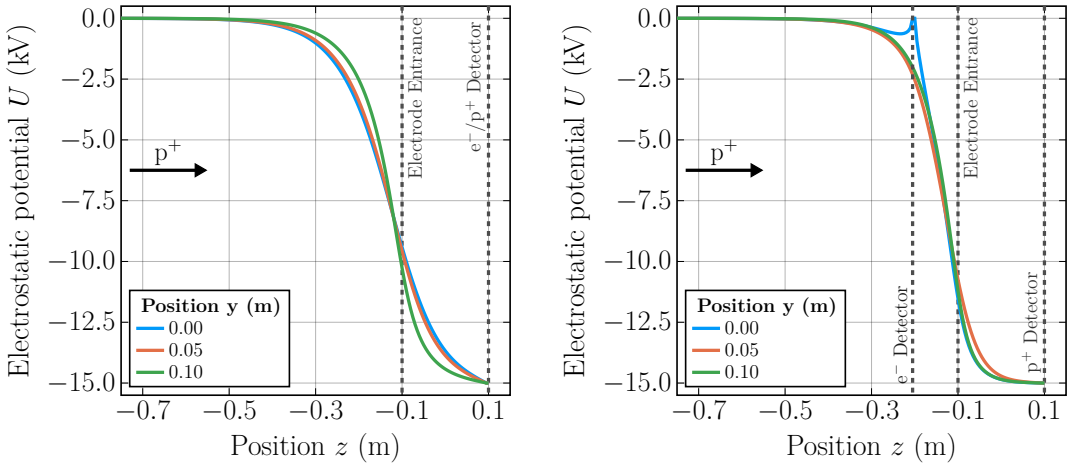


Figure 4.8: Electrostatic potential U generated by the cylinder electrode of (a) setup A and (b) setup B inside the detection region, evaluated as a function of the position z for multiple positions y at $x = 0\,\text{m}$. The direction from which the decay protons enter the detection region is indicated by the black arrow. Additionally, gray, dashed lines mark the location of the electrode entrance and of the two particle detectors. Decay protons experience a negative electrostatic potential as they move towards the detector. Note that the potential shows a gradient in direction y. Additionally, the electron detector of setup B prevents the potential to decrease monotonically for $y = 0\,\text{m}$.

The electrode should provide the electrostatic potential required for the proton post-acceleration. According to Fig. 4.7, protons experience a decreasing electrostatic potential as they move towards the proton detector inside the detection region. The electrostatic potential as a function of position z is shown in Fig. 4.8 for both detector setups for multiple positions y at $x = 0$. The various positions y are chosen to illustrate the electrostatic potential experienced by protons moving in different areas of the detection region. In both setups, particles enter the detection

region and experience a slowly decreasing potential in the regions far from the electrode. As they move closer to the electrode entrance they are accelerated by the rapidly decreasing potential. Protons experience a large fraction of the post-acceleration over this region. Inside the electrode, the slope of the potential changes again: the particles experience a slower decreasing potential as they move towards the detector. Note that the electrostatic potential does not decrease monotonically in setup B for $y = 0\,\mathrm{m}$. It reaches a maximum at the electron detector. This intrinsic feature of setup B is discussed in Section 4.3.4.

Both electrodes provide the required post-acceleration potential for the decay protons. However, protons are accelerated at different rates, depending on the region they cover when moving towards the detector. This indicates that the electrostatic potential, evaluated across slices in the x-y-plane of the detection region, is not homogeneous. This aspect is studied in more detail in the following.

4.3.2 Homogeneity of the Electrostatic Potential

As described in Section 3.2.2, radial variations of the electrostatic potential in regions covered by the decay particles should be sufficiently small to ensure an adiabatic particle transport. Additionally, homogeneity of the electrostatic potential is required for a position-independent reflection of backscattered protons, which leave the sensor with kinetic energy T_b and pitch angle θ_b. The following investigations evaluate relative deviations ΔU_rel of the electrostatic potential across multiple reference planes x-y, as described in Eq. (3.6). Here, $U_\mathrm{ref}(z)$ is the potential evaluated at the center of the rectangular proton beam, described by the coordinates $x = 0\,\mathrm{m}$ and $y = 0.045\,\mathrm{m}$, at a given position z.

The relative change of the electrostatic potential ΔU_rel, viewed in the y-x-plane, is shown in Fig. 4.9 at multiple positions z for detector configurations A and B. The positions z are chosen to show the potential homogeneity at various distances d_s above the proton sensor.

The homogeneity of the electrostatic potential at small distances from the proton sensor is first considered. Figs. 4.9a and 4.9b show the relative deviation ΔU_rel of the potential across the electrode, evaluated at a distance d_s of 1 cm ($z = -0.085\,\mathrm{m}$) above the detector. Results show that the largest potential deviations occur at the edges of the proton beam in both setups. However, relative changes of the electrostatic potential are small, especially in setup B. The maximum potential deviation $|\Delta U_\mathrm{rel}^\mathrm{max}|$ is $0.36\,\%$ and $0.06\,\%$ in setup A and B, respectively. Further evaluations of $|\Delta U_\mathrm{rel}^\mathrm{max}|$ at a distance of 5 cm from the detector ($z = -0.045\,\mathrm{m}$) yield $0.4\,\%$ in setup B, compared to $2.16\,\%$ in setup A.

Relative deviations of the electrostatic potential ΔU_rel at a distance d_s of 20 cm above the sensor, corresponding to the location of the electrode entrance ($z = 0.1\,\mathrm{m}$), are shown for both setups in Figs. 4.9c and 4.9d across the y-x-plane. Here, radial potential variations are smaller in setup A, with a maximum potential deviation $|\Delta U_\mathrm{rel}^\mathrm{max}|$ of about $12\,\%$. In comparison, $|\Delta U_\mathrm{rel}^\mathrm{max}|$ is evaluated at about $19\,\%$ in setup B.

The electron detector of setup B, which is operated at zero-potential, constrains the electrostatic potential in its vicinity and induces a significant potential inhomogeneity across the proton beam. Figs. 4.9e and 4.9f show the relative potential deviation ΔU_rel at a distance of 1 cm above the electron detector ($z = 0.215\,\mathrm{m}$) of setup B, evaluated in both detector setups. Here, the maximum potential deviation $|\Delta U_\mathrm{rel}^\mathrm{max}|$ is $36\,\%$ and $60\,\%$ in setup A and B, respectively.

Both detection setups require geometrical adjustments to improve the homogeneity of the electrostatic potential across the proton beam, especially at large distances from the proton detector. The effects of such adjustments on radial potential variations are studied in the following for each detector configuration individually. The planes of reference considered in evaluations of radial potential variations remain the same, independent of the electrode adjustment considered.

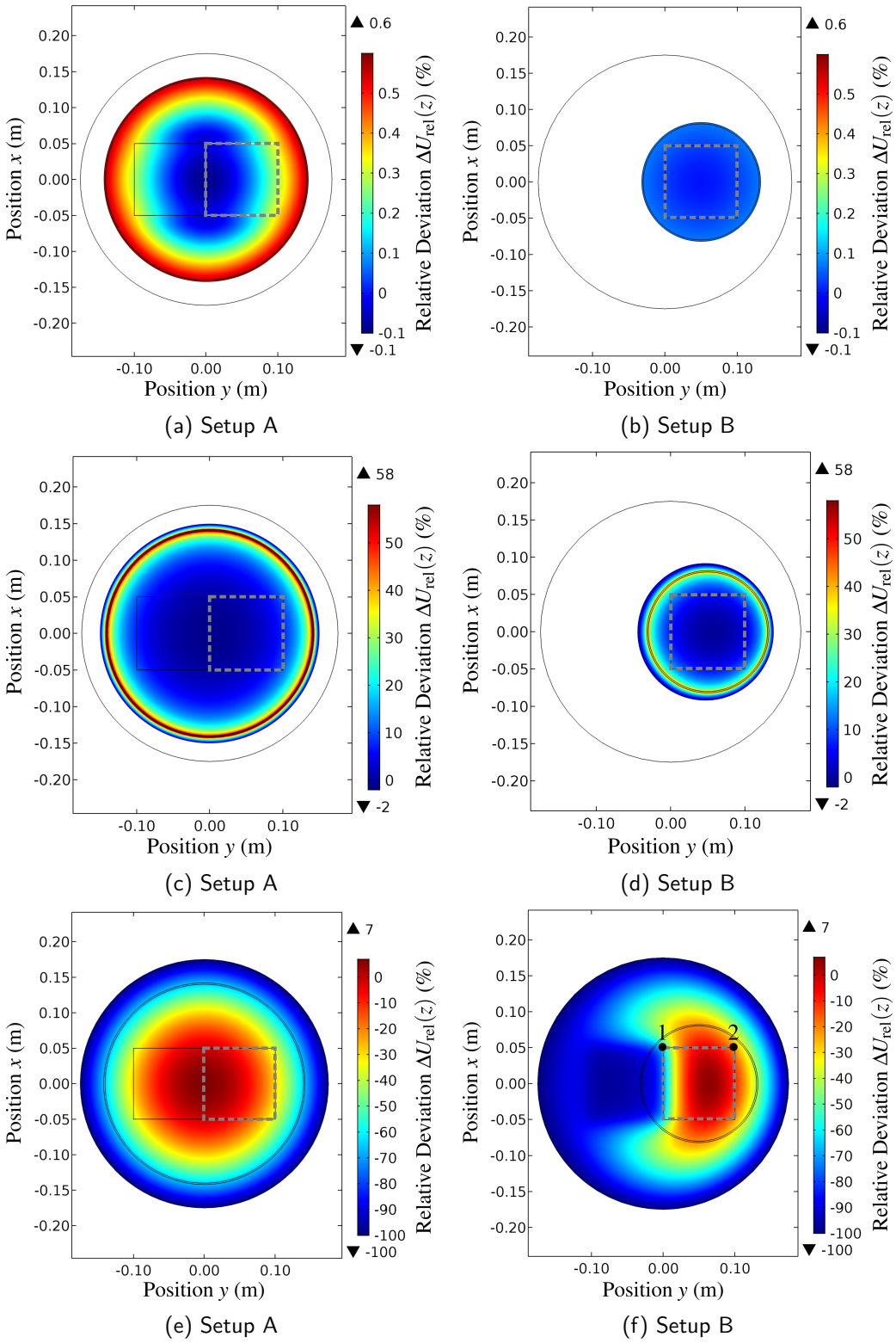
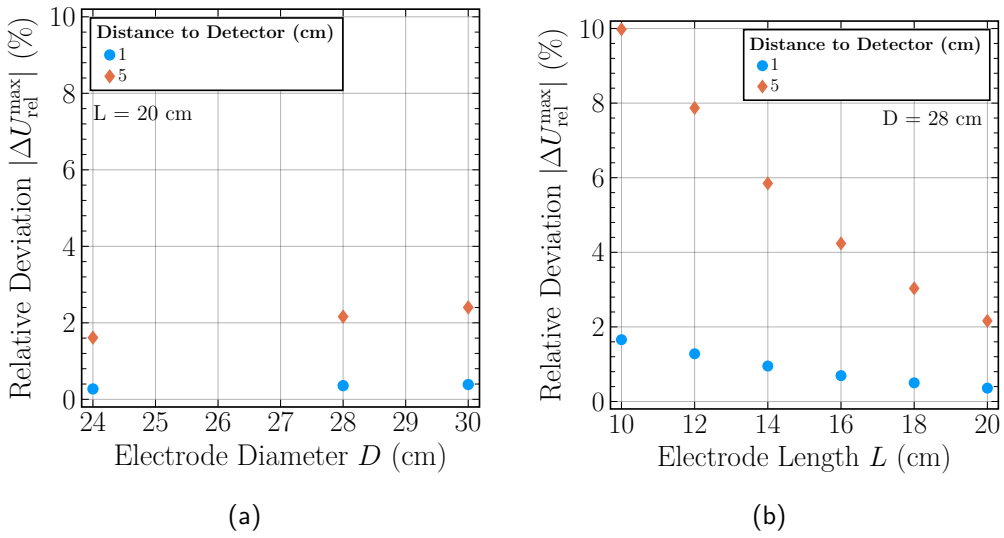


Figure 4.9: Relative potential deviation ΔU_{rel} evaluated in the y-x-plane at $x = 0\,\mathrm{m}$ for detection setups A and B at (a)−(b) a distance of 1 cm above the proton detector ($z = -0.085\,\mathrm{m}$), (c)−(d) at the electrode entrance ($z = 0.1\,\mathrm{m}$) and (e)−(f) at a distance of 1 cm above the electron detector of setup B ($z = 0.215\,\mathrm{m}$). The proton detector is marked by the dashed, gray rectangle. Additionally, two corners of the proton beam are marked in (d) by the black circles denoted as 1 and 2. The potential U_{ref} denotes the potential at the center of the proton beam (position $y = 0.045\,\mathrm{m}$). Input data U_{ref}: (a) $-14.916\,\mathrm{kV}$, (b) $-14.989\,\mathrm{kV}$, (c) $-9.534\,\mathrm{kV}$, (d) $-10.760\,\mathrm{kV}$, (e) $-2.86\,\mathrm{kV}$ and (f) $-1.87\,\mathrm{kV}$.

Adjustments to Setup A

Large potential deviations arise across the proton beam in setup A due to two factors: the position of the proton sensor (and, thus, proton beam) relative to the electrode and the larger electrode diameter, required to fit both particle detectors. Potential inhomogeneities can be reduced if a smaller electrode diameter is chosen as can be seen in Fig. 4.10a. A reduction of the electrode diameter D from 28 cm to 24 cm results in a decrease of the maximum relative potential deviation $|\Delta U_{\mathrm{rel}}^{\mathrm{max}}|$ by about 24 % and 25 % to 0.3 % and 1.6 % at a distance of 1 cm and 5 cm above the detector, respectively. A further reduction of the electrode diameter requires an adjustment of the detector size and, hence, of the particle beam size.



(a) (b)

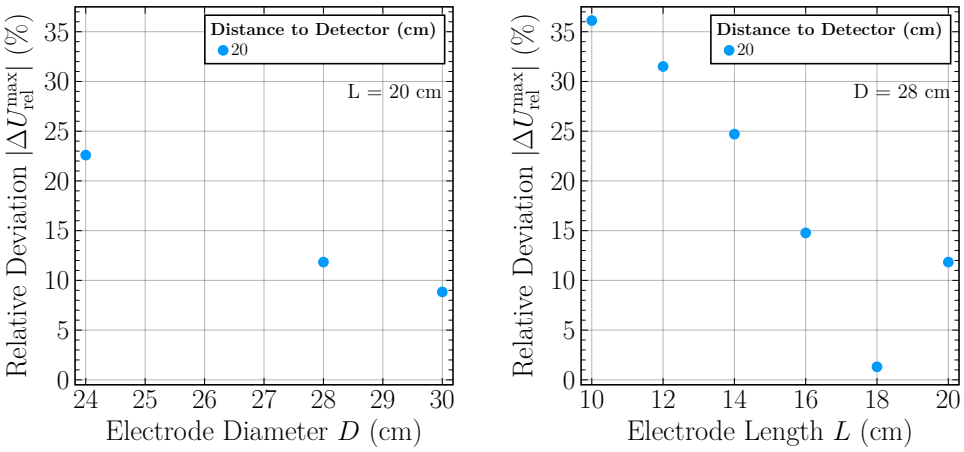
Figure 4.10: Maximum relative potential deviation $|\Delta U_{\mathrm{rel}}^{\mathrm{max}}|$ evaluated at a distance of 1 cm and 5 cm from the proton detector for multiple (a) diameters D and (b) lengths L of the electrode in setup A. A small electrode diameter is required to obtain a homogeneous potential in the vicinity of the proton detector. To minimize deviations $|\Delta U_{\mathrm{rel}}^{\mathrm{max}}|$, an electrode with a length larger than 20 cm is required.

Alternatively, a longer electrode can be chosen to improve the potential homogeneity in the vicinity of the proton detector in setup A. In the following studies, the position of the electrode end plate is fixed while the electrode length is varied. The maximum potential deviation $|\Delta U_{\mathrm{rel}}^{\mathrm{max}}|$ evaluated at small distances from the proton detector is shown in Fig. 4.10b for multiple electrode lengths L. It can be seen that a short electrode generates a strongly inhomogeneous potential in this regions. To achieve similar results as in setup B, an electrode with a length above 20 cm is required.

Effects of an adjustment of the electrode diameter D and length L on relative potential variations at a distance of 20 cm above the proton sensor (at $z = 0.1$ m) are shown in Fig. 4.11. In Fig. 4.11a it can be seen that potential inhomogeneities decrease in this region with increasing electrode diameter D. The maximum relative potential deviation $|\Delta U_{\mathrm{rel}}^{\mathrm{max}}|$ is reduced by about 25 % to 9 % if the electrode diameter is increased from 28 cm to 30 cm.

The reference plane x-y at position $z = 0.1$ m was chosen to evaluate the relative change of the electrostatic potential at the entrance of the cylinder electrode of length $L = 20$ cm. Thus, an adjustment of the electrode length changes the distance between this reference plane and the plane in which the electrode entrance is located[1]. Studies performed for an electrode of length $L = 20$ cm have shown that radial variations of the electrostatic potential become significant

[1]As already mentioned, one fixed parameter of the cylinder electrode in the studies performed for length varitations is the location of the electrode end plate.



(a) (b)

Figure 4.11: Maximum relative potential deviation $|\Delta U_{\mathrm{rel}}^{\mathrm{max}}|$ evaluated at a distance of 20 cm from the proton detector for multiple (a) diameters D and (b) lengths L of the cylinder electrode in setup A. A large electrode diameter is required to obtain a homogeneous potential in this region. Potential inhomogeneities increase for shorter electrodes.

outside the electrode region (see Fig. 4.9e). For electrodes of lengths $L < 20$ cm, the reference plane at $z = 0.1$ m lies above the electrode entrance. Fig. 4.11b shows that the maximum relative potential deviation $|\Delta U_{\mathrm{rel}}^{\mathrm{max}}|$ present in the reference plane (at an axial distance of 20 cm above the proton sensor) decreases significantly with increasing electrode length L. Note that the best result is achieved in this region when the electrode has a length of 18 cm.

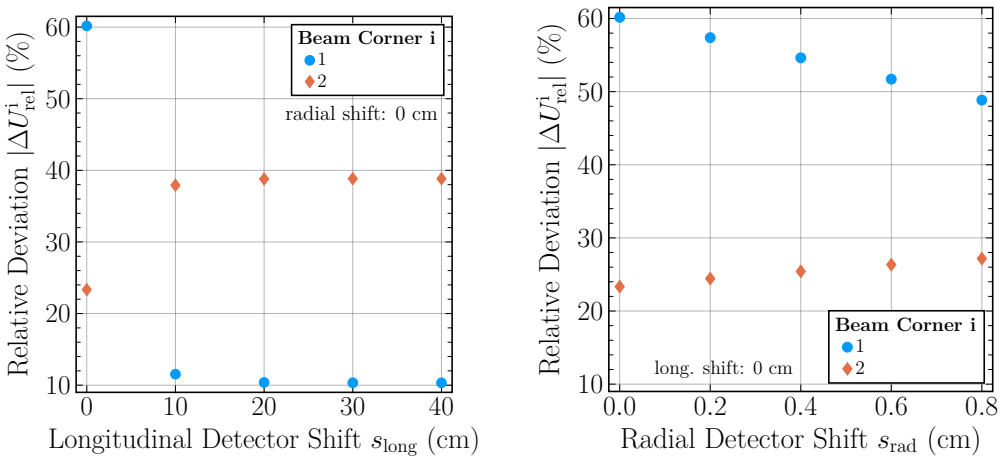
Results show that additional electrode parameters require adjustments to furher minimize radial potential variations across the proton beam.

Adjustments to Setup B

The electron detector can be longitudinally shifted away from the electrode to minimize relative deviations of the electrostatic potential at larger distances from the proton sensor. Fig. 4.12a shows the maximum relative potential deviation $|\Delta U_{\mathrm{rel}}^{\mathrm{i}}|$ for multiple longitudinal shifts s_{long} of the electron detector, evaluated at the two beam corners marked in Fig. 4.9f as 1 and 2, at a distance of 1 cm above the electron sensor. A shift s_{long} of 10 cm reduces $|\Delta U_{\mathrm{rel}}^{\mathrm{i}}|$ at beam corner 1 by about 81 % to 12 %. However, $|\Delta U_{\mathrm{rel}}^{\mathrm{i}}|$ increases at beam corner 2 by 63 % to 39 % if such a configuration is considered. Results show that longitudinal shifts above 10 cm do not significantly affect the homogeneity of the electrostatic potential in this plane.

Alternatively, a radial shift s_{rad} of the electron detector in the direction $-y$ can be considered. However, results show that such an adjustment has a lower impact on the homogeneity of the electrostatic potential and relative deviations $|\Delta U_{\mathrm{rel}}^{\mathrm{i}}|$ remain significant, as can be seen in Fig. 4.12b. A radial shift of the proton detector by 0.8 cm results in a decrease of $|\Delta U_{\mathrm{rel}}^{\mathrm{i}}|$ by 81 % to 18 % at beam corner 1 and in an increase by 17 % to 27 % at beam corner 2. Note that the fraction of electrons mapped onto the sensor surface decreases with increasing radial shift of the sensor. At the same time, a larger fraction of the proton spectrum can be mapped onto the proton detector, since the shadowing effect by the electron sensor decreases.

Results have shown that radial potential variations across the proton beam are significantly smaller ($|\Delta U_{\mathrm{rel}}^{\mathrm{max}}| < 1\,\%$) in setup B at small distances from the proton sensor, compared to setup A. Both detection setups require further modifications to minimize inhomogeneities of the electrostatic potential at larger distances from the detector. Particle-tracking simulations need to be performed to quantify the effect of radial potential variations on decay protons and to set a



(a) (b)

Figure 4.12: Relative potential deviation $|\Delta U_{\mathrm{rel}}^{\mathrm{i}}|$ evaluated at a distance of 1 cm above the electron detector of setup B for multiple (a) longitudinal shifts s_{long} and (b) radial shifts s_{rad} of the electron sensor. Here, the index i denotes the beam corners 1 and 2, marked in Fig. 4.9f. Potential inhomogeneities decrease significantly at corner 1 if the electron detector is shifted longitudinally away from the electrode while the opposite holds for corner 2. A radial shift of the electron detector is not as effective in the reduction of $|\Delta U_{\mathrm{rel}}^{\mathrm{i}}|$.

limit on the tolerated relative potential deviation U_{rel}[2]. Such simulations were not performed for studies presented in the current chapter. They are, however, included in studies of the adiabatic particle transport performed in Chapter 5 in the context of the single proton measurement.

Although the grounded electron detector in setup B causes significant inhomogeneities in the electrostatic potential generated by the electrode, the sensor might shield the regions far from the electrode and, thus, the R×B drift region from large electrostatic potentials. The following section presents electrostatic potential studies at large distances from the electrode in both proposed setups.

4.3.3 Electrostatic Potential at large Distances from the Electrode

One criteria of the electrode design is the suppression of electrostatic potentials inside the R×B drift region. The potential induced by the electrode at the interface between the drift and the detection region should not exceed −10 mV (see Section 3.2). This condition is used to the determine the required length of the detection region which should be (preferably) short. The distance from the electrode entrance where this potential value is reached is determined in both proposed setups in the following. Additionally, a lower estimate for the required length of the detection region is provided. The minimum detection region length is determined by the sum of the electrode length L and the distance d_{f}.

Results show that the electrostatic potential reaches −10 mV at a distance d_{f} of 104 cm and 97 cm from the electrode entrance in setup A and B, respectively[3]. The smaller distance d_{f} obtained in setup B originates, among other parameters, in two factors: the smaller electrode diameter and the additionally shielding of the detection region from large electrostatic potentials by the grounded electron detector. Since the electrodes have a length of 20 cm, both setups require a detection region longer than 120 cm to fulfill this electrode requirement.

[2]Simulations for backscattered protons are also required. These are, however, beyond the scope of this thesis.

[3]The values obtained in the evaluation of the distance d_{f} and, thus, of the electrostatic potential are limited by the resolution of the mesh chosen in the simulation.

Adjustments to Setup A

Adjustments of the electrode diameter and length are not effective in the reduction of the distance d_f and, thus, of the detection region length. A decrease of the electrode diameter D in setup A from 28 cm to 24 cm reduces d_f by only 1 % to 103 cm while a decrease of the electrode length L leaves d_f unaffected. Since the lower estimate of the detection region length is determined by the electrode length and the distance d_f, a shorter electrode can be considered in both setups. However, such an adjustment comes at the cost of larger inhomogeneities of the electrostatic potential inside the electrode, as shown in Fig. 4.10b.

Adjustments to Setup B

A longitudinal shift of the electron detector to larger distances from the electrode of setup B increases the shielding effect in the regions far from the electrode. For this study, longitudinal detector shifts in the range between 0 cm and 40 cm have been considered. Results show that the effect is, however, not significant in the reduction of the distance d_f, as improvements are below 1 %, independent on the amount of detector shift.

Radial shifts of the electron detector result in a decrease of the shielding effect in regions far from the electrode. Studies performed for radial detector shifts in the range between 0 mm and 8 mm show that, although the distance d_f increases with the radial detector shift, effects remain well below 1 %.

So far, results have shown that a position adjustment of the grounded electron detector in setup B is not effective in the reduction of the detection region length. The detector position does, however, affect the homogeneity of the electrostatic potential at larger distances from the proton sensor. Further electrode requirements have to be analyzed to determine the optimal location of the electron detector. According to Fig. 4.8b, an additional effect occurs in the vicinity of the electron detector at position $y = 0$ m: the electrostatic potential has a minimum in this region, indicating the presence of a Penning trap. This intrinsic feature of setup B is discussed in more detail in the following section.

4.3.4 Particle Traps

The detection region should be free of any particle traps to avoid particle loss and additional background effects in the particle measurement. Two types of particle traps, relevant in the design of the detection region, have been discussed in Section 3.2.4: Penning trap and electromagnetic trap. These are studied in the following.

Penning Traps

There are no Penning traps inside the detection region in setup A. In setup B, however, a Penning trap for positively charged particles forms at the electron detector, which is operated at zero-potential (see Figs. 4.7b and 4.8). The trap is located above the electron detector and extends over its edges into the regions covered by low energetic protons. The Penning trap has the largest depth at the inner edge of the electron sensor, corresponding to position $y = 0$ m. Fig. 4.13 shows the electrostatic potential U as a function of position z for $y = x = 0$ m and the Penning trap of depth ΔU of 638 V. The elimination of this trap is crucial for the feasibility of the particle measurement. In the following, geometrical adjustments of setup B, which lead to the suppression of the Penning trap, are proposed.

The trap can be eliminated by placing the electron detector in regions of lower electrostatic potentials. This implies an increase of the longitudinal distance between the electron sensor and

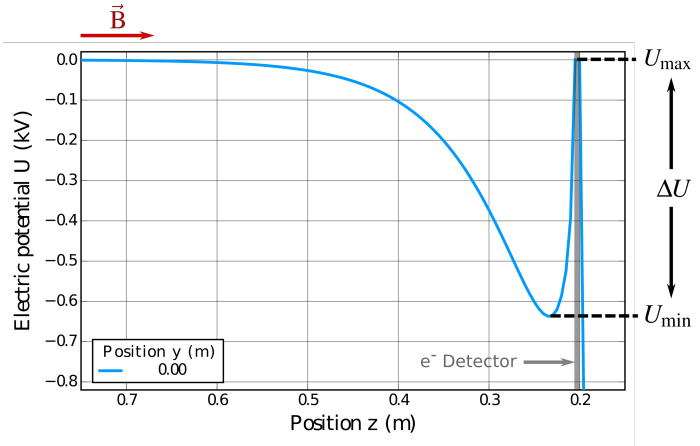


Figure 4.13: Penning trap present in detector configuration B for $x = y = 0\,\text{m}$. A magnetic field line is represented by the red arrow. Particles enter the detection region from the left. The potential has a minimum along the magnetic field line. The depth of the Penning trap ΔU is determined by the difference between the minimum and the maximum potential $U_{\min}$ and $U_{\max}$, respectively. Here, the Penning trap has a depth of $\Delta U = 638\,\text{V}$.

the electrode entrance. Fig. 4.14a shows the trap depth ΔU as a function of the longitudinal detector shift s_{long}. It can be seen that the Penning trap is eliminated if shifts larger than 40 cm are considered.

The Penning trap can be moved away from the proton beam by shifting the electron detector in direction $-y$. Fig. 4.14b shows that a radial shift s_{rad} of 0.8 cm is required to eliminate the trap from the proton beam. An adjustment of the radial detector position, however, does not eliminate the trap present at the electron detector. As already mentioned in the previous sections, a radial shift of the electron sensor also affects the number of detected electrons and protons as the fraction of the two beams which can be mapped onto the detector surface changes.

The two types of detector shifts can be combined to reduce the depth of the Penning trap (for $y = 0$) and the fraction of lost particles. The trap depth ΔU is shown in Fig. 4.14c as a function of the radial detector shift s_{rad} for a longitudinal shift s_{long} of 10 cm and 20 cm. The optimal combination of the two detector shifts and, thus, the maximal allowed depth of the Penning trap depend on the quality of the vacuum inside the detection region (see Section 3.2.4). Additionally, the influence of a detector shift on the potential homogeneity, as shown in Fig. 4.12, should be considered.

Electromagnetic Traps

According to Figs. 4.2 and 4.7, a fraction of decay electrons might be reflected by the negative electrostatic potential in both proposed electrode setups before they reach the electron sensor. Such electrons re-enter the R×B drift region and gyrate back towards the magnetic filter. Results have additionally shown that potential inhomogeneities are significant at large distances from the electrodes of both detection setups (see Section 4.3.2). These might introduce non-adiabatic effects which change particle properties, such as kinetic energy and pitch angle. Reflected electrons might be trapped between the detection region and the magnetic filter, as described in Section 4.3.4. Detailed investigations of the electromagnetic trap based on particle-tracking simulations are required to understand and eliminate this trap. Such simulations are, however, beyond the scope of this thesis.

Electric potential studies have shown that both detection setups provide the electrostatic potential required for the proton post-acceleration. However, significant potential inhomogeneities are present across the proton beam at larger distances from the proton sensor. Additionally,

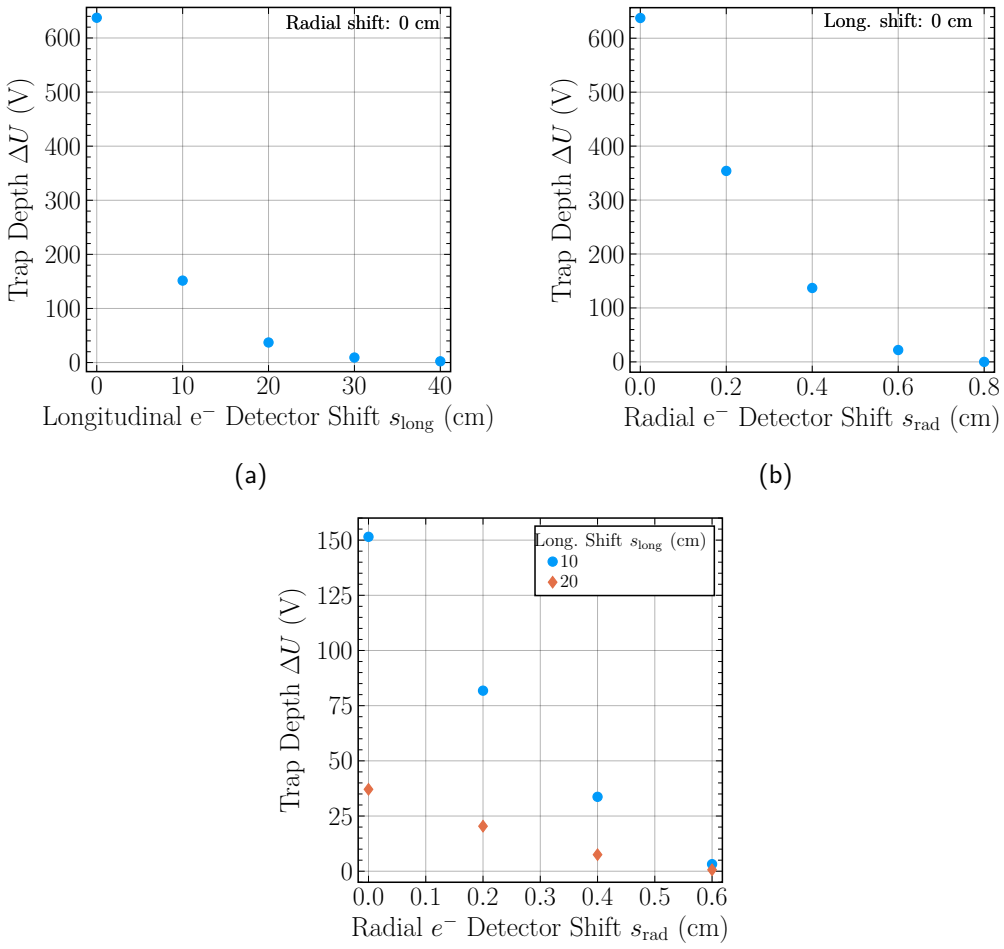


Figure 4.14: Penning trap depth ΔU as a function of the longitudinal detector shift s_{long} and radial detector shift s_{rad}, evaluated at position $y = 0\,\mathrm{m}$ in setup B. (a) The electron detector is located in regions of lower electrostatic potentials if it is shifted by larger distances away from the electrode. Consequently, the trap depth ΔU decreases. (b) The Penning trap is moved away from the proton beam if a radial shift of the electron detector is considered. The trap depth at the edge of the proton beam vanishes when a radial detector shift of 0.8 cm is considered. (c) Penning trap depth ΔU as a function of the radial detector shift s_{rad} for longitudinal detector shifts of 10 cm and 20 cm.

Penning traps are present in the path of both electrons and protons in the vicinity of the grounded electron detector of setup B. Geometrical adjustments of the two setups can be performed to minimize these systematic effects. However, further adjustments of the electrode and of the sensor setup are required to fulfill the electrode design criteria studied so far. The following studies focus on the electric fields generated by the two electrodes inside the detection region and provide an approximation for the distance by which protons drift due to E×B drift effects.

4.3.5 E×B Drift Effect

Decay protons are guided by a uniform magnetic field from the R×B drift region towards the detector and are accelerated by the electric field generated by the high voltage electrode. The spatial distribution of the proton (and electron) drift distance spectrum should not be significantly affected by systematic effects induced by the high voltage electrode. One such systematic effect is the E×B drift effect. In this section, an approximation of the drift distance $D_{\mathrm{E\times B}}$ by which the protons drift inside the detection region is given using Eq. (3.7).

As charged particles might experience E×B drifts in regions where the electric and magnetic fields are not aligned (see Eq. (2.11)), the orientation and magnitude of the electric field generated by the two proposed electrodes are first discussed. Figs. 4.15a and 4.15b show the orientation of the electric field E in the y-z-plane of the detection region for $x = 0$ in setups A and B, respectively. The proton beam is marked by the gray area in both figures and the magnetic field is assumed to be uniform and pointing in direction z.

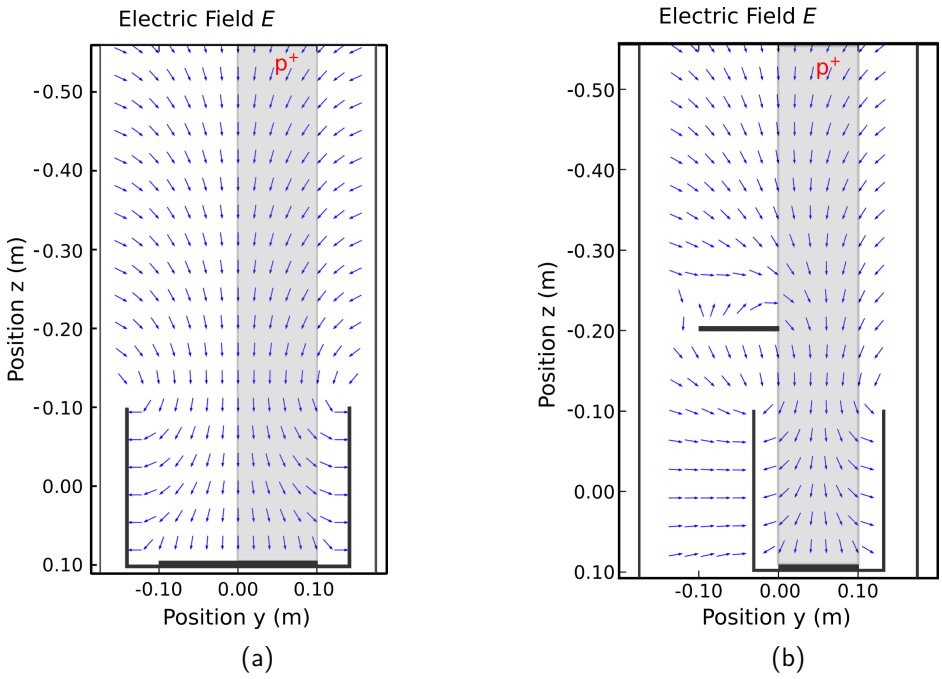


Figure 4.15: Electric field $\boldsymbol{E}$ generated by the electrode inside the detection region, viewed across the y-z-plane for $x = 0\,\mathrm{m}$ for detection setups (a) A and (b) B. The proton beam and the orientation of the magnetic field B are marked by the gray area and by the green arrow, respectively. Note that the length of the electric field arrows does not depict the field strength. The electric field is non-uniform in both detection setups. Due to the axial symmetry of setup A, a region of uniform field forms at the symmetry axis. The grounded electron detector of setup B induces a region of strongly inhomogeneous electric field in its proximity.

The strength of the electric field components E_{i} is shown in Figs. 4.16a and 4.16b as a function

of position z at the center of the proton detector ($y = 0.05\,\mathrm{m}$) for $x = 0\,\mathrm{m}$. Protons move towards the detector in increasing direction z. Since the position x is fixed and the geometry is axial symmetric, the normal component E_x is zero everywhere. Results show that the electric field generated by the two electrodes inside the detection region is non-uniform. A comparison of the two detection setups shows that:

- Setup A: The electric field along the axis of symmetry (at $y = 0\,\mathrm{m}$) has no normal components, since the geometry is axially symmetric (see Fig. 4.15a). Normal field components increase with the radial distance y from the symmetry axis.
- Setup B: The electron detector introduces an additional boundary condition to the electric field and induces a strongly inhomogeneous field region in its vicinity (see Fig. 4.15b). Normal field components increase with the radial distance y from the proton detector center, corresponding to $y = 0.05\,\mathrm{m}$.
- The normal electric field component E_y changes its orientation in the proximity of the electrode entrance in both setups. The absolute value of E_y is, however, smaller in setup B and decreases rapidly towards zero inside the electrode.
- The dominant field component in both setups is E_z. It reaches a minimum close to the electrode entrance. Due to the smaller electrode diameter in setup B, the absolute value of E_z is larger.

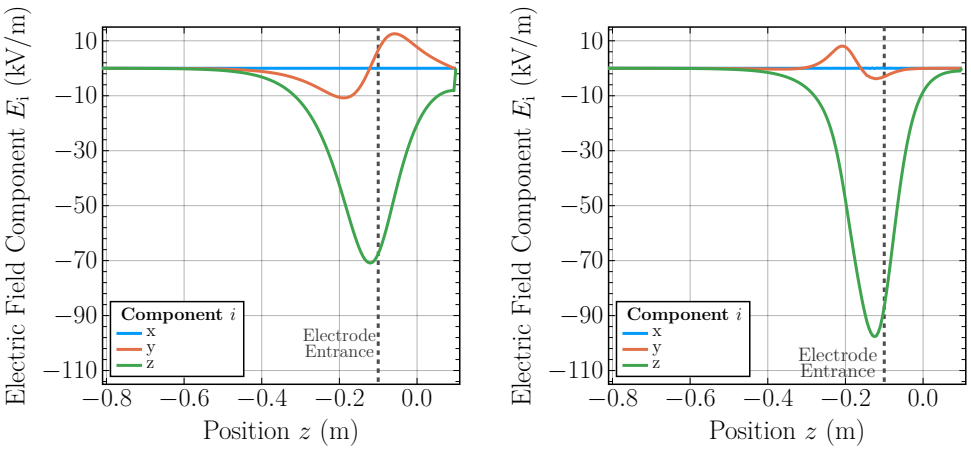


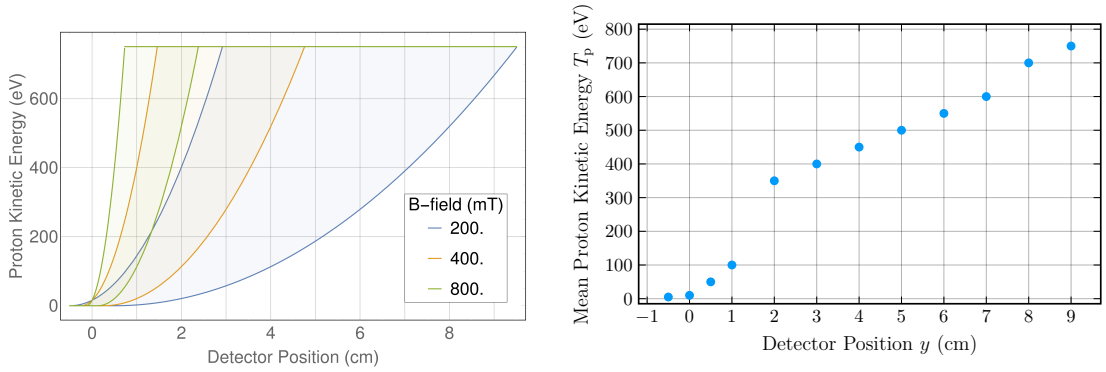
Figure 4.16: Electric field components E_i as a function of position z evaluated at the center of the proton detector ($y = 0.05\,\mathrm{m}$) for detector setups (a) A and (b) B. Note that the field component E_x vanishes in both detector setups since the data is shown for the fixed position $x = 0\,\mathrm{m}$ and the geometry is axial symmetric. Protons move towards the proton sensor in the direction of increasing position z. The electrode entrance is marked by the gray, dashed line. The normal field components E_x and E_y contribute to the E×B drift of the decay particles.

According to Eq. (2.11), charged particles might experience E×B drifts in regions where the electric and the magnetic fields are not aligned. In the two proposed setups, such regions are present both outside and inside the electrode. The amount of E×B drift experienced by a particle is determined on the one hand by particle parameters, such as kinetic energy and pitch angle, and on the other hand by the electric and magnetic fields. Particle tracking is required to correctly estimate the amount of drift experienced by a proton when moving inside the detection region.

Since the two proposed detector setups require further optimization to properly fulfill the electrode requirements discussed so far, no particle-tracking simulations were performed for this chapter. Despite this limitation, areas of the detection region which contribute to the drift effects can be identified. Additionally, the E×B drift distance $D_{\mathrm{E\times B}}$ by which the decay protons drift inside the detection region can be approximated using Eq. (3.7). Before doing so, the correlation between the proton initial kinetic energy T_0 and the detector position y considered in the evaluation of the E×B drift effect is described.

Proton Drift Distance Spectrum

The relation between the initial proton kinetic energy and the detector position, at which the proton is expected to arrive, is required to correctly estimate the E×B drifts experienced by decay protons. The charged decay particles drift inside the R×B region according to their charge and momentum (see Eq. (3.4)). The width of the resulting drift distance spectra depends on the magnetic field strength and on the gyration radius of the decay particles. Fig. 4.17a shows the correlation between the proton kinetic energy T_0 and detector position y for multiple magnetic fields B. Note that this is not a one-to-one mapping of the proton energy to detector position. Protons with the same initial kinetic energy T_0 but with different pitch angles θ_0 follow helical paths of different gyration radii around magnetic field lines towards the detector. This results in a variation of possible detector positions for the given proton energy T_0. For investigations of the E×B drift effect, the mean proton kinetic energy T_{p} at a given detector position, which is most representative of that energy, is considered as shown in Fig. 4.17b for $B = 220\,\mathrm{mT}$. It can be seen that the mean kinetic energy T_{p} increases rapidly in the range $y \in [-1, 2]$. This effect arises as the distance by which the particles drift in the R×B drift region is linear in the particle momentum p (see Eq. (3.4)) and, therefore, proportional to the square root of the particle kinetic energy T. Table 4.2 shows the approximate detector position y (rounded to integer) for multiple magnetic fields B for a mean proton kinetic energy of 10 eV, 400 eV and 750 eV. In the following studies, a magnetic field of 220 mT is considered, if not stated otherwise.



(a) (b)

Figure 4.17: (a) Correlation between the proton kinetic energy and detector position y for multiple magnetic flux densities B. For a given kinetic energy, variations of possible detector positions y arise due to the multiple particle pitch angles and, hence, gyration radii available. For the evaluation of E×B drifts, the mean proton kinetic energy T_{p} at a given position y, which is most representative of that energy, is considered for a magnetic field $B = 220\,\mathrm{mT}$. Figure (a) courtesy of Daniel Moser.

Table 4.2: Correlation between the mean initial kinetic energy T_p of the protons and the approximate detector position y for multiple magnetic fields B.

Magnetic Field B (mT)		150	200	220	300	400	800
		Detector Position y (cm)					
	10	0	0	0	0	0	0
Proton Kinetic Energy T_0 (eV)	400	6	4	3	3	2	1
	750	11	9	9	6	5	2

E×B Drift

The analytical E×B drift distance $D_{\mathrm{E\times B}}$ introduced in Eq. (3.7) is proportional to the ratio between the normal field component $E_\perp$[4] and the square root of the particle kinetic energy $T = T_0 - e(U - U_0)$:

$$D_{\mathrm{E\times B}} \propto \text{const} \cdot \frac{E_\perp}{\sqrt{T_0 - e(U - U_0)}}. \tag{4.1}$$

In the following, the ratio $r_{\mathrm{E\times B}}$, defined as

$$r_{\mathrm{E\times B}} = \frac{E_y}{\sqrt{T_0 - e(U - U_0)}}, \tag{4.2}$$

is evaluated to identify areas inside the detection region where particles experience significant E×B drifts. Here, both the normal electric field component E_y and its absolute value are considered. Fig. 4.18 shows $r_{\mathrm{E\times B}}$ evaluated in the y-z-plane ($x = 0\,\mathrm{m}$) for a proton of initial kinetic energy of $T_0 = 0\,\mathrm{eV}$ in setups A and B. In setup A, regions whit large ratios $r_{\mathrm{E\times B}}$ are present around the tips of the electrode entrance. Here, normal electric field components and electrostatic potentials are significant. Note that this regions are not directly located in the proton beam. In addition to the electrode tips, large values of the ratio $r_{\mathrm{E\times B}}$ are present at the edges of the electron detector in setup B. Here, normal electric field components are large while the electrostatic potential is small. Note that this region is directly crossed by low energetic protons.

The ratio $r_{\mathrm{E\times B}}$ is shown in Fig. 4.19 for setups A and B as a function of position z for multiple positions y at $x = 0\,\mathrm{m}$ for an initial proton kinetic energy of $T_0 = 0\,\mathrm{eV}$. Results show that the sign of the ratio $r_{\mathrm{E\times B}}$ changes in the proximity of the electrode entrance for all positions y in both setups, reflecting the change in orientation of the normal field component E_y. Since E_y increases for larger positions y, the amplitude of the ratio $r_{\mathrm{E\times B}}$ in setup A increases accordingly[5]. In setup B, $r_{\mathrm{E\times B}}$ has the smallest amplitude for $y = 0.05\,\mathrm{cm}$, corresponding to the electrode center. For larger distances from the electrode axis, the amplitude of $r_{\mathrm{E\times B}}$ increases with the normal electric field component E_y. The influence of the grounded electron detector on the ratio $r_{\mathrm{E\times B}}$ is reflected in the significant peak present at $y = 0.01\,\mathrm{m}$ at the location of the sensor, corresponding to $z = 0.2\,\mathrm{m}$.

To obtain an estimate of the distance by which protons drift inside the detection region, an integration of the area under the curve described by the ratio $r_{\mathrm{E\times B}}$, as shown in Fig. 4.19, is performed. The result is than multiplied by the constants in Eq. (3.7). The correlation between the detector position y and the mean proton kinetic energy T_0 for a magnetic field of 220 mT is

[4] The normal field component $E_\perp$ is defined by $\sqrt{E_\mathrm{x}^2 + E_\mathrm{y}^2}$.

[5] Studies of radial variations of the electrostatic potential performed in Section 4.3.2 have shown that potential inhomogeneities become significant outside the electrode region. Thus, protons gain kinetic energy at a different rates depending the areas (and, thus, position y) covered as they move towards the detector. This also affects the magnitude of the ratio $r_{\mathrm{E\times B}}$.

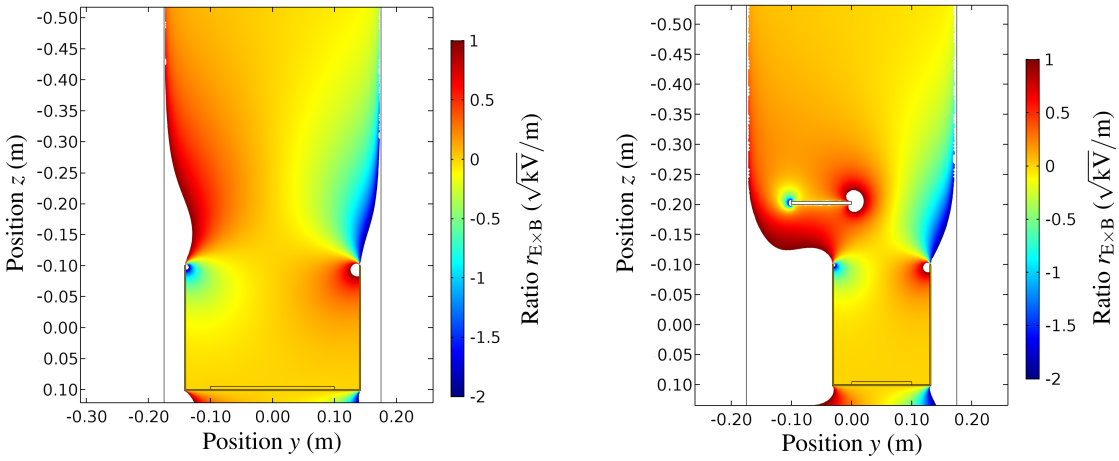


Figure 4.18: Ratio $r_{\mathrm{E\times B}}$ between the normal electric field component E_{y} and the square root of the electrostatic potential U in the y-z-plane at $x = 0\,\mathrm{m}$ for (a) detector setup A and (B) detector setup B. It can be seen that the ratio $r_{\mathrm{E\times B}}$ has large values as the electrode entrance edges in both detector setups. Additionally, large values of $r_{\mathrm{E\times B}}$ are induces at the electron detector edges of setup B. Note that the white areas represent values of $r_{\mathrm{E\times B}}$ outside the colorbar limits. Protons experience significant E×B drifts in the regions of high ratio $r_{\mathrm{E\times B}}$.

considered (see Table 4.2). Additionally, an overestimate of the E×B drift effect can be obtained if the absolute value of the ratio $r_{\mathrm{E\times B}}$ is considered in the integration. In this estimation, the direction of E×B drifts experienced by the particles is omitted.

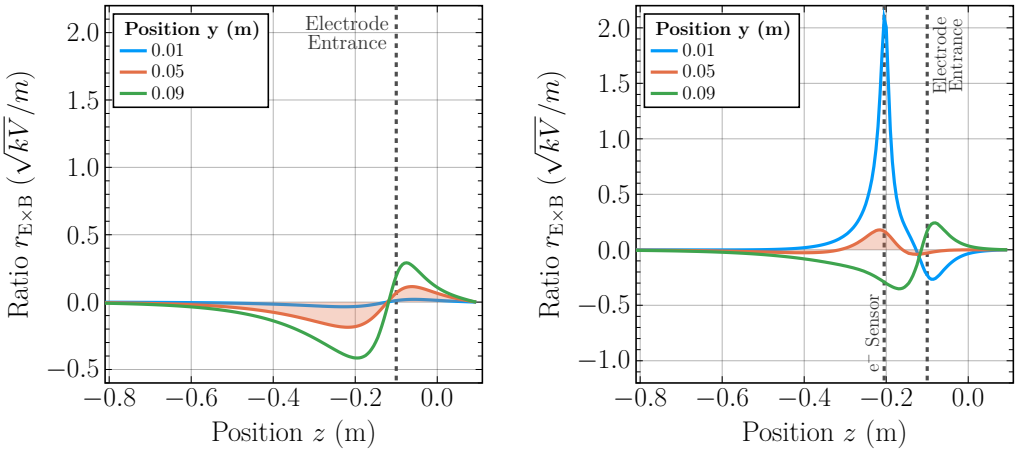
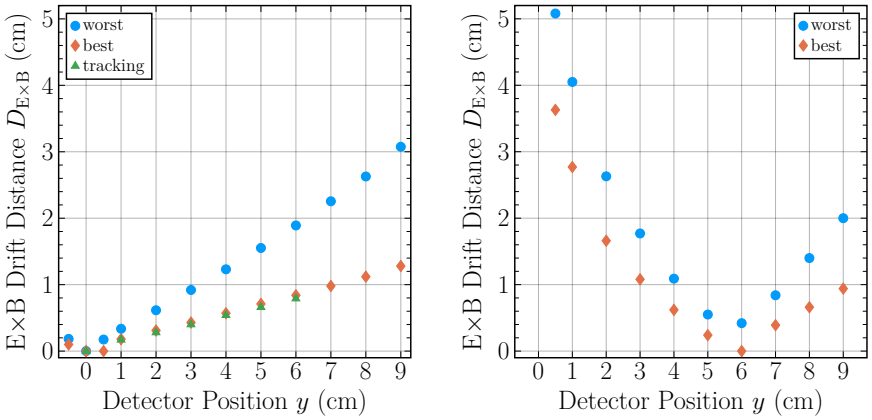


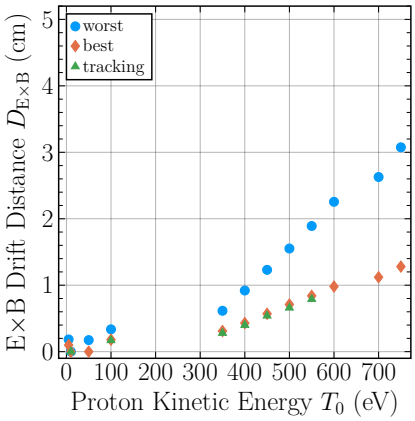
Figure 4.19: Ratio $r_{\mathrm{E\times B}}$ between the normal electric field component E_{y} and the square root of the electrostatic potential U as a function of position z for multiple position y in (a) detector setup A and (b) detector setup B. The electrode region is marked by the gray area in both detector setups. The location of the electron detector in setup B is indicated by the gray dashed line. A significant peak forms for $y = 0.01\,\mathrm{m}$ in the proximity of the electron sensor in setup B.

The integrated E×B drift distance $D_{\mathrm{E\times B}}$ as a function of the detector position y and the mean proton kinetic energy T_0 is shown in Fig. 4.20 for both setups. Here, both an integration over E_{y} and over its absolute value, labeled as best and worst case, respectively, has been considered. Results show that:

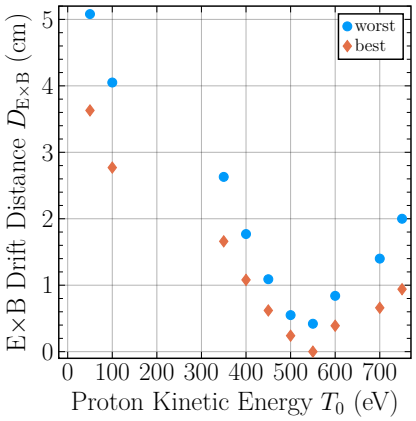


(a) Setup A

(b) Setup B



(c) Setup A



(d) Setup B

Figure 4.20: Distance $D_{\mathrm{E\times B}}$ by which protons drift inside the detection region when accelerated by the cylinder electrodes of setup A and B as a function of (a)−(b) detector position y and (c)−(d) proton initial kinetic energy T_0, evaluated according to Eq. (3.7). The drift distance is evaluated by assuming the integration over the normal field component $E_\perp$ (best) and over its absolute value (worst). A comparison between the two setups shows that low energetic protons moving close to the system central axis z experience small drifts in setup A. The drift distance $D_{\mathrm{E\times B}}$ increases approximately linear with position y and kinetic energy T_0 above 300 eV. In setup B, both low and high energetic protons drift by a significant amounts. Low energetic protons traverse a region of strongly non-uniform electric field at the electron detector of setup B.

- The distance $D_{\mathrm{E\times B}}$, by which the protons drift inside the detection region, varies strongly with the detector position y and the initial kinetic energy T_0 in both setups.
- A compensation of E×B drifts is reflected in the smaller drift distance experienced by protons in setups A and B if the orientation of the normal electric field component E_y is considered (best case).
- Setup A: Low energetic protons move on trajectories close to the central axis z, where normal electric field components are small, and experience small drifts. The drift distance increases approximately linearly for higher energetic protons which move at larger distances from the axis of symmetry.
- Setup B: High energetic protons drift by a smaller distance, compared those in setup A, while low energetic protons traverse regions of strongly non-uniform electric fields in the

vicinity of the electron detector and drift by a significant amount.

Note that the E×B drift distance obtained in the lower estimation in setup A fits well with the drift of the guiding center (denoted as "tracking" in Figs. 4.20a and 4.20c) obtained from particle-tracking simulations[6].

Both setups do not fulfill the electrode requirement connected to the suppression of E×B drifts. Protons drift by large distances resulting in a significant change of the spatial distribution of the proton drift distance spectrum. Geometrical and electrical properties of the two detection setups need to be adjusted to minimize the E×B drifts experienced by the decay protons as they move towards the sensor. The influence of such adjustments on the drift distance $D_{\mathrm{E\times B}}$ is studied in the following. For the evaluation of $D_{\mathrm{E\times B}}$, the absolute value of the normal electric field E_{y} is considered.

Adjustments to Setup A

To reduce the amount of E×B drift experienced by the higher energetic protons in setup A, the electrode diameter can be increased. By doing so, the edges of the electrode entrance, where the ratio $r_{\mathrm{E\times B}}$ has large values, are further away from the proton beam[7]. Fig. 4.21 shows the E×B drift distance $D_{\mathrm{E\times B}}$ as a function of the proton kinetic energy T_0 for multiple electrode diameters D. Effects of the diameter variation are largest for higher energetic protons which follow trajectories closer to the electrode walls. An increase of the electrode diameter from 28 cm to 30 cm results in a reduction of the drift distance by about 5 % to 2.9 cm for a particle of energy 750 eV. The trend shows that a further increase of the electrode diameter does not significantly reduce the E×B drift effect. Note that an adjustment of the electrode diameter affects other electrode requirements, such as the potential homogeneity, discussed in the previous sections.

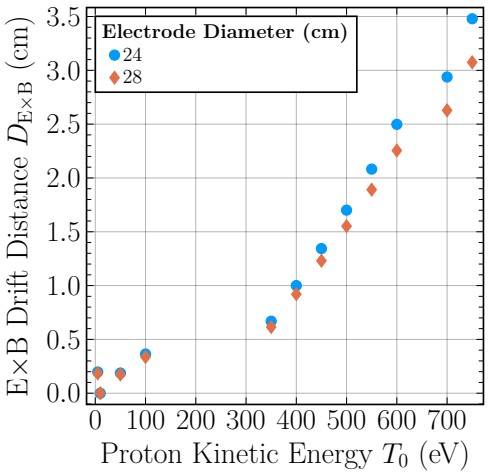


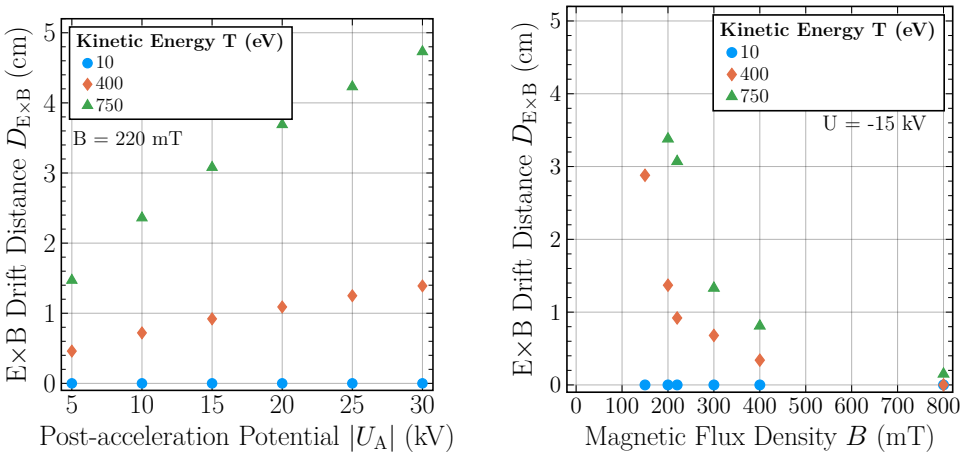
Figure 4.21: E×B drift distance $D_{\mathrm{E\times B}}$ as a function of the proton kinetic energy T_0 for multiple electrode diameters D in setup A. The drift distance decreases for protons of higher kinetic energies when the electrode diameter is increased. This is due to a larger distance between the proton beam and the electrode edges where the ratio $r_{\mathrm{E\times B}}$ has large values. Note that an increase of the electrode diameter does not affect the E×B drift experienced by low energetic protons which follow trajectories close to the electrode center.

[6] Tracking-simulations of protons were performed only sporadically for investigations of the electrode requirements discussed in the current chapter. An extensive analysis of the systematic effects introduced by the high voltage electrode is presented in Chapter 5 based on particle-tracking simulations in the context of a single measurement of the decay protons.

[7] Note that the electrostatic potential and electric field generated by the electrode also change. This in turn change the ratio $r_{\mathrm{E\times B}}$.

A significant reduction of the strength of the normal electric field components and, thus, of the drift distance $D_{\mathrm{E\times B}}$ can be achieved by choosing a lower post-acceleration potential U_{A}. The E×B drift distance $D_{\mathrm{E\times B}}$ as a function of the post-acceleration potential U_{A} is shown in Fig. 4.22a for multiple proton kinetic energies T_0. It can be seen that the drift distance increases with the applied post-acceleration potential. When the potential is decreased from 15 kV to 5 kV, a reduction of the E×B drift distance by 52 % to 1.5 cm is achieved for a particle of energy 750 eV. The required electrode post-acceleration potential depends, however, on the chosen detector technology and affects the detector performance.

The most effective tool to suppress E×B drifts is to increase the magnetic flux density B. An increase of the magnetic field results in a decrease of the particle beam size, as shown in Fig. 4.17a. Hence, high energetic protons follow trajectories closer to the central axis z, where normal electric field components are small. Additionally, E×B drifts are suppressed since the drift distance $D_{\mathrm{E\times B}}$ is indirectly proportional to the magnetic flux density B. Fig. 4.22b shows the relation between the magnetic flux density B and the drift distance $D_{\mathrm{E\times B}}$ for multiple proton kinetic energies T_0. Results show a decrease of $D_{\mathrm{E\times B}}$ with $1/B$, independent on the proton kinetic energy. It can be also seen that the dependence of the drift distance on the particle kinetic energy decreases for larger magnetic fields. For a proton with a kinetic energy of 750 eV, $D_{\mathrm{E\times B}}$ is reduced by 95 % to 0.15 cm when the magnetic flux density is increased from 220 mT to 800 mT.

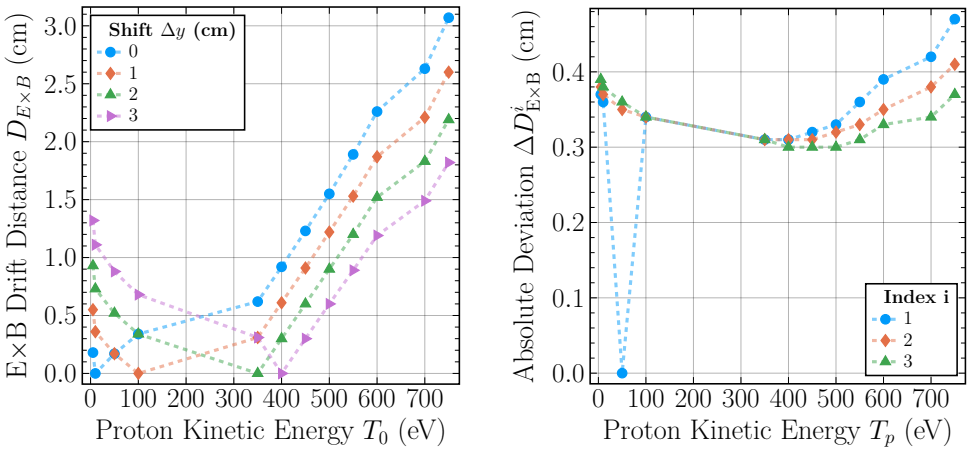


(a) (b)

Figure 4.22: E×B drift distance $D_{\mathrm{E\times B}}$ as a function of (a) the post-acceleration voltage U and (b) the magnetic flux density B for multiple proton kinetic energies T_0, considering detector setup A. The drift distance increases linearly for larger post-acceleration voltages and it decreases with $1/B$ for larger magnetic flux densities B.

Another option to further minimize the mean drift distance $D_{\mathrm{E\times B}}$ is to shift the proton (and electron) beam[8] and, hence, the detector in R×B drift direction. A shift of the proton beam changes the areas covered by the decay protons inside the detection region and, therefore, the electric field experienced by the particles. The E×B drift distance $D_{\mathrm{E\times B}}$ as a function of the proton kinetic energy T_0 is shown in Fig. 4.23a for multiple detector shifts Δy. A shift of the proton detector in the direction of negative position y results in an increase of the drifts experienced by low energetic protons. The opposite is observed for high energetic protons. The mean drift distance decreases when the detector is shifted by 3 cm. In such a detector setup, protons of mean kinetic energy 400 eV, which are the most abundant, are expected to arrive at the detector position $y = 0$ cm. This position corresponds to the electrode center. Here, the

[8] A shift of the particle beam is achieved by a shift of the aperture.



(a) (b)

Figure 4.23: (a) E×B drift distance $D_{\mathrm{E\times B}}$ as a function of the proton kinetic energy T_0 for multiple detector shifts Δy (corresponding to a shift of the proton beam) in detector setup A. The detector is shifted in negative y-direction. An overall reduction of the mean drift distance is achieved if the electron detector and, hence, the proton (and electron) beam are shifted by 3 cm. (b) Uncertainty in the determination of the drift distance $D_{\mathrm{E\times B}}$ induced by a misalignment of the electrode-detector system with respect to the proton beam : Absolute deviations $\Delta D^i_{\mathrm{E\times B}}$ of the approximated drift distance between two consecutive shifts of the sensor are largest for higher energetic protons.

electric field is aligned with the magnetic field for all positions z. Thus, such a proton experiences no E×B drifts. The distance by which a proton of 5 eV drifts increases by 675 % to 1.32 cm while that of a 750 eV proton decreases by 41 % to 1.82 cm.

From Fig. 4.23b additional information on the misalignment of the electrode-detector system with respect to the proton beam can be gained. It shows the absolute deviation $\Delta D^i_{\mathrm{E\times B}}$ of the E×B drift distance between two consecutive detector shifts Δy^i and Δy^{i-1}, defined as

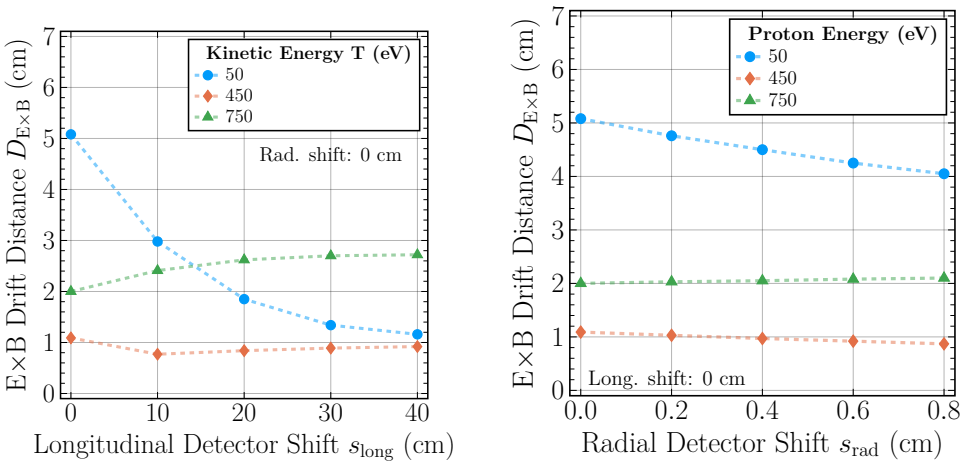
$$\Delta D^i_{\mathrm{E\times B}} = |D^i_{\mathrm{E\times B}} - D^{i-1}_{\mathrm{E\times B}}|. \tag{4.3}$$

The absolute deviation $\Delta D^i_{\mathrm{E\times B}}$ is small for a proton kinetic energy of 350 eV and increases for low and higher energetic protons. The effect of the misalignment is largest for high energetic protons. Note that 50 eV protons drift by the same amount in the setups where the beam is shifted by 0 cm and 1 cm. In the former setup, the proton enters the detection region at $y = 0.5$ cm while in the later setup it enters at $y = -0.5$ cm. Since the geometry is axially symmetric, electric fields experienced by the particle in the two setups are equal. Thus, $\Delta D^i_{\mathrm{E\times B}}$ is zero. The uncertainty in the E×B drift is below 0.5 mm for a detector misalignment of 1 mm.

Adjustments to Setup B

In detector setup B, low energetic protons experience large E×B drifts as they move towards the detector in a strongly inhomogeneous electric field. The E×B drift effect experienced by such protons can be minimized by shifting the electron detector in longitudinal or radial direction away from the electrode. When the electrode detector is shifted in longitudinal direction, it is located in a region of lower electrostatic potential and electric field strength. Thus, the ratio $r_{\mathrm{E\times B}}$ at the electron detector decreases (see Fig. 4.18b). The E×B drift distance $D_{\mathrm{E\times B}}$ as a function of the longitudinal electron detector shift s_{long} is shown in Fig. 4.24a for multiple proton kinetic energies T_0. When the electron detector is shifted by a distance of 40 cm away from its initial position, the distance by which a proton of energy 50 eV drifts decreases by 77 % to about 1 cm.

For high energetic protons, however, $D_{\mathrm{E\times B}}$ increases for larger detector shifts. This result in an increase of the drift distance by 36 % to 2.8 cm for a longitudinal shift of 40 cm and a proton of energy 750 eV.



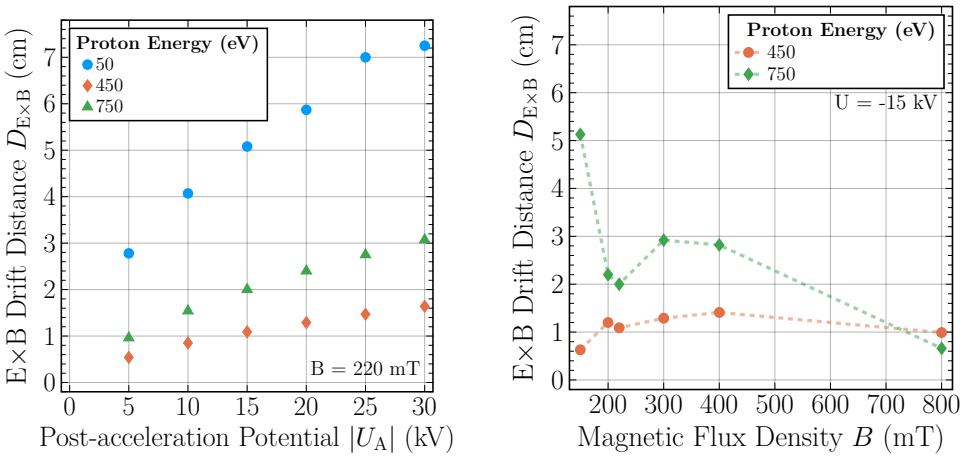
(a) (b)

Figure 4.24: E×B drift distance $D_{\mathrm{E\times B}}$ as a function of (a) longitudinal electron detector shift s_{long} and (b) radial electron detector shift s_{rad} in setup B. It can be seen that the detector shift affects the E×B drift experienced by the protons differently. (a) A longitudinal shift significantly reduces the drift by which protons of energy 50 eV drift. However, drifts experienced by high energetic protons increase. (b) The effect of a radial detector shift on the proton drift is similar to (a), although, effects are not as significant.

A radial electron detector shift also reduces the E×B drifts experienced by low energetic protons. This is shown in Fig. 4.24b for multiple proton kinetic energies T_0. When the electron detector is shifted radially away from the electrode, the edge of the detector which generates a high field ratio $r_{\mathrm{E\times B}}$ is further away from the proton beam. Therefore, low energetic protons experience a smaller E×B drift. The drift distance of a proton with a kinetic energy of 50 eV decreases by 20 % to about 4 cm when the electron detector is shifted by a radial distance of 0.8 cm away from its initial location. Such a detector shift does not affect the E×B drifts experienced by mean and high energetic protons significantly.

As in detector setup A, the electrode post-acceleration voltage and the magnetic flux density can be adjusted to reduce E×B drifts experienced by the protons. The E×B drift distance $D_{\mathrm{E\times B}}$ as a function of the post-acceleration potential $|U_{\mathrm{A}}|$ is shown in Fig. 4.25a for multiple proton kinetic energies T_0. The drift distance is reduced by 45 % to 2.8 cm for a proton of energy 50 eV when the post-acceleration potential is decreased from 15 kV to 5 kV. As previously mentioned, the required post-acceleration potential is based on the choice of the particle sensor.

An adjustment of the magnetic field affects the proton beam size and the mean proton kinetic energy T_{p} expected at detector position y according to Fig. 4.17 and Table 4.2. The drift distance $D_{\mathrm{E\times B}}$ as a function of the magnetic flux density B, evaluated for multiple proton initial kinetic energies T_0, is shown in Fig. 4.25b. A proton of initial energy 450 eV follows a trajectory closer to the grounded electron detector, where the field-to-potential ratio $r_{\mathrm{E\times B}}$ has large values (see Fig. 4.18b), if they are guided by a stronger magnetic field. Thus, drifts experienced by the proton increase for magnetic flux densities up to 400 mT. Results show that strong magnetic fields ($>$ 800 mT) are required to suppress drifts experienced by the decay protons in such a setup.



(a) (b)

Figure 4.25: E×B drift distance D as a function of (a) the post-acceleration voltage U and (b) the magnetic flux density B for multiple proton kinetic energies T_0, considering detector setup B. The drift distance increases linearly for larger post-acceleration voltages. Large magnetic fields are required to minimize drifts experienced by decay protons.

4.4 Summary

The goal of this chapter was to investigate the feasibility of a simultaneous measurement of the charged decay products based on studies of systematic effects induced by the post-acceleration electrode for protons. The design of the electrode should fulfill the requirements mentioned in Section 3.2. For these studies, two simple detector configurations were presented in Section 4.1: electrons and protons are either measured on a common detector surface (setup A) or on two spatially separated sensors (setup B). For the proton post-acceleration, cylindrical electrodes have been considered in both setups (Section 4.2). Both proposed setups affect the number of detected particles. To achieve the desired measurement sensitivity, the following effects need to be considered:

- Setup A: Low energetic electrons might be reflected by the post-acceleration potential applied at the electrode-detector system. The number of reflected electrons increases with the post-acceleration potential (see Fig. 4.2).

- Setup B: Low energetic protons might be lost due to shadowing by the electron detector. Considering only an axial separation between the two particle detectors and an electron and proton beam of width 10 cm, 0.5 cm of the proton beam is blocked by the electron sensor. First estimations show that the effect in the determination of the electron-antineutrino coefficient a is negligible.

Systematic effects studies have shown that not all requirements are fulfilled by the cylinder electrodes in the two proposed setups. Some of the key findings are mentioned in the following:

- **Homogeneity of the electrostatic potential**:

  While the electrostatic potential is more homogeneous across the proton beam in the vicinity of the proton sensor, inhomogeneities increase at larger distances from the detector. It was found that a small electrode diameter is required in the proximity of the proton sensor to improve the homogeneity of the electrostatic potential. The opposite holds for larger distances from the detector.

The grounded electron detector of setup B causes significant inhomogeneities of the electrostatic potential across the proton beam in its vicinity. An increase of the longitudinal and radial distance between the electron sensor and electrode improves the potential homogeneity in this plane. However, effects remain significant.

- **Electrostatic potential at large distances from the electrode**:

  Both electrodes generate electrostatic potentials which reach far into the detection region. It was found that both proposed setups require a detection region longer than 1.2 m to prevent electrostatic potentials above -10 mV from reaching into the R$\times$B drift region.

  Further, results have shown that adjustments of the electrode diameter or of the location of the electron detector of setup B are not effective in the reduction of the required detection region length.

- **Penning traps**:

  There are no Penning traps inside the detection region in setup A. However, a Penning trap for positively charged particles is present around the grounded electron detector in setup B. This trap is located in the path of both electrons and protons and has a maximum depth of 638 V. Its elimination is, therefore, crucial.

  It was found that the trap can be eliminated from both the electron and proton beam if the longitudinal distance between the electron detector and the electrode is 50 cm. A radial detector shift of 0.8 cm is sufficient to eliminate the trap from the proton beam. However, a significant trap still remains above the electron detector.

- **E$\times$B drift effect**:

  The electric field generated by the two electrodes inside the detection region is non-uniform and protons experience significant drifts. Results have shown:

  - Setup A: Medium and high energetic protons drift by larger distances compared to low energetic ones. They follow trajectories at larger distances from the axis of symmetry z where normal electric field components are large. It was found that a shift of the proton detector (and, thus, of the proton beam) inside the electrode in R$\times$B drift direction results in a decrease of the mean E$\times$B drifts experienced by the incoming protons.
  - Setup B: Low and high energetic protons experience significant drifts. The former follow trajectories close to the electron detector, where the ratio between the normal electric field components and the electrostatic potential is large. The mean drift experienced by such protons can be reduced if the longitudinal distance between the electron detector and the electrode is 50 cm.

  The most effective tools to minimize E$\times$B drifts experienced by protons in both setups are the post-acceleration potential U_A and the magnetic flux density B. The drift distance $D_{\mathrm{E}\times\mathrm{B}}$ is below 2 cm and 3 cm in setups A and B, respectively, for all protons if $U_\mathrm{A} = -5$ kV. An increase of B to 800 mT suppresses the drifts experienced by protons in both setups.

Results obtained for the E$\times$B drift effect represent are only an approximation (overestimation) of the drifts experienced by the decay protons, since no particle tracking simulations were performed, and represent an overestimation of this effect. Such simulations are crucial in future investigations of E$\times$B drift effects and of the adiabatic particle transport. These studies are performed in the next chapter, considering only the measurement of decay protons.

Investigations performed in this chapter showed that a simultaneous measurement of the decay electrons and protons is difficult to achieve, especially due to the large E×B drifts experienced by protons. However, promising results have been achieved in setup A when combined with a shift of the proton beam. In the following chapter, only the single measurement of the decay protons is considered. The focus lies on studies of systematic effects introduced by the post-acceleration electrode, using electric and magnetic field computations and particle-tracking simulations, to determine if a proton measurement is feasible.

Chapter 5

Electrode Designs for Single Proton Measurement

Studies presented in the previous chapter have shown that a simultaneous measurement of the charged decay particles is difficult to achieve, especially for protons. Systematic effects induced by the post-acceleration electrode, such as E×B drift effects experienced by the decay protons, need to be suppressed to make the proton measurement feasible. The focus of this chapter lies on the design of the post-acceleration electrode considering only the measurement of decay protons to gain a better understanding of these various effects. For the electrode optimization, particle-tracking simulations are performed in addition to electric field computations. These are crucial in the evaluation of the adiabatic particle transport and of E×B drift effects.

This chapter is divided into seven sections. For the proton post-acceleration, two electrode categories, cylinder electrode and field degrader, are proposed in Section 5.1. Geometrical and electrical setups of the proposed post-acceleration electrodes are introduced in Section 5.2. Studies of the electrostatic potential, adiabatic particle transport and of E×B drift effects are performed in Sections 5.3 to 5.5 for both electrode types based on the design criteria discussed in Section 3.2. In Section 5.6, effects of the particle beam size and shifts thereof on adiabaticity and E×B drifts are investigated. Finally, key findings are summarized in Section 5.7.

5.1 Possible Electrode Types

For the proton post-acceleration, two electrode types are proposed: cylinder electrode and field degrader. The geometries of the two electrodes, including the surrounding vacuum tube and the proton detector, are shown in Figs. 5.2 to 5.3. Before a detailed description of the proposed electrodes and their individual features is given, important geometrical parameters in the design of the detection system are reiterated.

As in the simultaneous particle measurement, important factors in the design of the detection system are:

- The alignment between the proton beam and the proton detector,
- the alignment between the proton beam (and, thus, proton sensor) and the post-acceleration electrode and
- the location of the electrode inside the surrounding vacuum tube.

The location of the proton detector inside the detection region is chosen to allow a complete mapping of the proton beam onto the sensor surface. For simplicity, a symmetric distribution of the proton drift distance spectrum shown in Fig. 3.2 around the system central axis z is considered.

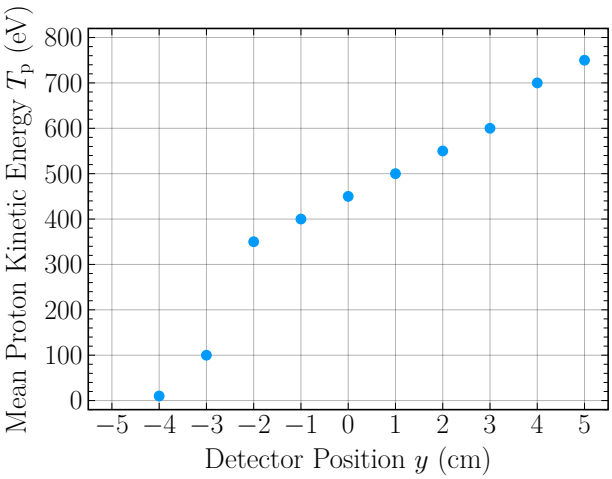


Figure 5.1: Correlation between the mean proton kinetic energy T_p and detector position y for a symmetrical distribution of the proton drift distance spectrum around the central axis z at the end of the R×B drift region. Here, a shift of the mean energy spectrum shown in Fig. 4.17b by 4 cm in negative direction y and a magnetic field of 220 mT are considered.

The correlation between the mean proton kinetic energy T_p and detector position y is shown in Fig. 5.1 for a sensor of size 10×10 cm^2 and a magnetic field of 220 mT. This enables the construction of an axial symmetric geometry of the detection region, with the post-acceleration electrode and the proton sensor centered inside the vacuum tube.

5.1.1 Cylinder Electrode

Fig. 5.2a shows a top view in the x-y-plane of the axially symmetric detection region, composed of the proton detector, cylinder electrode and vacuum tube. A cross section of the system is shown in Fig. 5.2b in the y-z-plane for $x = 0$ cm. The proton detector is embedded into the electrode end plate. The electrode of diameter D and length L can be operated in two distinct modes, depending on the material used to manufacture the cylinder:

- Cylindrical conductor: The cylinder is a conductor and, thus, all electrode surfaces have a constant electrostatic potential U_A.
- Resistive cylinder: The cylinder is composed of a resistive foil. The surface potentials applied at the electrode entrance and end plate differ, creating a linear potential gradient across the electrode surface in the direction z[1].

The proton detector and the electrode end plate are operated at the common surface potential U_A, independent on the operation mode. The electrode-detector system is surrounded by the vacuum tube of diameter D_vt, which is operated at ground potential. A distance d is considered between the electrode and the vacuum tube to avoid large electric fields in this region.

5.1.2 Field Degrader

The detection region composed of the vacuum tube, field degrader and proton sensor is schematically shown in Fig. 5.3. Fig. 5.3a shows a top view of the axially symmetric geometry in the x-y-plane. The electrode of length L is composed of a circular end plate (labeled as R_1) and multiple rings (labeled as R_2 to R_N) as shown in Fig. 5.3b in the y-z-plane for $x = 0$ m. Compared

[1] A linear surface potential builds up across the electrode walls only for an ideal resistor material.

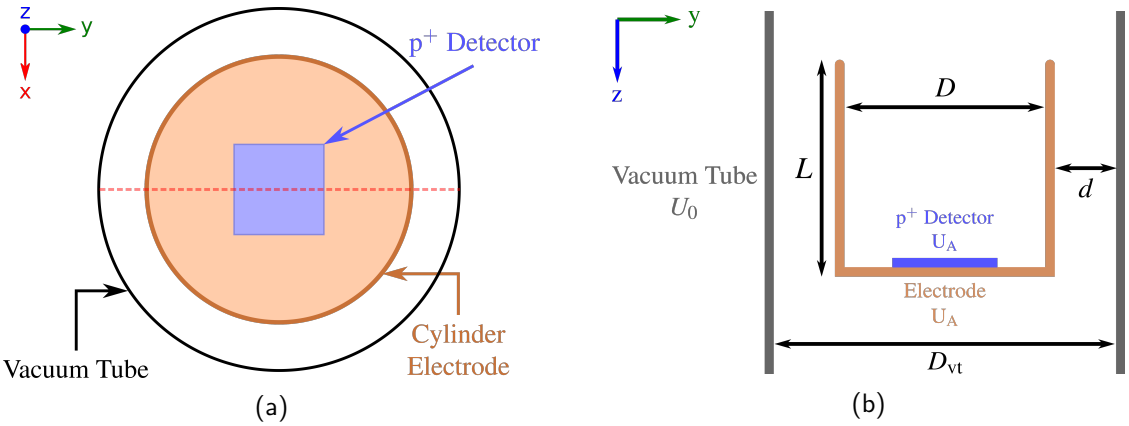


Figure 5.2: (a) A top-view in the x-y-plane of the detection system composed of the vacuum tube (black), cylinder electrode (orange) and proton detector (blue). The geometry is axially symmetric. (b) A sketch of the detection system in the y-z-plane at $x = 0\,\mathrm{m}$, indicated by the red, dashed line in (a). The proton detector is embedded into the electrode end plate. The electrode of diameter D and length L can be operated at constant surface potential surface potential U_A or in resistive mode. In the latter, the electrode entrance ring and end plate are operated at different surface potentials U_0 and U_A, respectively, inducing a potential gradient along the axis z. The vacuum tube of diameter D_vt is connected to zero-potential.

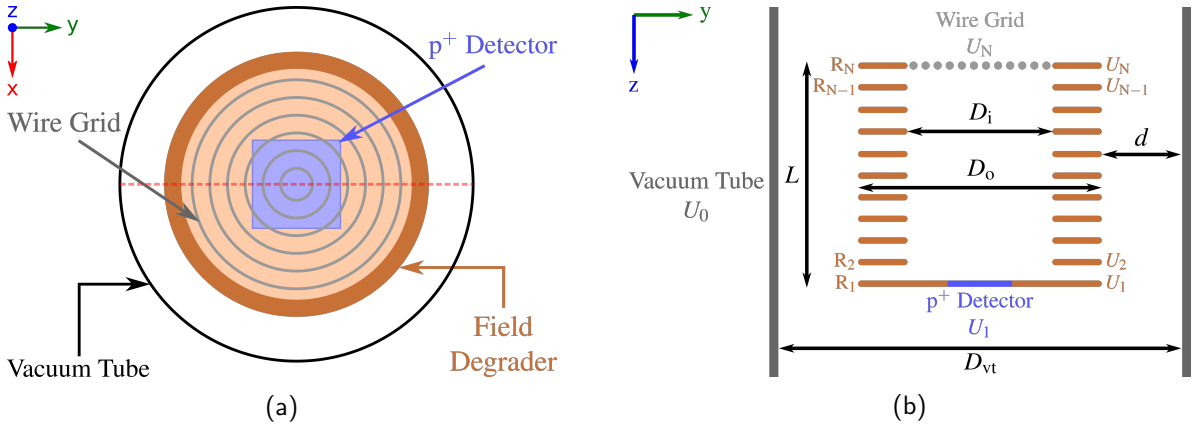


Figure 5.3: (a) A top-view in the x-y-plane of the detection system composed of the vacuum tube (black), field degrader (orange) and proton detector (blue). A detachable circular wire grid (gray), composed of M wires, is located at the electrode entrance. The geometry is axially symmetric. (b) A sketch of the detection system in the y-z-plane at $x = 0\,\mathrm{m}$, indicated by the red, dashed line in (a). The proton detector is embedded into the electrode end plate. The electrode of length L is composed of multiple rings, labeled as $\mathrm{R_i}$, which have a surface potential U_i. The electrode has an inner diameter D_i and outer diameter D_i. The vacuum tube of diameter D_vt is connected to zero-potential.

to the cylinder electrode, the modular structure of the field degrader offers more flexibility in the design of the post-acceleration electrode. The surface potentials U_{i} applied at the corresponding electrode component $\mathrm{R_i}$ can be individually adjusted to obtain a more precise control over the electrostatic potential induced by the electrode. The electrode rings are equidistant, with a distance d_{n} between consecutive rings. The electrode is further characterized by the inner diameter D_{i} and the outer diameter D_{o}. The vacuum tube of diameter D_{vt} surrounds the electrode and is connected to ground potential.

One optional feature of the field degrader is the concentric wire grid which can be attached at the electrode entrance. The grid consist of M individual wires of diameter D_{wire} separated by the distance d_{m} which toghether with the inner electrode diameter D_{i} determine the wire grid transmissibility T (see Appendix D.3.1). The electrode and the vacuum tube of diameter D_{vt} are separated by a distance d to avoid the emergence of large electric fields in this region.

To illustrate the working principles of the proposed electrodes, the electrostatic potential generated by the various electrodes inside the detection region is shown in the following section for a fixed set of geometrical and electrical electrode parameters.

5.2 Geometrical and Electrical Setup of the Detection System

The geometrical and electrical parameters of the cylinder electrode and field degrader in the standard configuration are defined in the following. The cylinder electrode has a diameter of 24 cm and is 20 cm long. A post-acceleration potential of -15 kV is applied at the electrode surface. The geometrical and electrical properties of the field degrader are listed in Table 5.1. For both setups, a vacuum tube of diameter $D_{\mathrm{vt}} = 350$ cm and length $L = 400$ cm is considered.

Table 5.1: Geometrical and electrical parameters of the field degrader in the standard configuration.

Description		
Number of rings		11
Distance between rings d_{n} (cm)		2
Inner diameter D_{i} (cm)		24
Outer diameter D_{o} (cm)		28
Length L (cm)		20
	U_1	-15
Ring potential U_{i} (kV)	U_{11}	0
	ΔU	1.5

Fig. 5.4 shows the electrostatic potential U induced by the two electrodes inside the detection region, evaluated in the y-z-plane for $x = 0$ m. Decay protons enter the detection region from the top and are distributed symmetrically around the system central axis z. Some of the most important features of the electrostatic potential are listed below:

- Protons experience a decreasing potential and are accelerated as they move towards the sensor. The decrease rate of the potential is largest either in the region outside the electrode (cylinder) or inside the electrode (field degrader).
- Equipotential lines are curved, especially at larger distances from the proton sensor, indicating inhomogeneities of the electrostatic potential.

- The cylinder electrode generates large potentials in regions far from the electrode. In contrast, the gradual increment of the surface potential applied at the rings of the field degrader prevents large potentials to extend as far into the detection region.

Additionally, since the electrostatic potential increases rapidly inside the field degrader, a larger fraction of backscattered protons might be reflected back towards the sensor before they leave the electrode when compared to the cylinder electrode.

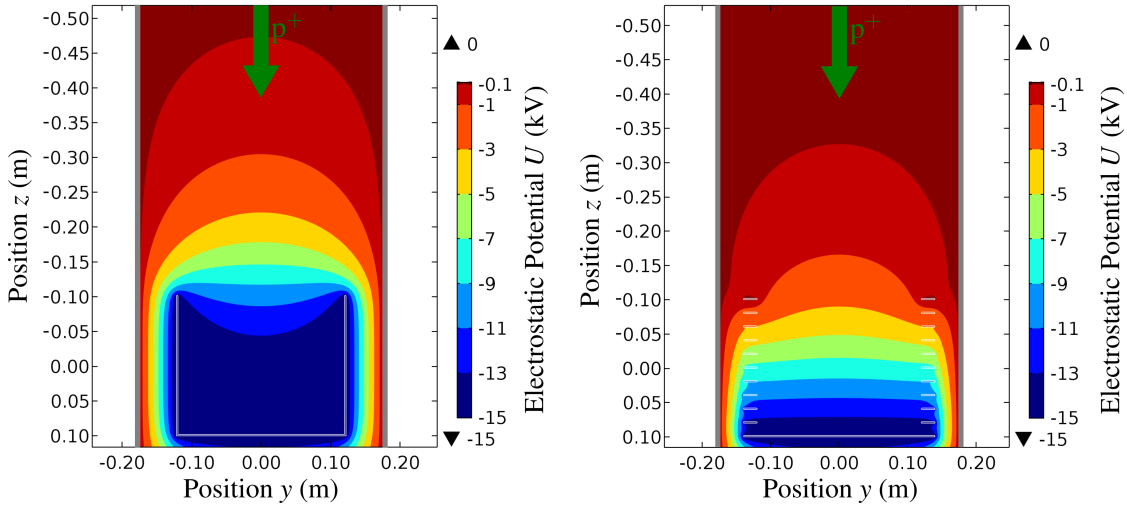


Figure 5.4: Electrostatic potential U generated by (a) the cylinder electrode and by (b) the field degrader inside the detection region, viewed in the y-z-plane for $x = 0$. The decay particles enter the detection region from the top, as indicated by the green arrow. (a) The cylinder electrode generates a slowly varying potential inside the electrode. The potential extends away from the electrode into the detection region where it increases rapidly. (b) Due to the surface potential gradient applied across the electrode rings, U increases rapidly inside the field degrader. A comparison between (a) and (b) shows that the potential generated by the field degrader does not extend as far into the detection region.

To adapt this feature for the cylinder electrode, it can be modified into a resistive cylinder system. This is shown in Fig. 5.5a for the same set of geometrical parameters as the cylinder electrode. In such a setup, the electrode entrance is grounded while the surface potential applied at the electrode end plate is chosen as $-15\,\text{kV}$ which results in a potential gradient across the electrode walls (in direction z). The resistive cylinder induces an electrostatic potential in the detection region with a profile similar to the field degrader.

A more effective shielding of the detection region from large potentials can be obtained if the concentric wire grid is attached at the entrance ring of the field degrader. The electrostatic potential generated by such an electrode is shown in Fig. 5.5b in the y-z-plane of the detection region for $x = 0\,\text{cm}$. The geometrical and electrical properties of the electrode correspond to the ones listed in Table 5.1. The wire grid is composed of 22 equidistant concentric wires ($d_\text{m} = 5.14\,\text{mm}$) of cross section diameter $D_\text{wire} = 200\,\mu\text{m}$ and has a transmissibility T of 0.964 (see Fig. D.4). The wire grid and the electrode entrance ring are operated at the same surface potential U_{11}. Note that equipotential lines are less curved inside the field degrader when the electrode is used in combination with the circular wire grid. This indicates that the potential is more homogeneous in this region when compared to the other electrodes considered. This feature is discussed in more detail in Section 5.3.4.

Detailed studies of various features of the electrostatic potential mentioned above are performed in the following section to determine if the two proposed electrode types fulfill the corresponding design requirements discussed in Section 3.2.

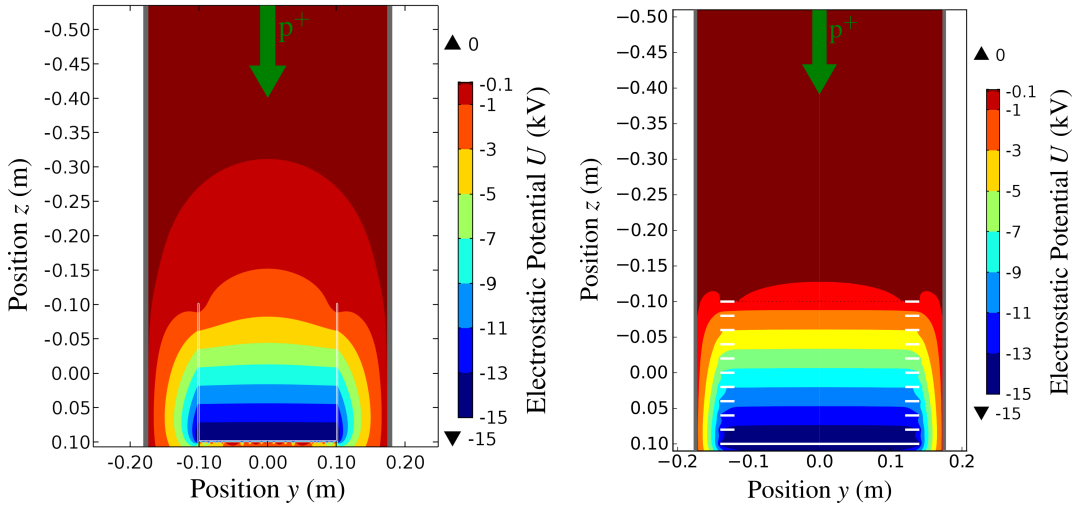


Figure 5.5: Electrostatic potential U generated inside the detection region by (a) the resistive cylinder and by (b) the field degrader including a concentric wire grid, viewed in the y-z-plane for $x = 0\,\text{m}$. (a) The geometrical parameters of the resistive cylinder are identical with those of the cylinder electrode. The electrode entrance ring is operated at zero-potential while the end plate is operated at $-15\,\text{kV}$. This results in a potential gradient across the electrode walls. The potential generated inside the detection region is similar to the field degrader (see Fig. 5.4b). (b) The wire grid attached at the entrance ring of the field degrader consists of 22 equidistant, concentric wires and is operated at zero-potential. It can be seen that the wire grid shields the detection region from large electrostatic potentials.

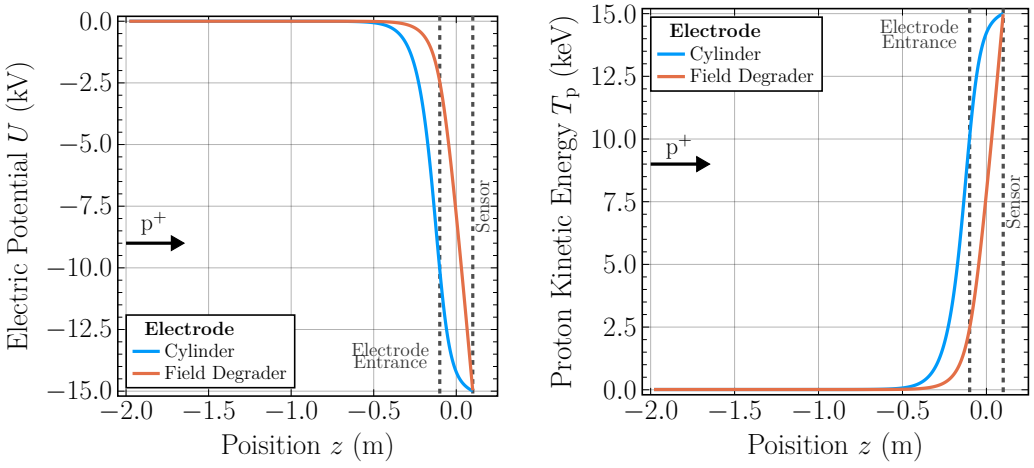
5.3 Electrostatic Potential Studies

The proton post-acceleration electrode should be designed to fulfill all requirements presented in Section 3.2. In the following, multiple features of the electrostatic potential generated by the proposed electrodes inside the detection system are studied. Results presented in this section were obtained from simulations performed in COMSOL Multiphysics and from particle-tracking simulations performed in C++. The standard configurations of the cylinder electrode and field degrader are considered throughout this section, if not stated otherwise.

5.3.1 Proton Post-acceleration

The electrode should provide the electrostatic potential required to post-accelerate decay protons to detectable energies. The electrostatic potential U along the trajectory of a tracked proton is shown, together with the proton kinetic energy T_p, in Fig. 5.6 for the cylinder electrode and field degrader in the standard configuration (see Section 5.2). The proton starts 4 cm off-axis with an initial kinetic energy $T_0 = 10\,\text{eV}$ (see Fig. 5.1) and a pitch angle θ_0 of 0° and moves in a magnetic field $B = 220\,\text{mT}$. The proton experiences a decreasing electrostatic potential as it moves towards the sensor. Its kinetic energy increases only slowly in regions far from the electrode, where the electrostatic potential is small, in both setups. The rate at which the proton is accelerated by the two electrodes as it moves closer to the sensor differs in the two setups:

- Cylinder electrode: The proton experiences a rapidly decreasing potential as it approaches the electrode entrance and gains a large fraction of its final kinetic energy over this region. As the proton moves closer to the sensor, where the potential becomes more homogeneous (in direction z), the proton gains kinetic energy at a slower rate.



(a) (b)

Figure 5.6: (a) Comparison of the electrostatic potential U experienced by a proton of initial kinetic energy $T_0 = 10\,\text{eV}$, pitch angle $\theta_0 = 0°$ and phase angle $\varphi_0 = 0°$ when accelerated by the cylinder electrode and field degrader in the corresponding standard configuration described in Section 5.2. (b) Comparison of the kinetic energy T_p gained by the proton when accelerated by the cylinder electrode and field degrader. The proton moves in the direction of increasing position z, as indicated by the black arrow. Locations of the electrode entrance and of the proton sensor are marked by gray, dashed lines. A comparison between the two setups shows that the proton gains the largest fraction of its final kinetic energy either before entering the electrode or afterwards, depending on the chosen electrode type.

- Field degrader: The rapid potential decrease inside the field degrader causes the proton to gain the largest fraction of its final kinetic energy after it enters the electrode.

Both electrodes provide the electrostatic potential required to accelerate decay protons to detectable energies.

According to Fig. 5.6a, the electrostatic potential generated by the field degrader does not extend as far into the detection region, compared to the cylinder electrode. Investigations of the electrostatic potential in regions far from the electrode and its influence on the detection region length are performed in the following section.

5.3.2 Electrostatic Potential at large Distances from the Electrode

One electrode design criteria mentioned in Section 3.2.5 requires that the electrostatic potential at the interface between the detection and the R×B drift region should not exceed $-10\,\text{mV}$. The electrostatic potential reaches this value at an axial distance d_f of about 104 cm and 90 cm from the electrode entrance for the cylinder electrode and the field degrader, respectively[2]. This yields a minimum required detection region length of about 1.3 m and 1.1 m for the two electrode configurations[3].

A short detection region facilitates the design of a homogeneous magnetic field, required to ensure adiabatic particle transport, and reduces the complexity and costs of the coil design. Multiple adjustments to the cylinder electrode can be considered to further constrain the electrostatic

[2]Values obtained in the evaluation of the distance d_f are limited by the number of boundary elements chosen in the segmentation of the electrode and vacuum tube. Results obtained for the cylinder electrode are consistent with those obtained in studies of the simultaneous particle measurement in Section 4.3.3 (see setup A).

[3]As already mentioned in Section 3.2.5, the minimum detection region length is determined by the sum of the electrode length L and the distance d_f.

potential outside the electrode and, thus, minimize the required detection region length. Such studies are performed in the following for both electrode types.

Adjustments to the Cylinder Electrode

Two trivial geometrical parameters, the electrode diameter and length, can be adjusted to reduce the distance d_f and, thud, the detection region length. Results show, however, that these tools are not very effective. The relation between the electrode diameter D and the distance d_f from the electrode entrance where the potential reaches $-10\,\mathrm{mV}$ is shown in Fig. 5.7a. Results show that d_f decreases by only $1\,\%$ to 103 cm if the electrode diameter is reduced from 24 cm to 16 cm. Studies performed for various lengths L of the cylinder electrode show that a reduction of the electrode length does not affect the potential generated at large distances from the electrode. The potential reaches $-10\,\mathrm{mV}$ at a distance of 104 cm from the electrode entrance, independent on the electrode length. Although the minimum length of the detection region can be reduced if a short electrode is considered, such an adjustment of the cylinder electrode affects the electrostatic potential inside the electrode. This is discussed in more detail in Section 5.3.4.

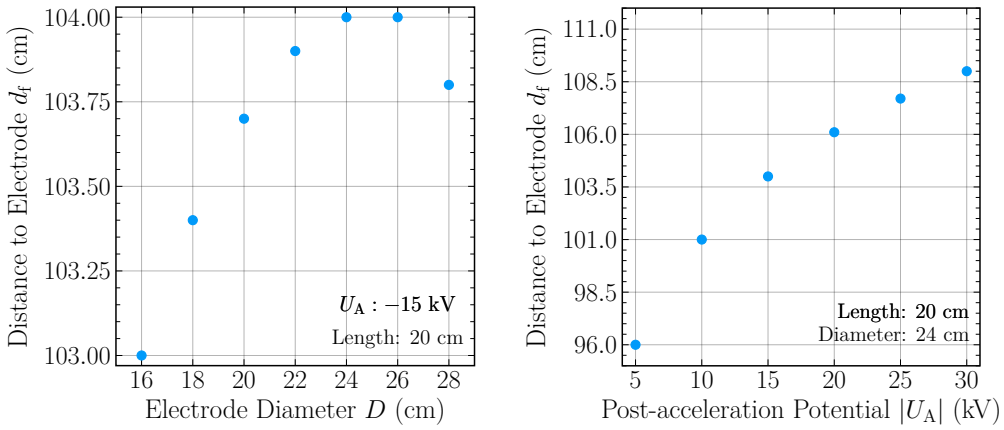


Figure 5.7: Distance d_f, measured from the entrance of the cylinder electrode, where the electrostatic potential U reaches $-10\,\mathrm{mV}$ as a function of (a) the electrode diameter D and (b) the proton post-acceleration potential $|U_\mathrm{A}|$. While effects of a reduction of the electrode diameter on the distance d_f are small, d_f decreases by about $7\,\%$ when the post-acceleration potential $|U_\mathrm{A}|$ is reduced from 15 kV to 5 kV.

One more effective parameter in the reduction of the electrostatic potential induced by the electrode inside the detection region and, thus, of the minimum detection region length is the post-acceleration potential U_A. Fig. 5.7b shows the relation between the distance d_f and the post-acceleration potential $|U_\mathrm{A}|$. The distance d_f increases with the square root of the potential U_A. If the post-acceleration potential is decreased from 15 kV to 5 kV, a reduction of d_f by 8 cm is achieved. Although such an electrical electrode setup is more effective for the reduction of the required detection region length, one crucial factor in the choice of the post-acceleration potential remains the sensor technology used to measure the decay protons.

If a large post-acceleration potential is required, the detection region can be shielded more effectively from large electrostatic potentials using a resistive cylinder. Studies of the electrostatic potential generated by such an electrode have shown similarities to the potential induced by the field degrader (see Fig. 5.5a). The distance between the electrode and the radial plane where the potential reaches $-10\,\mathrm{mV}$ is reduced by about $15\,\%$ to 88 cm when compared to a cylinder electrode operated at a constant surface potential of 15 kV. This yields a minimum length of the

detection region of about 1.1 m.

Adjustments to the Field Degrader

Several geometrical and electrical parameters of the field degrader can be adjusted to shield the detection region from large electrostatic potentials induced by the electrode. The shielding is more effective if the surface of the entrance ring, which is operated at zero-potential, is increased. This corresponds to a reduction of the electrode inner diameter for a fixed outer diameter. In the following study, a variation of the inner diameter D_i is considered for an electrode outer diameter D_o and length L of 28 cm and 20 cm, respectively. The distance between the outer electrode walls and the vacuum tube is, therefore, constant. Fig. 5.8 shows an approximately linear dependence of the distance d_f on the electrode inner diameter. A reduction of d_f by 8 % to about 83 cm is achieved when the inner diameter is decreased from 24 cm to 16 cm.

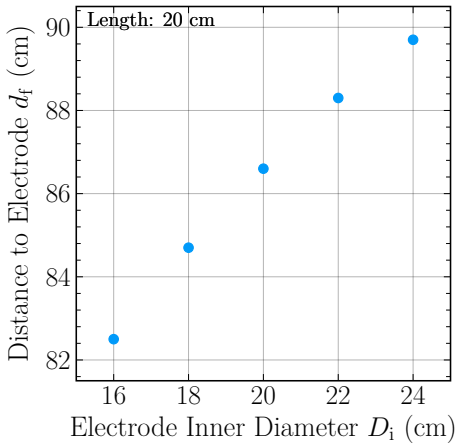


Figure 5.8: Distance d_f, measured from the entrance of the field degrader, where the electrostatic potential U reaches -10 mV as a function of the electrode inner diameter D_i. Note that the outer electrode diameter D_o is fixed to 28 cm and that the variation of the inner diameter represents a variation of the electrode ring width w. Results show that the distance d_f increases approximately linearly with the electrode inner diameter D_i.

A significant shielding of the region outside the electrode is achieved when the circular wire grid is attached to the electrode entrance (see Fig. 5.5b). In such a setup, the axial distance d_f between the electrode and the point at which the potential reaches -10 mV decreases by about 20 % to 72 cm when compared to the field degrader without a wire grid (standard configuration). Therefore, a detection region with a minimum length of 1 m can be considered.

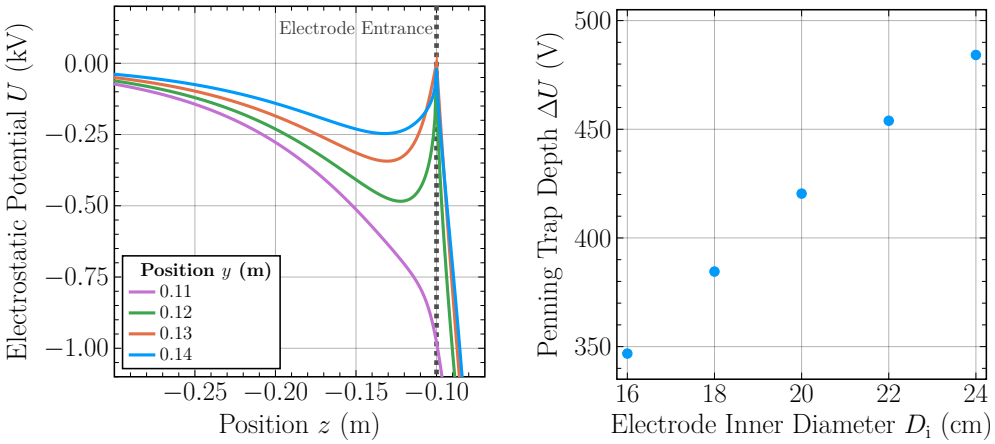
One disadvantage of such an electrode setup are particle traps induced by the grounded wire grid which can emerge inside the proton beam. The same holds for the grounded electrode entrance ring. This is discussed in more detail in the following section.

5.3.3 Particle Traps

The detection region, especially the areas covered by the decay protons, should be free of particle traps. This requirement is fulfilled if the cylinder electrode, which is operated at constant surface potential, is considered for the proton post-acceleration. This condition is not met in a detection system consisting of the proposed field degrader. The entrance ring, which is operated at zero-poential, constrains the electrostatic potential in its vicinity and causes the formation of a Penning trap. Fig. 5.9a shows the electrostatic potential in this region as function of position z for multiple positions y at $x = 0$ m. There are no particle traps inside the electrode (corresponding to $y < 0.12$ m) and, hence, across the proton beam (see also Fig. 5.4b). However,

the electrostatic potential has a minimum along magnetic field lines for $y = 0.12\,\mathrm{m}$, $0.13\,\mathrm{m}$ and $0.14\,\mathrm{m}$, corresponding to the radial position of the electrode entrance ring, which indicates the presence of a Penning trap above the ring. The largest trap depth is reached at the inner ring edge ($y = 0.12\,\mathrm{m}$) with a depth ΔU of $484\,\mathrm{V}$.

Additional Penning traps are present at the entrance of the field degrader if the wire grid is attached to the electrode. These traps are directly located inside the proton beam and have a depth ΔU of about $105\,\mathrm{V}$. To avoid the accumulation of residual gas ions and suppress background effects, it is crucial to eliminate these traps. In the following, effects of multiple electrode parameters on the Penning trap depth ΔU are studied for the field degrader with and without the wire grid.



(a) (b)

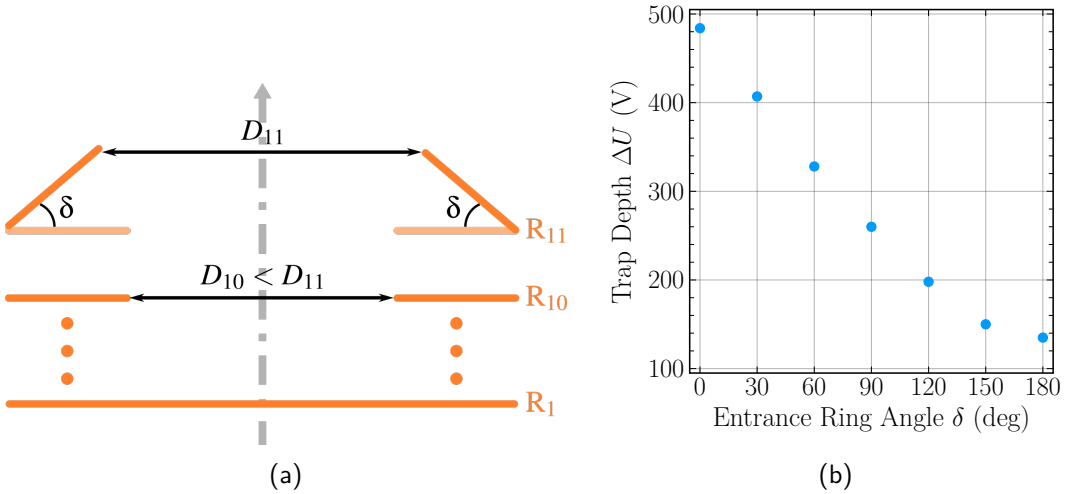
Figure 5.9: (a) Electrostatic potential U in the vicinity of the entrance ring of the field degrader as a function of position z for multiple positions y. The dashed gray line marks the location of the grounded entrance ring. The ring extends from $y = 0.12\,\mathrm{m}$ to $0.14\,\mathrm{m}$ and $y = 0.11\,\mathrm{m}$ lies inside the electrode. It can be seen that the potential has a minimum in front of the grounded entrance ring for positions y $0.12\,\mathrm{m}$ to $0.14\,\mathrm{m}$, indicating the presence of a Penning trap. There are no traps inside the electrode ($y = 11\,\mathrm{m}$) and, thus, in the regions covered by the decay protons. The Penning trap has the largest depth at the inner edge of the entrance ring with a depth $\Delta U = 484\,\mathrm{V}$. (b) Penning trap depth ΔU as a function of the electrode inner diameter D_i. The trap depth decreases linearly with the electrode diameter D_i.

Electrode Inner Diameter

A decrease of the electrode inner diameter, corresponding to an increase of the ring surface, results in a more effective shielding of the detection region from large electrostatic potentials. Thus, such an adjustment can be considered to minimize the depth of the Penning trap present above the entrance ring. Fig. 5.9b shows the trap depth ΔU as a function of the electrode inner diameter D_i evaluated at the inner ring edge (at $y = 0.12\,\mathrm{m}$ and $x = 0\,\mathrm{m}$). It can be seen that the relation between the trap depth and the electrode diameter is linear. A reduction of ΔU by about $28\,\%$ to $347\,\mathrm{V}$ is obtained if the electrode inner diameter is decreased from $24\,\mathrm{cm}$ to $16\,\mathrm{cm}$. Although the depth of the Penning trap decreases for smaller electrode inner diameters, its spatial spread increases. This is due to an increase of the electrode ring surface. Additionally, higher energetic protons follow trajectories much closer to the inner ring edge, where the trap is located, if the electrode inner diameter is small. To avoid such effects, rotations of the electrode entrance ring can be considered.

Electrode Entrance Ring Rotation

A rotation of the entrance ring, as shown in Fig. 5.10a, pulls the trap further away from the proton beam and shields the sensor optically from background emitted by the particle trap. Fig. 5.10b shows the trap depth ΔU as a function of the tilt angle δ evaluated at the inner edge of the entrance ring (at $x = 0\,\mathrm{m}$). For rotations up to 90°, ΔU decreases linearly with the tilt angle δ. Although the trap depth decreases by 46 % to 260 V if the ring is tilted by 90°, ΔU remains significant.



(a) (b)

Figure 5.10: (a) The entrance ring (R_{11}) of the field degrader can be tilted away from the proton beam by an angle δ to minimize the depth of the Penning trap present above the grounded ring. (b) Penning trap depth ΔU as a function of the tilt angle δ of the electrode entrance ring. Results show that the trap depth decreases approximately linearly with the tilt angle δ.

Wire Grid: Wire Diameter and Number of Wires

The depth of the Penning traps present above the concentric wires of the wire grid field degrader depends, among other parameters, on the wire diameter and the number of wires. Investigations of the trap depth ΔU for multiple wire diameters and numbers of wires show:

- Wire diameter D_{wire}: ΔU increases to 146 V and 180 V if the wire diameter is reduced from 200 µm to 100 µm and 50 µm, respectively.
- Number of wires: ΔU increases to 222 V and 420 V if the number of wires is decreased from 22 to 5. This corresponds to an increase of the distance between two wires d_{wire} from 5.14 mm to 10.24 mm and 20.64 mm.

Note that these wire grid parameters affect the wire grid transmissibility as shown in Appendix D.3.1.

Although the proposed adjustments to the field degrader achieve a reduction of the Penning trap depth, further optimizations are required for its elimination. One additional factor in the electrode optimization is the homogeneity of the electrostatic potential induced by the post-acceleration electrode. This aspect is discussed in more detail in the following section.

5.3.4 Homogeneity of the Electrostatic Potential

The electrostatic potential generated by the post-acceleration electrode inside the detection region should be homogeneous in every x-y-plane covered by the decay protons. A measure for the homogeneity of the electrostatic potential is the relative potential deviation ΔU_{rel} defined in Eq. (3.6). The homogeneity of the electrostatic potential is evaluated in radial cross sections of the proton beam at multiple distances from the detector for the cylinder electrode and field degrader in the standard configuration. The electrostatic potential U_{ref} is evaluated at the center of the proton beam ($y = x = 0\,\mathrm{m}$) at a given axial position z.

Fig. 5.11 shows the relative potential deviation $|\Delta U_{\mathrm{rel}}|$ as function of position y at a distance of 1 cm above the proton detector, corresponding to $z = 0.09\,\mathrm{m}$, for both electrodes. Since both detection setups are axially symmetric, it is sufficient to investigate effects only for positive positions y. A comparison of the cylinder electrode and field degrader shows that potential deviations across the proton beam are smaller if the field degrader is considered. However, both electrodes show good potential homogeneity, with variations $|\Delta U_{\mathrm{rel}}|$ well below 1 %.

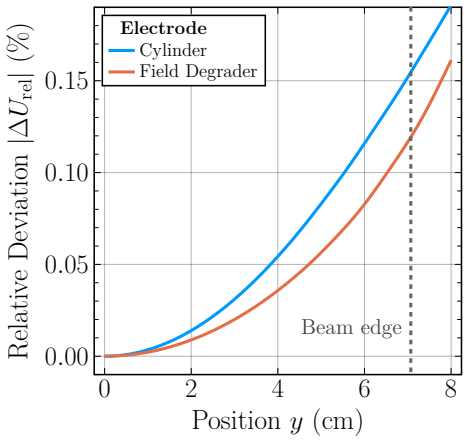


Figure 5.11: Comparison of the relative deviation of the electrostatic potential $|\Delta U_{\mathrm{rel}}|$ for the cylinder electrode and the field degrader as a function of radial position y evaluated at a distance of 1 cm above the proton detector. The edge of the proton beam is marked by the gray, dashed line. The electrostatic potential is homogeneous across the proton beam in both electrode setups, with a maximum relative deviation at the beam edge well below 1 %. Input data for U_{ref}: $-14.95\,\mathrm{kV}$ and $-14.27\,\mathrm{kV}$ for the cylinder electrode and field degrader, respectively.

Electrostatic potential studies at larger distances from the proton detector have shown that the radial potential variations always increases monotonically with position y. For the following investigations, the maximum relative deviation $|\Delta U_{\mathrm{rel}}^{\mathrm{max}}|$ is evaluated at the proton beam edge. Table 5.2 shows $|\Delta U_{\mathrm{rel}}^{\mathrm{max}}|$, together with the corresponding reference potential U_{ref}, evaluated at multiple distances d_{s} from the proton sensor. Inhomogeneities of the electrostatic potential increase at larger distances d_{s} in both setups. At a distance of 20 cm, corresponding to the position of the electrode entrance, the potential generated by the cylinder electrode is more homogeneous. This trend is observed also at larger distances from the electrode. In regions far from the electrode ($d_{\mathrm{s}} = 80\,\mathrm{cm}$), both electrodes generate an electrostatic potential of similar homogeneity.

Both electrodes generate a homogeneous potential in the vicinity of the proton sensor. In order to minimize relative potential deviations at larger distances from the sensor, an adjustment of the electrode geometry is required. In the following, the influence of various geometrical electrode parameters on the maximum relative potential deviation $|\Delta U_{\mathrm{rel}}^{\mathrm{max}}|$ is studied for the cylinder electrode and the field degrader.

Table 5.2: Relative deviation $|\Delta U_{\mathrm{rel}}^{\mathrm{max}}|$ of the electrostatic potential, evaluated at the edge of the proton beam, and the corresponding reference potential U_{ref}, evaluated at various distances d_{s} from the proton sensor for the cylinder electrode and field degrader. The electrode entrance is located at a distance d_{s} of 20 cm above the proton detector.

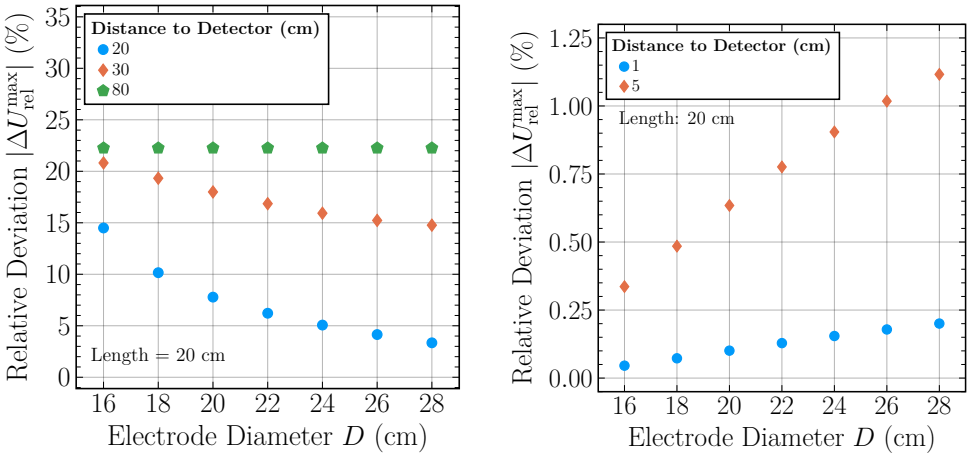
	Cylinder		Field Degrader	
d_{s} (cm)	U_{ref} (V)	$\lvert\Delta U_{\mathrm{rel}}^{\mathrm{max}}\rvert$ (%)	U_{ref} (V)	$\lvert\Delta U_{\mathrm{rel}}^{\mathrm{max}}\rvert$ (%)
1	−14,947.2	0.16	−14,269.5	0.12
5	−14,692.6	0.9	−11,373.3	0.7
20	−9936.8	5.07	−2604.9	20.52
30	−3723.2	15.93	−607.1	25.26
80	−4.2	22.26	−0.6	22.14

Adjustments to the Cylinder Electrode

The homogeneity of the electrostatic potential at large distance from the proton detector can be improved by adjusting the electrode diameter. The maximum relative potential deviation $|\Delta U_{\mathrm{rel}}^{\mathrm{max}}|$ as a function of the electrode diameter D is shown in Fig. 5.12a, evaluated at multiple distances d_{f} from the sensor. The electrode length is fixed to 20 cm. It can be seen that inhomogeneities in the potential can be reduced at larger distances from the sensor if the electrode diameter is increased from 24 cm to 28 cm. The maximum relative deviation $|\Delta U_{\mathrm{rel}}^{\mathrm{max}}|$ decreases by 34 % and 7 % to about 3 % and 15 % at a distance of 20 cm and 30 cm from the proton detector. An increase of the electrode diameter does not affect the potential generated by the electrode at a distance of 80 cm from the detector. The trend shows that improvements observed for $|\Delta U_{\mathrm{rel}}^{\mathrm{max}}|$ become smaller for larger electrode diameters. One disadvantage of a wide electrode are, however, larger potential variations in regions close to the proton detector. Fig. 5.12b shows $|\Delta U_{\mathrm{rel}}^{\mathrm{max}}|$ as a function of the electrode diameter D, evaluated at a distance of 1 cm and 5 cm above the sensor. Despite an increase of radial potential variations with increasing electrode diameter, the potential shows good homogeneity in this electrode region, with $|\Delta U_{\mathrm{rel}}^{\mathrm{max}}|$ of 0.2 % and 1.1 % for an electrode with diameter 28 cm. This represents an increase of $|\Delta U_{\mathrm{rel}}^{\mathrm{max}}|$ by 30 % and 23 %, respectively.

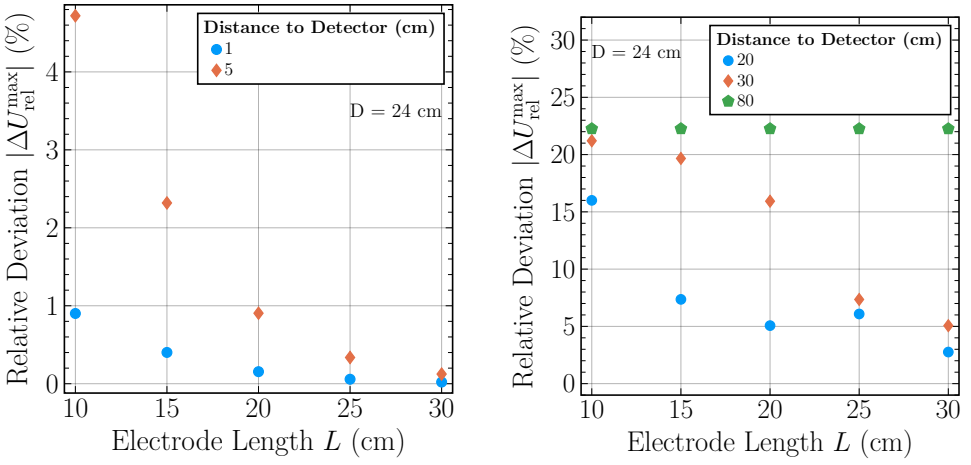
One alternative to improve the overall potential homogeneity is to increase the electrode length. The relative potential deviation $|\Delta U_{\mathrm{rel}}^{\mathrm{max}}|$ evaluated at small distances from the proton detector is shown in Fig. 5.13a for multiple lengths L of the electrode of diameter 24 cm. A reduction of $|\Delta U_{\mathrm{rel}}^{\mathrm{max}}|$ by 86 % to 0.02 % and 0.12 % is achieved at a distance of 1 cm and 5 cm above the sensor, respectively, if the electrode length is increased to 30 cm. In such a setup, strong improvements of the potential homogeneity are also observed at larger distances from the sensor, as shown in Fig. 5.13b. The relative deviation $|\Delta U_{\mathrm{rel}}^{\mathrm{max}}|$ decreases by 46 % to about 3 % at the distance $d_{\mathrm{s}} = 20$ cm. In this electrode setup, $|\Delta U_{\mathrm{rel}}^{\mathrm{max}}|$ is estimated to about 5 % at a distance of 30 cm above the sensor, which corresponds to the location of the electrode entrance. This result is consistent with the one obtain for the cylinder electrode of length $L = 20$ cm at a distance $d_{\mathrm{s}} = 20$ cm and, thus, at the electrode entrance. This indicates that inhomogeneities of the electrostatic potential remain significant at the entrance of the cylinder electrode, independent on its length. The homogeneity of the electrostatic potential in regions far from the electrode is not significantly affected by the electrode length.

So far, only the cylinder electrode operated at a constant surface potential has been considered. The electrode can be also operated in resistive mode, as described in Section 5.2, to obtain a similar profile of the electrostatic potential to the field degrader. A comparison of the relative potential deviation $|\Delta U_{\mathrm{rel}}^{\mathrm{max}}|$ between the two operation modes of the cylinder electrode



(a) (b)

Figure 5.12: Maximum relative deviation $|\Delta U_{\mathrm{rel}}^{\mathrm{max}}|$ of the electrostatic potential as a function of the cylinder electrode diameter D evaluated at multiple distances d_{s} above the proton sensor. It can be seen that an electrode of small diameter generates a more homogeneous potential inside the electrode region (b). However, in order to avoid large potential inhomogeneities at larger distances from the sensor at, a wider electrode is required (a).



(a) (b)

Figure 5.13: Maximum relative deviation $|\Delta U_{\mathrm{rel}}^{\mathrm{max}}|$ of the electrostatic potential as a function of the cylinder electrode length L, evaluated at multiple distances d_{s} above the proton sensor. It can be seen that a longer electrode generates a more homogeneous potential both at at small and large distances from the sensor. The smallest mean relative potential deviation is obtained for an electrode of length $L = 30\,\mathrm{cm}$.

shows a decrease by 63 % and 43 % to 0.06 % and 0.51 % at a distance of 1 cm and 5 cm from the detector, respectively. On the other hand, $|\Delta U_{\mathrm{rel}}^{\mathrm{max}}|$ increases by 346 % to about 21 % at a distance of 20 cm from the detector.

Results show that radial variations of the electrostatic potential in the vicinity of the proton sensor can be significantly reduced either if a long cylinder electrode or if a resistive cylinder is considered. Further electrode optimizations are, however, required to minimize potential variations at larger distances from the sensor.

Adjustments to the Field Degrader

As for the cylinder electrode, a smaller inner diameter of the field degrader can be chosen to achieve a better potential homogeneity inside the field degrader. However, variations of the electrostatic potential increase at larger distances from the proton sensor. The relative potential deviation $|\Delta U_{\mathrm{rel}}^{\mathrm{max}}|$ is shown in Fig. 5.14a as a function of the electrode inner diameters D_{i} at a distance of 1 cm and 5 cm from the proton sensor. All other electrode parameters are defined as in the standard configuration. Results show that the electrostatic potential at small distances from the proton sensor is most homogeneous when a field degrader with an inner diameter of 16 cm is considered. A further decrease of the inner diameter would require a reduction of the beam and detector size. Potential inhomogeneities at larger distances from the proton detector increase significantly if a smaller inner diameter is chosen, as shown in Fig. 5.14b. Here, $|\Delta U_{\mathrm{rel}}^{\mathrm{max}}|$ increases by about 166 % and 35 % to 55 % and 34 % at a distance of 20 cm and 30 cm from the sensor. The electrode inner diameter does not significantly affect the homogeneity of the electrostatic potential in regions far from the electrode. As in the design of the cylinder electrode, an optimization of the electrode diameter is required to balance effects inside and outside the electrode. The modular design of the field degrader offers more flexibility in achieving this.

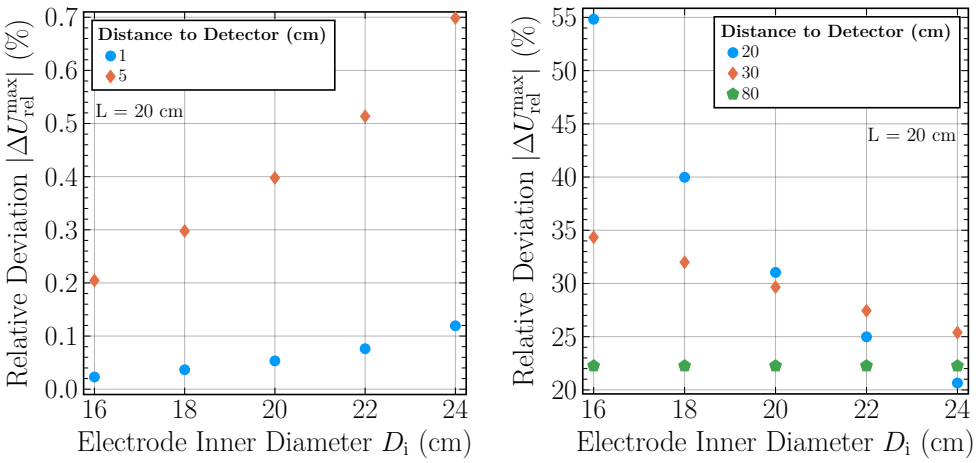


Figure 5.14: Maximum relative deviation $|\Delta U_{\mathrm{rel}}^{\mathrm{max}}|$ of the electrostatic potential as a function of the field degrader inner diameter D_{i}, evaluated at multiple distances above the proton detector. The electrode length L and the electrode outer diameter D_{o} are fixed to 20 cm and 28 cm. While a small inner diameter of the field degrader is required to minimize $|\Delta U_{\mathrm{rel}}^{\mathrm{max}}|$ at small distances from the sensor, the opposite holds for large distances.

One possible adjustment to avoid large radial variations of the potential at the electrode entrance is to increase the inner diameter by tilting the entrance ring by an angle δ, as shown in Fig. 5.10a. Note that such an adjustment increases the length of the field degrader. Fig. 5.15 shows the relative potential $|\Delta U_{\mathrm{rel}}^{\mathrm{max}}|$ as a function of the tilt angle δ evaluated at a distance of 20 cm and 30 cm from the proton detector[4]. It can be seen that $|\Delta U_{\mathrm{rel}}^{\mathrm{max}}|$ decreases rapidly with increasing tilt angle δ. For a tilt of 90°, a reduction of $|\Delta U_{\mathrm{rel}}^{\mathrm{max}}|$ by 13 % and 4 % to 18 % and 24 % is achieved at a distance of 20 cm and 30 cm, respectively. Such an adjustment causes an increase of potential variations in the vicinity of the proton detector. However, effects are small and variations of the potential across the beam remain below 1 % in this region.

To balance effects at small and large distances from the sensor, rotations of multiple electrode rings can be considered. Studies presented in the following consider a gradual increase of the electrode inner diameter from the electrode end plate towards the electrode entrance. To achieve

[4]The evaluation of $|\Delta U_{\mathrm{rel}}^{\mathrm{max}}|$ is performed at the inner edge of the entrance ring for $x = 0$ m.

this, a setup in which the angle δ_i between two consecutive electrode rings increases by 5°, with δ_1 = 0° and δ_{11} = 50° at rings R1 and R11, respectively. The relative change $|\Delta U_\mathrm{rel}^\mathrm{max}|$ decreases by 19 % and 11 % to about 0.1 % and 0.6 % at a distance of 1 cm and 5 cm from the proton sensor, respectively, compared to the standard configuration of the field degrader. A better homogeneity of the electrostatic potential is obtained also at larger distances from the detector, with relative changes of the potential of 16 % and 25 % at a distance of 20 cm and 30 cm, respectively.

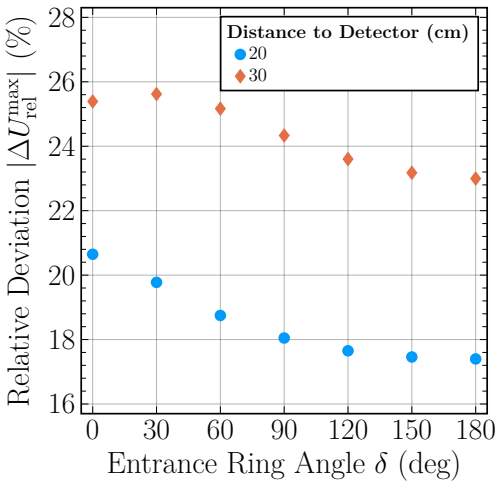


Figure 5.15: Maximum relative deviation $|\Delta U_\mathrm{rel}^\mathrm{max}|$ of the electrostatic potential as a function of the tilt angle δ of the field degrader entrance ring, evaluated at a distance of 20 cm and 30 cm above the detector. Inhomogeneities of the electrostatic potential at larger distances from the sensor can be reduced by tilting the electrode entrance ring away from the central axis z, as shown in Fig. 5.10a.

One additional feature of the field degrader is the concentric wire grid which can be attached at the electrode entrance. The wire grid, operated at the same surface potential as the entrance ring, constrains the potential inside the electrode and minimizes potential inhomogeneities present in these regions. Relative potential deviations $|\Delta U_\mathrm{rel}^\mathrm{max}|$, evaluated at a distance of 1 cm and 5 cm from the proton detector, decrease significantly to 0.05 % and 0.18 %, respectively, if this feature is considered. However, the electrostatic potential extends into the detection region between the wires, as shown in Fig. 5.16a in the y-z-plane for x = 0 m. The electrostatic potential in the wire plane and in its vicinity is strongly inhomogeneous. The largest inhomogeneities are present in the wire plane at z = 0.1 m. Here, ΔU_rel reaches a maximum of 27.8 % between the wires (see Fig. 5.16a).

The electrostatic potential generated by the electrode in the wire grid plane depends on geometrical parameters such as the number of wires and their diameter. To improve the potential homogeneity in the wire plane, the number of wires can be reduced to increase the distance d_wire between consecutive wires. In the following, wire grids composed of 22, 11 and 5 concentric wires, which are separated by a distance d_wire of 5.14 mm, 10.24 mm and 20.64 mm, respectively, are considered. Alternatively, the wire diameter D_wire and, thus, the surface of the circular wires can be decreased to reduce inhomogeneities of the electrostatic potential present in the wire plane. Wire grids composed of 22 individual wires of diameter 50 µm, 100 µm and 200 µm are considered. Results show that:

- Number of wires: A decrease of the number of wires from 22 to 11 and 5 results in a reduction of the $|\Delta U_\mathrm{rel}^\mathrm{max}|$ to about 19 % and 14 %, respectively.
- Wire diameter D_wire: A decrease of the wire diameter from 200 µm to 100 µm and 50 µm results in a reduction of $|\Delta U_\mathrm{rel}^\mathrm{max}|$ to about 20 % and 18 %.

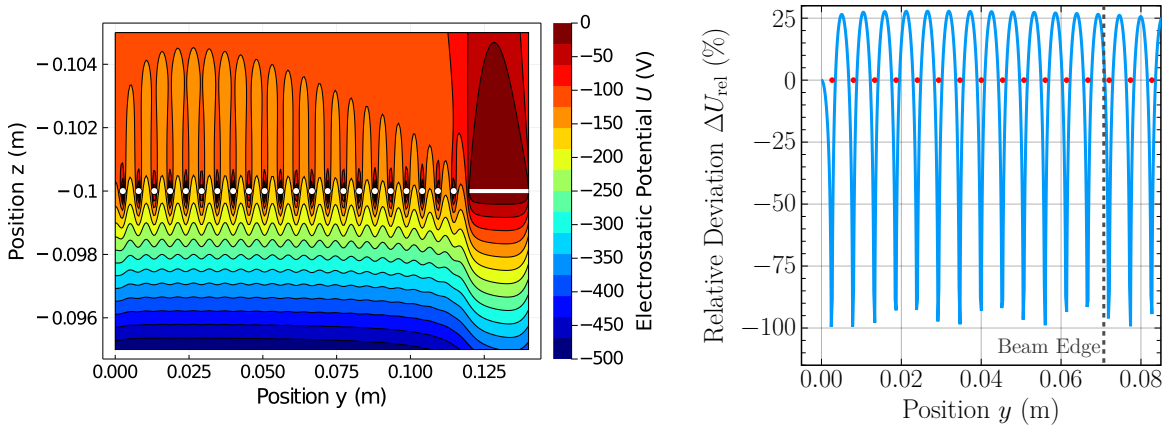


Figure 5.16: (a) Electrostatic potential U generated by the wire grid field degrader, evaluated in the y-z-plane for $x = 0\,\mathrm{m}$. (b) Relative deviation ΔU_{rel} of the electrostatic potential evaluated as a function of position y at the wire grid of the field degrader. The proton beam edge is marked by the dashed, gray line. The grounded wire grid generates a region of strongly inhomogeneous potential at the electrode entrance. Input data U_{ref}: $-134.8\,\mathrm{V}$.

Studies of the electrostatic potential induced by the cylinder electrode and field degrader performed in this section show that radial potential variations are small in the vicinity of the proton sensor, with $|\Delta U_{\mathrm{rel}}^{\mathrm{max}}| < 1\,\%$ evaluated at distances $d_{\mathrm{s}} \leq 5\,\mathrm{cm}$. However, potential variations increase at larger distances from the sensor in both setups. Large potential variations during the period of one particle gyration might break the invariance of the particle magnetic moment and make the particle transport non-adiabatic. The adiabatic transport of decay protons inside the detection region is studied, based on particle-tracking simulations, for both electrode types in the following section.

5.4 Adiabatic Particle Transport Studies

A detailed study of the adiabatic particle transport relies on tracking of protons in the electromagnetic field of the detection region. Adibaticity simplifies investigations of systematic effects and enables an analytical description of particle properties such as kinetic energy and pitch angle. To ensure an adiabatic motion of the decay protons, variations of the electric and magnetic fields experienced by the protons over one gyration period need to be sufficiently small. For the investigations performed in this section, a spatial distribution of the protons inside the detection region according to Fig. 5.1 and a magnetic field of 220 mT are considered, if not stated otherwise. The cylinder electrode and field degrader setups correspond to the standard configurations given in Section 5.2[5]. The magnetic field is provided by a cylindrical coil with a length of 10 m and a minimum and maximum radius of 0.22 m and 0.29 m which encloses the vacuum tube.

The orientation of the electric field E induced by the cylinder electrode and field degrader inside the detection region is shown in Fig. 5.17, evaluated in the y-z-plane for $x = 0$. Results presented in Section 5.3.4 have shown that the electrostatic potential inside the field degrader is more homogeneous, compared to the cylinder electrode. The same is observed for the electric field. Non-uniform fields are present in regions outside the electrode in both setups. Normal field components vanish at the axis of symmetry z and increase for larger distances from the axis.

[5]Due to software restrictions, investigations of the resistive cylinder are not included in this and the following sections. However, the electrostatic potential and, thus, the electric field generated by such an electrode is similar to the field degrader.

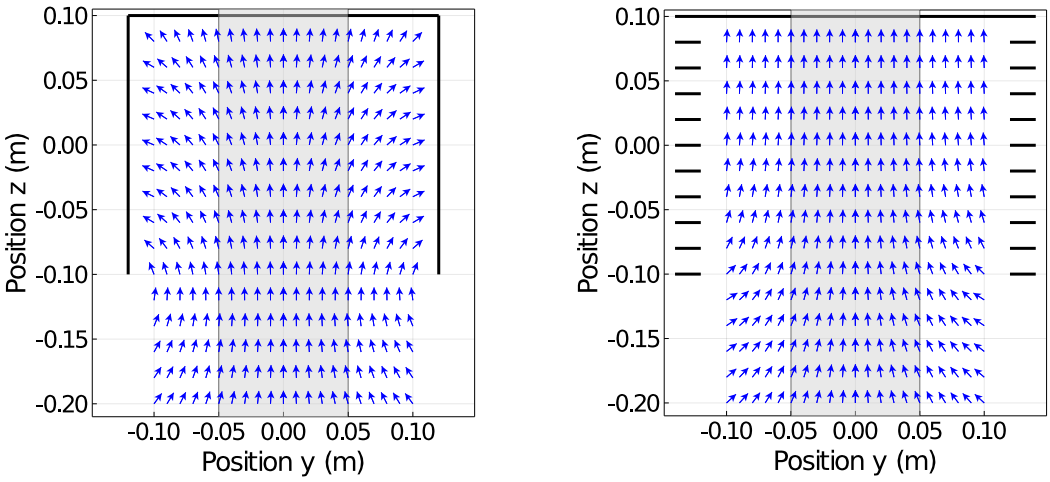


Figure 5.17: Electric field $\boldsymbol{E}$ generated inside the detection region by the (a) cylinder electrode and (b) field degrader, shown across the y-z-plane for $x = 0\,\mathrm{m}$. The area covered by the proton beam is marked in gray. Protons move in the direction of increasing position z. Note that the length of the arrows does not depict the electric field strength. A comparison of the two setups shows that the electric field generated by the field degrader is more uniform across the proton beam inside the electrode. The field along the central axis z (for $y = 0\,\mathrm{m}$) has no normal components since the geometry of both setups is axially symmetric.

Large variations of the electric field during the period of one particle gyration break the invariance of the particle magnetic moment and the particle transport can not be described in the adiabatic approximation. The electric field generated by the post-acceleration electrode and the guiding magnetic field should fulfill the adiabatic conditions mentioned in Eq. (2.13). The magnetic field inside the detection region is designed to fulfill this condition (see Fig. D.1). In the following, the electric field and variations thereof are evaluated along the trajectories of decay protons.

Fig. 5.18a shows a comparison of the electric field norm E experienced by a proton which starts 4 cm off-axis with initial kinetic energy $T_0 = 10\,\mathrm{eV}$, pitch angle $\theta_0 = 45°$ and phase angle $\varphi_0 = 0°$ when accelerated by the cylinder electrode and field degrader[6]. The proton traverses a region of weak electric fields at large distances from the electrode entrance in both setups. As it approaches the electrode entrance, it experiences a rapidly increasing field. A comparison of the electric field in the proximity of the electrode entrance and inside the electrode shows:

- Cylinder electrode: The electric field reaches a maximum at the electrode entrance and decreases rapidly inside the electrode, where the electrostatic potential (see Fig. 5.6a) and, thus, the field become more homogeneous.

- Field degrader: The proton experiences a monotonically increasing electric field as it moves towards the sensor. Note that the electric field generated by the electrode does not extends as far into the detection region, compared to the cylinder electrode.

The electric field generated by both electrodes changes significantly along the particle trajectory. Such field gradients should be small to ensure an adiabatic transport of the protons.

[6]We mention that the trajectories of the simulated protons presented in this and the following section end 1 cm before the particles reach the electrode end plate. This is due to a software restriction for electrostatic potential calculation very close to the electrode end plate. To obtain comparable results for all geometries presented in this chapter, all particle trajectories end at position $z = 0.09\,\mathrm{m}$.

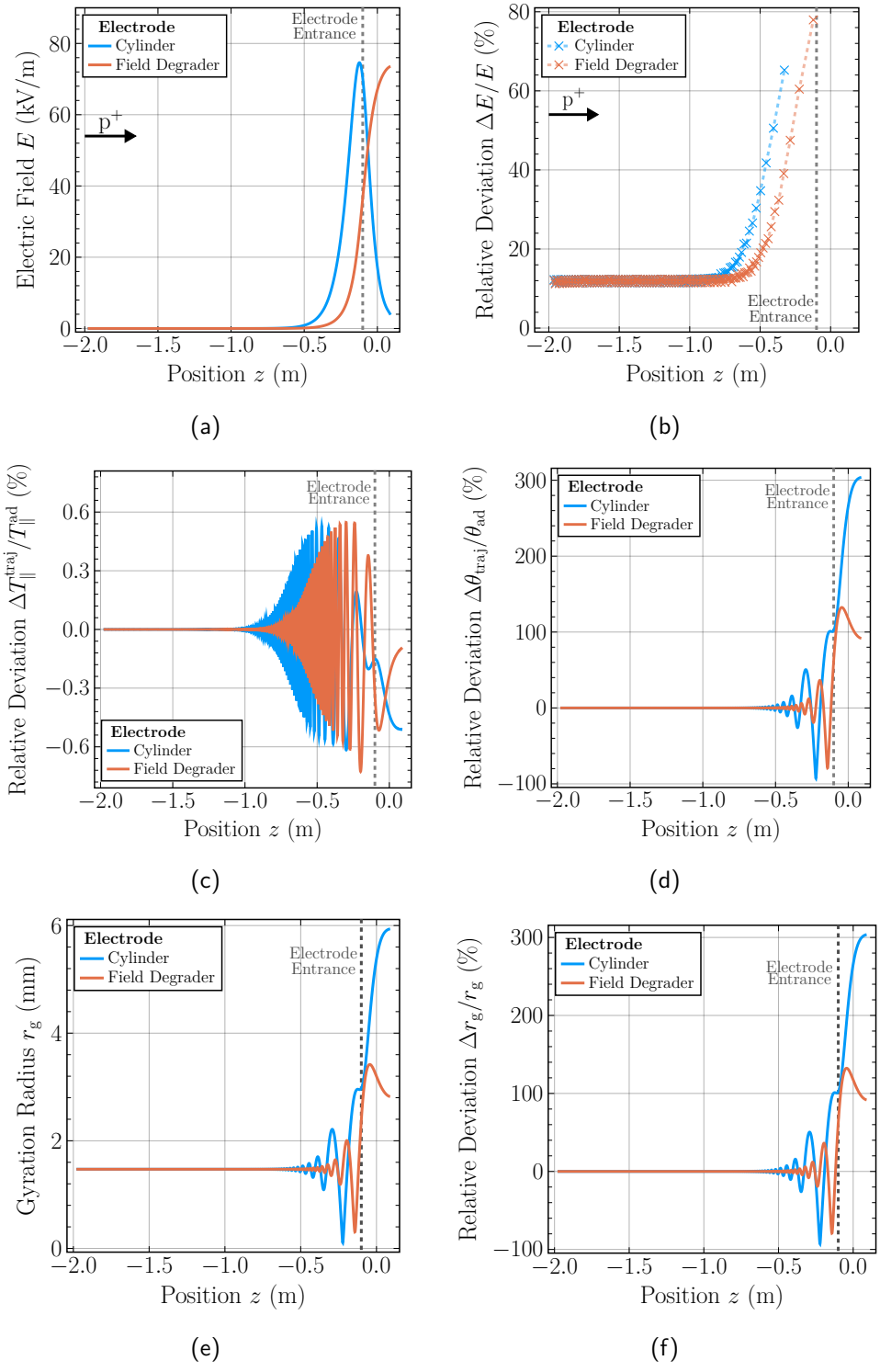


Figure 5.18: Comparison of non-adiabatic effects introduced by the cylinder electrode and field degrader: A proton of initial kinetic energy $T_0 = 10\,\mathrm{eV}$, pitch angle $\theta_0 = 45°$ and phase angle $\varphi_0 = 0°$ experiences a rapidly increasing electric field E (a) as it approaches the electrode in both setups. In this region, relative deviations $\Delta E/E$ of the electric field (b), evaluated after each period of the particle gyration, are significant. This causes non-adiabatic effects, which are reflected in deviations of the particle longitudinal kinetic energy $\Delta T_{\parallel}^{\mathrm{traj}}/T_{\parallel}^{\mathrm{ad}}$ (c) and pitch angle $\Delta\theta_{\mathrm{traj}}/\theta_{\mathrm{ad}}$ (d) from the adiabatic quantities $T_{\parallel}^{\mathrm{ad}}$ and θ_{ad} given in Eqs. (2.17) and (2.18), respectively. While oscillations of the particle kinetic energy are small, those observed in the particle pitch angle are significant. Since changes of the pitch angle are non-adiabatic, the particle gyration radius r_{g} (e) is no longer constant and large deviations $\Delta r_{\mathrm{g}}/r_{\mathrm{g}}$ from the initial gyration radius (f) are observed. Effects are, however, smaller when the proton is accelerated by the field degrader.

The relative field deviation $\Delta E/E$ within one gyration of the same proton, when accelerated by the cylinder electrode and field degrader, is shown in Fig. 5.18b. Here, $\Delta E/E$ is evaluated after every complete gyration of the particle, as described in Section 3.2.1. In the regions far from the electrode, where the electric field is close to zero, relative field deviations $\Delta E/E$ are (already) large in both setups[7]. As the particle approaches the electrode and gains longitudinal kinetic energy, the pitch height of the particle gyration increases. This is reflected by the decreasing number of periodic points with increasing position z considered in the evaluation of $\Delta E/E$. Over this region, $\Delta E/E$ increases significantly during one particle gyration. Since the electric field generated by the field degrader does not reach as far into the detection region, deviations $\Delta E/E$ start at a later position z of the particle trajectory and are smaller, compared to the cylinder electrode. Note that the pitch height of the gyro motion increases significantly before the proton enters the electrode and the proton does not complete a gyration afterwards. Large variations of the electric field during one gyration of the proton cause non-adiabatic effects in both setups.

Non-adiabatic effects are reflected in deviations of the proton longitudinal kinetic energy $T_{\parallel}^{\mathrm{traj}}$ and pitch angle θ_{traj} from the adiabatic quantities $T_{\parallel}^{\mathrm{ad}}$ and θ_{ad} given in Eqs. (2.17) and (2.18). Figs. 5.18c and 5.18d show relative deviations $\Delta T_{\parallel}^{\mathrm{traj}}/T_{\parallel}^{\mathrm{ad}}$ and $\Delta\theta_{\mathrm{traj}}/\theta_{\mathrm{ad}}$ of the proton kinetic energy and pitch angle, respectively, along the particle trajectory. Oscillations of both quantities in regions where the proton experiences strong electric field gradients are observed in the two setups. Effects in the longitudinal kinetic energy of the proton are small. However, $\Delta\theta_{\mathrm{traj}}/\theta_{\mathrm{ad}}$ oscillates with a significant amplitude. In the field degrader setup, oscillations of the pitch angle have a smaller envelope, compared to the cylinder electrode, caused by the smaller field gradients experienced by the proton.

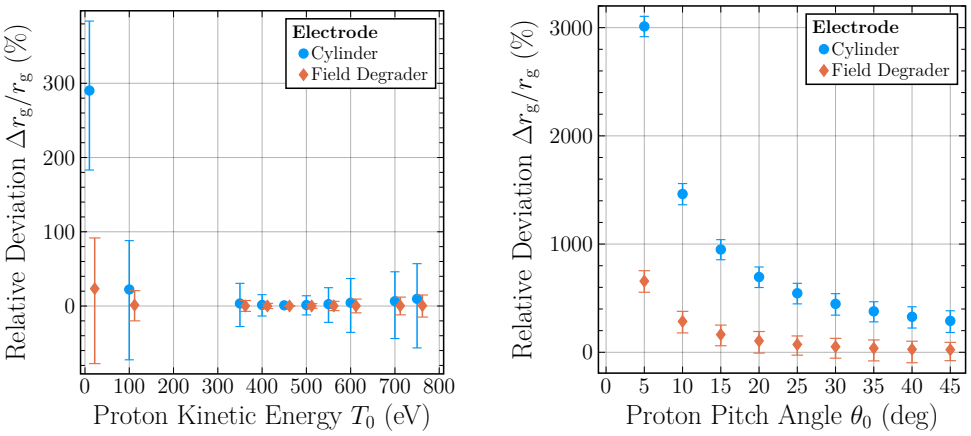
One property of the particle trajectory, which comprises both non-adiabatic effects, is the particle gyration radius r_{g}. Fig. 5.18e shows that the gyration radius is no longer constant. Relative deviations of the gyration radius $\Delta r_{\mathrm{g}}/r_{\mathrm{g}}$ from the initial gyration radius r_{g} become significant as the proton approaches the electrode entrance in both setups, as shown in Fig. 5.18f. Note that oscillations of $\Delta r_{\mathrm{g}}/r_{\mathrm{g}}$ are comparable to those observed in the particle pitch angle. Independent on the electrode type, deviations of the gyration radius remain significant at the end of the particle trajectory.

Fig. 5.19 shows the relative deviation $\Delta r_{\mathrm{g}}/r_{\mathrm{g}}$ of the particle gyration radius evaluated at the end of the particle trajectory as a function of the initial proton kinetic energy T_0 ($\theta_0 = 45°$) and pitch angle θ_0 ($T_0 = 10\,\mathrm{eV}$). Here, the correlation between the particle kinetic energy and the radial starting position of a tracked proton is considered according to Fig. 5.1. The relative deviation $\Delta r_{\mathrm{g}}/r_{\mathrm{g}}$ represents the mean value evaluated over the phase angle φ_0, ranging from 0° to 360° in steps of 45°. Variation bars indicate the minimum and maximum deviation from the mean value $\Delta r_{\mathrm{g}}/r_{\mathrm{g}}$. It can be seen that non-adiabatic effects are smaller in the field degrader setup for all proton energies and pitch angles. Since the electric field generated by the field degrader is more homogeneous, variations from the mean value are significantly smaller. Results show that relative deviations $\Delta r_{\mathrm{g}}/r_{\mathrm{g}}$ strongly depend on the initial properties of the incoming protons:

- Low energetic protons with pitch angles θ_0 up to 15° follow orbits of small gyration radii ($r_{\mathrm{g}} < 0.5\,\mathrm{mm}$) at the start of the trajectory. Additionally, they cover regions of strongly non-uniform electric fields at large distances from the axis of symmetry z. Hence, relative deviations $\Delta r_{\mathrm{g}}/r_{\mathrm{g}}$ and phase angle variations are largest for such protons in both setups.

- Protons with energies below 450 eV, which enter the detection region at smaller distances from the symmetry axis, cover more homogeneous electric field areas (see Fig. 5.17). Thus,

[7] The electric field generated by the two electrodes in regions far from the electrode increases very slowly and is in the order of $10^{-6}\,\mathrm{V/m}$. Thus, relative changes of the electric field $\Delta E/E$ during one particle gyration are already large, however, constant.



(a) $\theta_0 = 45\,\text{eV}$ (b) $T_0 = 10\,\text{eV}$

Figure 5.19: Relative deviation $\Delta r_g/r_g$ of the particle gyration radius, evaluated at the end of the particle trajectory, as a function of the initial proton (a) kinetic energy T_0 and (b) pitch angle θ_0 for the cylinder electrode and field degrader. Here, $\Delta r_g/r_g$ is the mean value over all tracked phase angles φ_0 for a given proton energy. Variation bars indicate the minimum and maximum deviation from the mean value. Note that for a better comparison of the variations bars, data for the field degrader is shifted by 10 eV in (a). A comparison of the two electrodes shows that non-adiabatic effects are significantly smaller in the field degrader setup, independent on the particle energy and pitch angle.

$\Delta r_g/r_g$ and φ_0-variations decrease with increasing kinetic energy T_0 in this range.

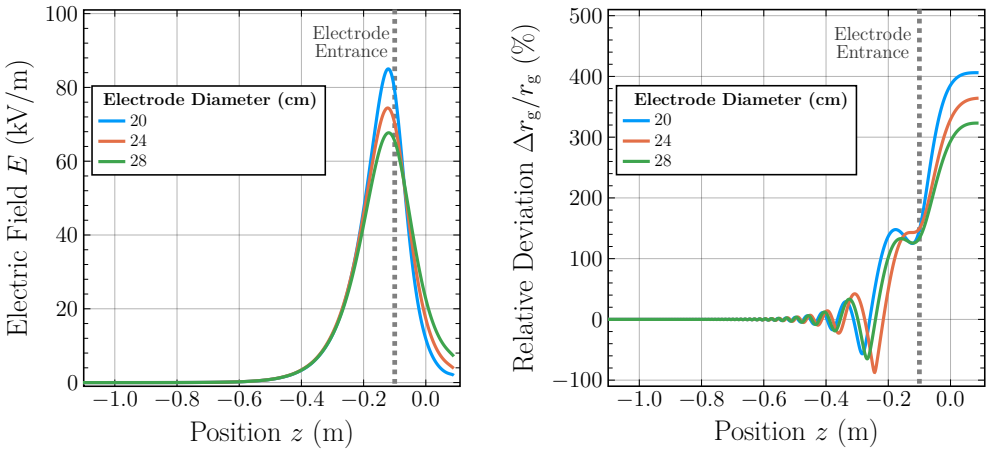
- The transport of protons with energies of 450 eV, which start the trajectory on the axis of symmetry, is adiabatic in both setups and φ_0-variations vanish.
- For energies above 450 eV, relative deviations of the gyration radius increase with T_0. Since the gyration radius of the particle orbit increases with the transversal particle velocity $v_\perp$ (see Eq. (2.5)) and, thus, with the transversal kinetic energy $T_\perp$, high energetic particles cover wider areas of the detection region and experience larger field gradients. Therefore, phase angle variation increase with the kinetic energy T_0.

Both electrodes require geometrical and electrical adjustments to reduce gradients of the electric field experienced by the decay protons within one gyration period and to minimize non-adiabatic effects. Such adjustments are discussed in the following for the cylinder electrode and field degrader, individually.

5.4.1 Adjustments to the Cylinder Electrode

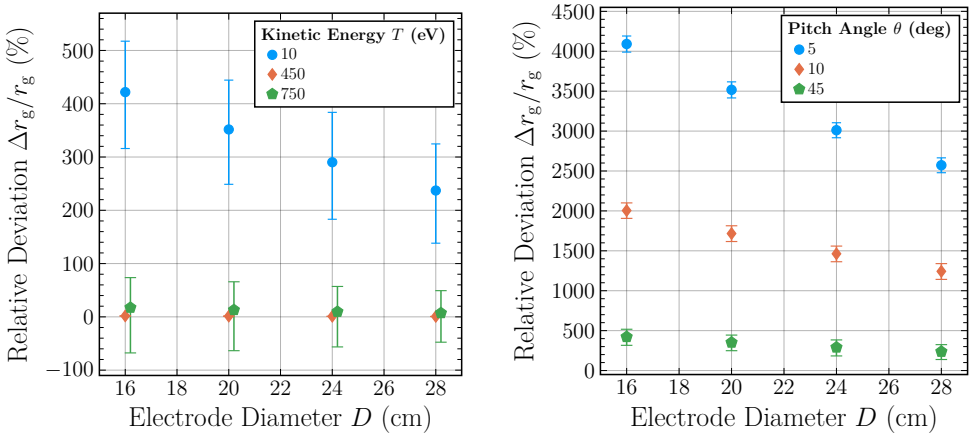
Electrode Diameter and Length

Two trivial geometrical electrode parameters, which affect the electric field and its magnitude, are the electrode diameter D and length L. Fig. 5.20a shows the electric field along the trajectory of a proton of energy $T_0 = 10\,\text{eV}$, pitch angle $\theta_0 = 45°$ and phase angle $\varphi_0 = 315°$ for multiple diameters D of the cylinder electrode. It can be seen that the peak of the electric field at the electrode entrance decreases for larger diameters, while its reach towards the detector increases. The effect of the diameter variation on relative deviations $\Delta r_g/r_g$ of the gyration radius is shown in Fig. 5.20b for the same proton as a function of position z. The electric field strength at larger distances from the electrode entrance does not increase monotonically with the diameter D. It



(a) (b)

Figure 5.20: (a) Electric field E and (b) relative deviation $\Delta r_g/r_g$ of the particle gyration radius as a function of position z for a proton of initial energy $T_0 = 10\,\text{eV}$ and pitch angle $\theta_0 = 45°$ for multiple electrode diameters D. The proton moves in the direction of increasing position z. The electrode entrance is marked by the gray dashed line. The peak at the electrode entrance decreases for larger electrode diameters while the reach of E towards the sensor increases. This results in a decrease of $\Delta r_g/r_g$ inside the electrode.



(a) $\theta_0 = 45\,\text{eV}$ (b) $T_0 = 10\,\text{eV}$

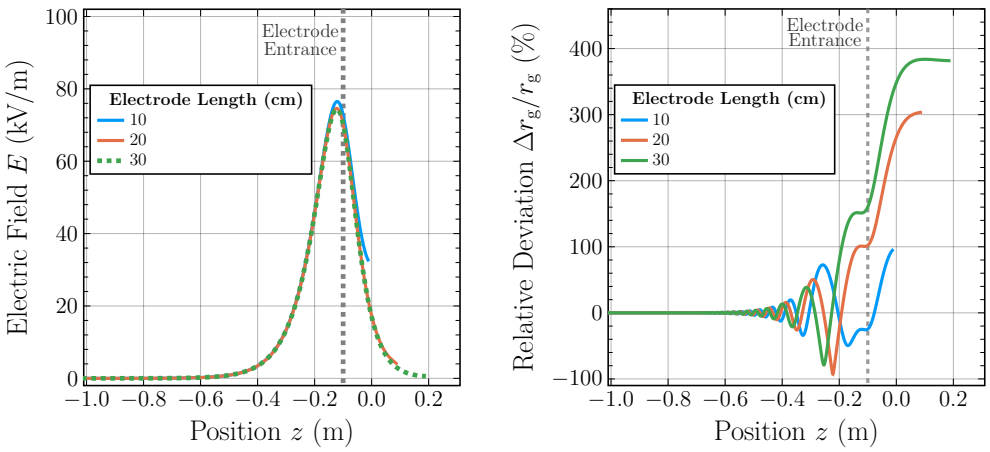
Figure 5.21: Relative deviation $\Delta r_g/r_g$ of the particle gyration radius, evaluated at the end of the particle trajectory, as a function of the proton initial (a) kinetic energy T_0 and (b) pitch angle θ_0 for multiple diameters D of the cylinder electrode. Note that for a better comparison of the variations bars, data for protons of kinetic energy 750 eV are shifted by 0.2 cm in (a). Relative deviations $\Delta r_g/r_g$ decrease with increasing electrode diameter for all proton energies and pitch angles. Effects are more pronounced for low energetic protons with small initial pitch angles.

reaches a maximum between diameters D of 24 cm and 26 cm[8], similar to the effect observed in the evaluation of the electrostatic potential at large distances from the electrode in Fig. 5.7a. For an electrode of diameter 24 cm, oscillations of the gyration radius occur at an earlier position of the particle trajectory and their amplitude increases in regions outside the electrode, compared to an electrode of diameter $D = 20\,\text{cm}$. An increase of the electrode diameter D from 24 cm to

[8]Evaluations of the electric field strength E at position $z = -0.4\,\text{m}$ yield 3343 V/m, 3470 V/m and 3367 V/m for an electrode diameter D of 20 cm, 24 cm and 28 cm, respectively.

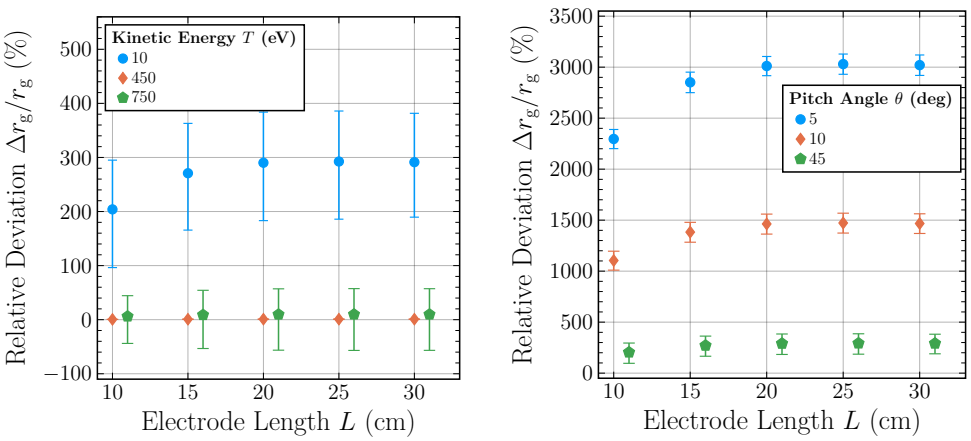
28 cm results in a decrease of the oscillation amplitude of $\Delta r_g/r_g$ in regions outside the electrode. Relative deviations of the gyration radius decrease with increasing electrode diameter inside the electrode. Fig. 5.21 shows the relative deviation of the gyration radius $\Delta r_g/r_g$ at the end of the particle trajectory as a function of the electrode diameter D for multiple proton initial energies T_0 and pitch angles θ_0. An increase of the electrode diameter from 24 cm to 28 cm results in a decrease of $\Delta r_g/r_g$ and of phase angle variations for all proton energies and pitch angles θ_0. However, non-adiabatic effects remain significant, especially when compared to the field degrader (see Fig. 5.19).

The influence of the electrode length L on the electric field E experienced by a proton of initial energy 10 eV and pitch angle 45° as it gyrates towards the sensor is shown in Fig. 5.22a. It can be seen that large electric fields are present over the entire length of the electrode and in front of the electrode entrance for $L = 10$ cm. Hence, the relative change of the electric field from the electrode entrance to the sensor is smaller. The relative deviation $\Delta r_g/r_g$ along the trajectory of the same proton is shown in Fig. 5.22b for multiple electrode lengths L. Although, oscillations of $\Delta r_g/r_g$ increase for shorter electrodes outside the electrode, relative deviations of the gyration radius are significantly smaller inside the electrode. A reduction of the electrode length from 20 cm to 10 cm results in smaller relative deviations of the gyration radius at the end of the trajectory for all proton energies T_0 and pitch angles θ_0. This is shown in Fig. 5.23. Note that $\Delta r_g/r_g$ reaches a constant value for electrode lengths above 20 cm. If the electrode is long enough, protons pass a region of constant electric field before arriving at the detector and non-adiabatic effect are suppressed over this region. Although non-adiabatic effects can be reduced by adjusting the electrode length and diameter, they remain significant.



(a) (b)

Figure 5.22: (a) Electric field E experienced by a proton of initial energy $T_0 = 10$ eV, pitch angle $\theta_0 = 45°$ and phase angle $\varphi_0 = 0°$ when accelerated by the cylinder electrode for multiple electrode lengths L. The peak at the electrode entrance decreases for larger electrode diameters. The field inside the electrode decreases slower when a a larger electrode diameter is considered. (b) Relative deviation $\Delta r_g/r_g$ of the particle gyration radius evaluated for the same proton as in (a) for multiple lengths L of the cylinder electrode. Relative deviations $\Delta r_g/r_g$ decrease inside the electrode with increasing length L. For a better comparison, data are shifted by -0.1 m and 0.1 m for the electrodes of length 10 cm and 30 cm, respectively, in both figures.

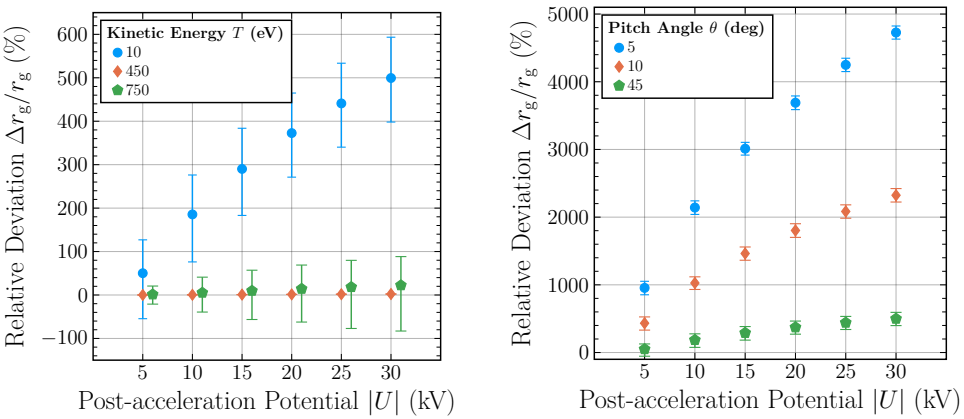


(a) $\theta = 45°$ (b) $T_0 = 10\,\text{eV}$

Figure 5.23: Relative deviation $\Delta r_g/r_g$ of the particle gyration radius, evaluated at the end of the particle trajectory, as a function of the proton initial (a) kinetic energy T_0 and (b) pitch angle θ_0 for multiple lengths L of the cylinder electrode. Note that data are shifted by 1 cm for protons of energies 750 eV in (a) and by 1° for $\theta_0 = 45°$ in (b). Although non-adiabatic effects observed for low energetic protons can be reduced if an electrode of length 10 cm is chosen, effects remain significant.

Proton Post-acceleration Potential

In order to significantly reduce the magnitude of the electric field, a smaller post-acceleration potential U_A can be chosen. The peak of the electric field E present at the electrode entrance decreases linearly with the post-acceleration potential (see Fig. D.2) and particles experience smaller field gradients over the tracked distance. A significant reduction of relative deviations $\Delta r_g/r_g$ of the particle gyration radius is achieved for all initial proton energies T_0 and pitch angles θ_0 when a post-acceleration potential $|U_A|$ of 5 kV is chosen, as shown in Fig. 5.24. Additionally, variation



(a) $\theta = 45°$ (b) $T_0 = 10\,\text{eV}$

Figure 5.24: Relative deviation $\Delta r_g/r_g$ of the particle gyration radius, evaluated at the end of the proton trajectory, as a function of the initial proton (a) kinetic energy T_0 and (b) pitch angle θ_0 for multiple post-acceleration potentials $|U_A|$ applied at the cylinder electrode. Note that data are shifted by 1 kV for protons of energies 750 eV in (a). Non-adiabatic effects can be significantly reduced if a low post-acceleration potential is chosen.

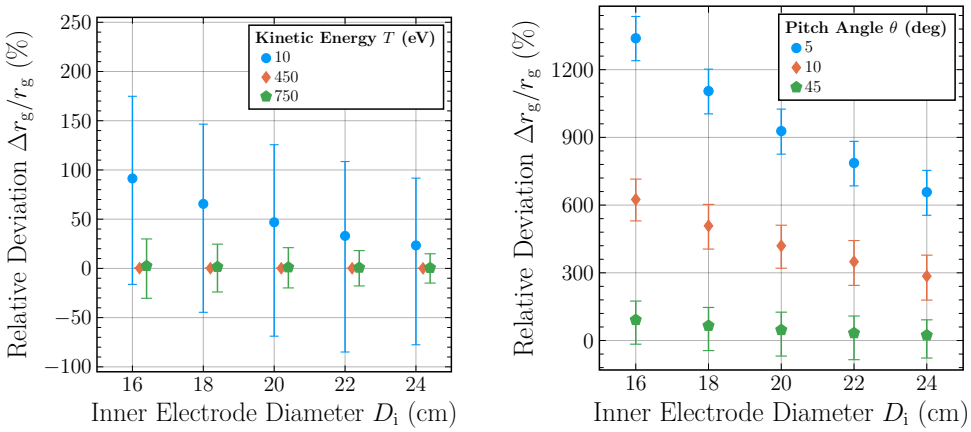
bars decrease significantly for high energetic protons. Results obtained for a post-acceleration potential of 5 kV are comparable to the ones obtained for the field degrader (see Fig. 5.19). The

amount of post-acceleration required for the detection of decay protons depends, among other parameters, on the chosen detector type and on the detector performance.

5.4.2 Adjustments to the Field Degrader

Electrode Diameter and Length

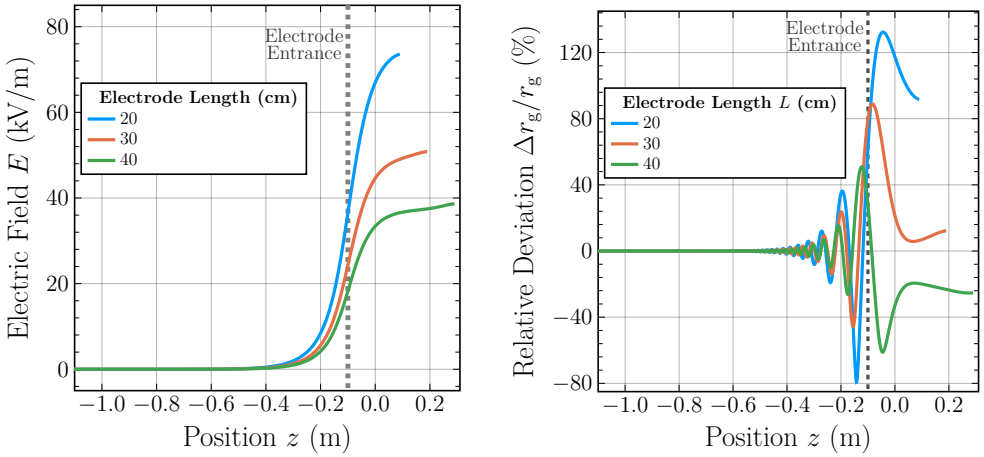
Similar to the adjustment of the cylinder electrode diameter, an increase of the field degrader inner diameter can be considered to reduce the electric field strength and, therefore, non-adiabatic effects, especially for low energetic protons. Fig. 5.25 shows the relation between the relative gyration radius $\Delta r_\mathrm{g}/r_\mathrm{g}$ and the electrode inner diameter D_i for multiple proton energies T_0 and pitch angles θ_0. The field degrader length L and outer diameter D_o are fixed to 20 cm and 28 cm, respectively. Although relative deviations $\Delta r_\mathrm{g}/r_\mathrm{g}$ decrease for all proton kinetic energies and pitch angles if the electrode diameter is increased, non-adiabatic effects remain significant, especially for low energetic protons. Additional electrode parameters require adjustments to minimize such effects.



(a) $\theta = 45°$ (b) $T_0 = 10\,\mathrm{eV}$

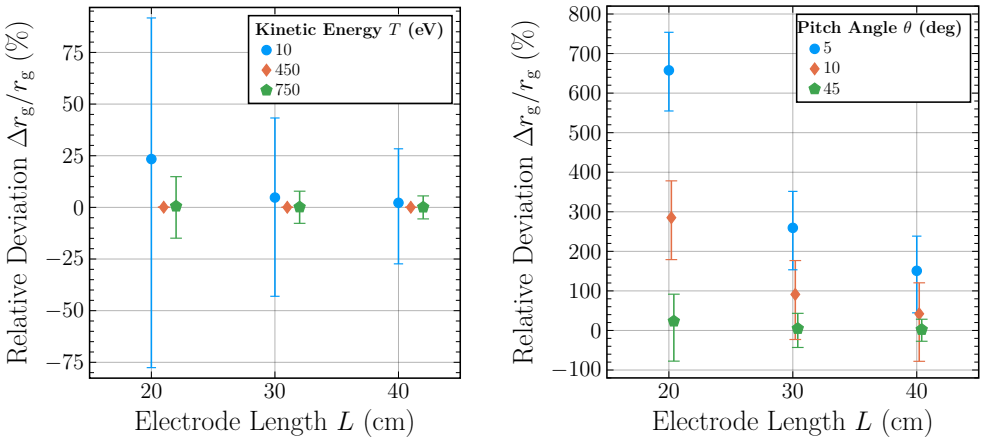
Figure 5.25: Relative deviation $\Delta r_\mathrm{g}/r_\mathrm{g}$ of the particle gyration radius, evaluated at the end of the proton trajectory, as a function of the initial proton (a) kinetic energy T_0 and (b) pitch angle θ_0 for multiple inner diameters D_i of the field degrader. Note that data are shifted by 0.2 cm and 0.4 cm for protons of energies 450 eV and 750 eV, respectively, in (a). A large inner electrode diameter is required to minimize non-adiabatic effects, especially for low energetic protons with small initial pitch angles.

Electric field experienced by the protons as they gyrate towards the detector can be significantly reduced by adjusting the number of individual rings (and, thus, the electrode length) and the surface potential applied at the rings. In the following, a field degrader of length $L = 20$ cm, 30 cm and 40 cm composed of 11, 16 and 21 equidistant rings with an increment of the surface potential of -1.5 kV, -1 kV and -0.75 kV between subsequent electrode rings, respectively, is considered. The three field degrader setups are described in see Table C.1 (labeled as setup 1 to 3). The increment of the surface potential is adapted to the number of electrode rings according to $U_\mathrm{A}/(N-1)$, where U_A denotes the post-acceleration potential and N is the total number of rings. All other electrode parameters remain unchanged. The electric field experienced by a proton with initial energy $T_0 = 10$ eV, pitch angle $\theta_0 = 45°$ and phase angle $\varphi_0 = 0°$ is shown in Fig. 5.26a for the three field degrader setups of length L. For a better comparison, data shown in this figure are shifted such that the positions of the electrode entrance coincide in all setups. Results show that the electric field decreases in magnitude if a long field degrader, with a small



(a) (b)

Figure 5.26: (a) Electric Field E as a function of position z for multiple length L of the field degrader for a proton of initial kinetic energy $T_0 = 10\,\text{eV}$, pitch angle $\theta_0 = 45°$ and phase angle $\varphi_0 = 45°$. The surface potential applied at the electrode rings is adjusted to the number of electrode plates such that the potential gradient remains linear. This results in an overall smaller electric field strength for longer electrodes. (b) Relative deviation $\Delta r_g/r_g$ of the particle gyration radius as a function of position z for the same proton as in (a) and multiple electrode lengths L of the field degrader. It can be seen that oscillations of $\Delta r_g/r_g$ decreases when a long electrode is considered. Note that for a better comparison data in both (a) and (b) are shifted by 0.1 m and 0.2 m for the electrodes of length 30 cm and 40 cm, respectively



(a) $\theta = 45°$ (b) $T_0 = 10\,\text{eV}$

Figure 5.27: Relative deviation $\Delta r_g/r_g$ of the particle gyration radius, evaluated at the end of the particle trajectory, as a function of the initial proton (a) kinetic energy T_0 and (b) pitch angle θ_0 for multiple lengths L of the field degrader. Note that data are shifted by 1 cm and 2 cm for protons of energies 450 eV and 750 eV, respectively, in (a). In (b), data are shifted by 0.2 cm and 0.4 cm for $\theta_0 = 10°$ and 45°, respectively. Non-adiabatic effects can be significantly reduces if the length of the field degrader is increased.

increment of the surface potential applied at the electrode rings, is considered. This effect leads to a reduction of the oscillation amplitude of the relative gyration radius $\Delta r_g/r_g$, as can be seen in Fig. 5.26b. The mean value $\Delta r_g/r_g$ evaluated at the end of the particle trajectory and variations with the phase angle decrease with increasing electrode length for all proton energies T_0 and pitch

angles θ_0. This is shown in Fig. 5.27. Note that the dependence of $\Delta r_\mathrm{g}/r_\mathrm{g}$ on the particle initial energy T_0 and pitch angle θ_0 also becomes smaller for longer electrodes. Although significant improvements are obtained for the field degrader of length $L = 40\,\mathrm{cm}$ in combination with a small increment of the surface potential applied at the electrode rings (setup 1), non-adiabatic effects remain significant for low energetic protons of small pitch angles θ_0.

One optional feature of the field degrader is the concentric wire grid, that can be mounted at the electrode entrance ring. In the following, the adiabatic transport of protons which are accelerated by such an electrode is studied.

Wire Grid Field Degrader

Results presented in Sections 5.3.2 and 5.3.4 have shown that the wire grid used in combination with the field degrader shields the detection region from the electrostatic potential generated by the electrode more effectively and improves the potential homogeneity inside the electrode. In the following, the electric field and relative changes of the particle gyration radius are studied for the wire grid field degrader in the standard configuration (see setup 1 in Table C.2). The orientation of the electric field E generated by the electrode is shown in Fig. D.6 in the y-z-plane for $x = 0\,\mathrm{m}$. The electric field strength E and deviations of the particle gyration radius $\Delta r_\mathrm{g}/r_\mathrm{g}$ experienced by a proton of energy $T_0 = 10\,\mathrm{eV}$ and pitch angle $\theta_0 = 45°$ when accelerated by the wire grid field degrader is shown in Fig. 5.28.

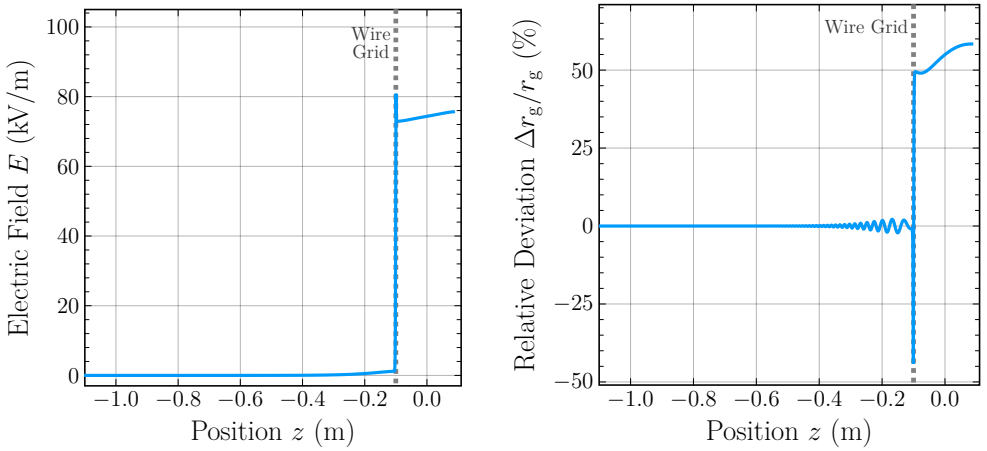
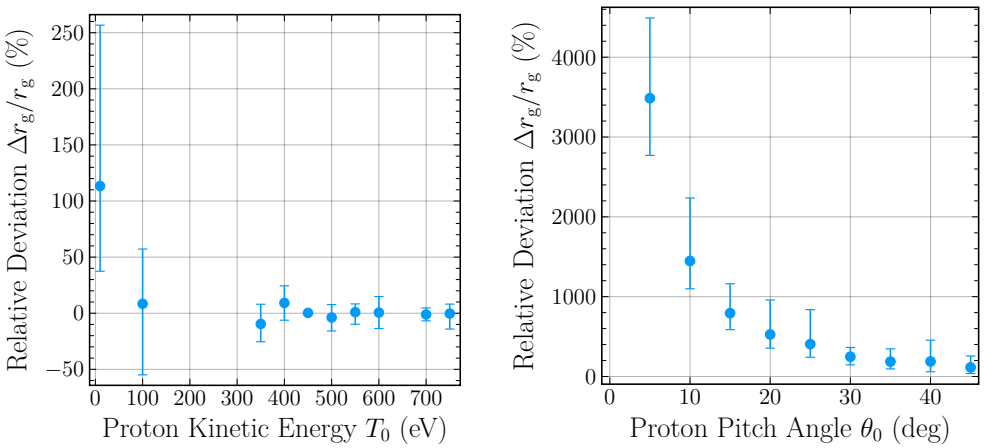


Figure 5.28: (a) Electric field E and (b) relative deviation $\Delta r_\mathrm{g}/r_\mathrm{g}$ of the particle gyration radius as a function of position z for a proton of initial kinetic energy $T_0 = 10\,\mathrm{eV}$, pitch angle $\theta_0 = 45°$ and phase angle $\varphi_0 = 0°$ when accelerated by the field degrader in combination with the concentric wire grid. The wire grid shields the detection region from strong electric fields and oscillations of $\Delta r_\mathrm{g}/r_\mathrm{g}$ are small in this region. Strong electric fields present in the wire plane cause an abrupt change of the particle gyration radius.

As the proton approaches the electrode entrance it experiences a slowly increasing electric field and oscillations observed in the gyration radius are small. However, large fields are present in the wire plane and cause strong relative deviations $\Delta r_\mathrm{g}/r_\mathrm{g}$ of the particle gyration radius. Inside the electrode, E increases monotonically as the proton moves towards the detector. Relative deviations of the gyration radius $\Delta r_\mathrm{g}/r_\mathrm{g}$, evaluated at the end of the particle trajectory, are shown in Fig. 5.29 as a function of the proton initial kinetic energy T_0 and pitch angle θ_0. Non-adiabatic effects increase for all particle energies and pitch angles, when compared to the field degrader without the wire grid (see Fig. 5.19). Variation bars also increase significantly, especially for low energetic protons. These variations arise as protons of the same energy and pitch angle but with



(a) $\theta_0 = 45°$ (b) $T_0 = 10\,\text{eV}$

Figure 5.29: Relative deviation $\Delta r_g/r_g$ of the particle gyration radius, evaluated at the end of the particle trajectory, as a function of the initial proton (a) kinetic energy T_0 and (b) pitch angle θ_0. Significant field gradients present in the wire plane (see Fig. 5.28) induce larger non-adiabatic effects, especially for low energetic protons, compared to the field degrader without a wire grid (see Fig. 5.19).

different initial phase angle φ_0 traverse the wire plane at different radial distances from the wires, where strong electric fields are present.

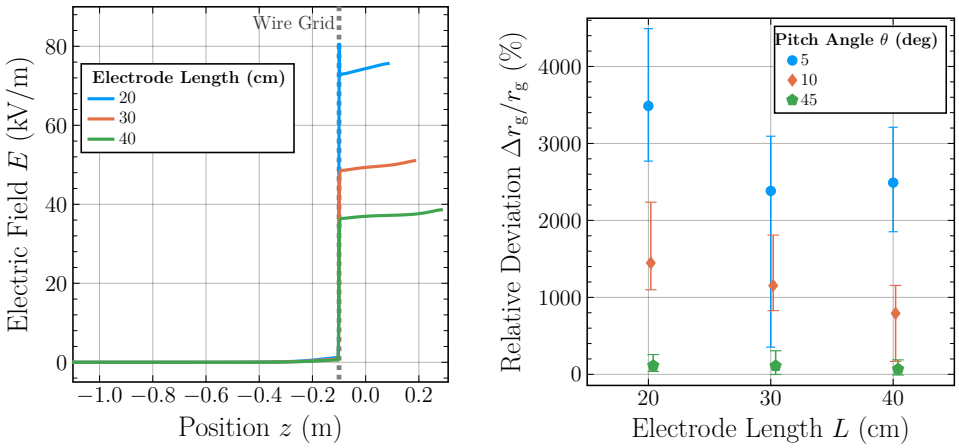
If such an electrode is considered for the proton post-acceleration, multiple electrode parameters require adjustments to avoid strong electric fields at the wire grid and to minimize non-adiabatic effects. The influence of such adjustments on relative changes of the particle gyrations are studied in the following.

Strong electric fields experienced by the protons in the wire plane can be reduced if the difference between the surface potentials applied at the wire grid and the subsequent electrode ring is small. Two approaches to achieve this are considered in the following: an increase of the field degrader length by addition of electrode rings and a field degrader with a double wire grid system.

Length Variation of the Wire Grid Field Degrader

First, a variation of the number of electrode rings and of the surface potential applied at the individual rings is considered. The electrode of length $L = 20\,\text{cm}$, 30 cm and 40 cm (labeled as setup 1 to 3) is composed of 11, 16 and 21 equidistant rings with an increment of the surface potential of $-1.5\,\text{kV}$, $-1\,\text{kV}$ and $-0.75\,\text{kV}$ between subsequent rings, respectively (see Table C.2). All other electrode parameters remain unchanged. The electric field E experienced by the particle in the wire plane and inside the electrode decreases for longer electrodes with a smaller increment of the surface potential applied at the rings (see Fig. 5.30a). The relative deviation $\Delta r_g/r_g$ of the particle gyration radius, evaluated at the end of the trajectory, is shown in Fig. 5.30b for multiple proton kinetic energies T_0 and pitch angles θ_0 as a function of the electrode length L. The mean value $\Delta r_g/r_g$ and phase angle variations decrease for longer electrodes, for which a smaller increment of the surface potential is chosen between subsequent electrode rings. However, non-adiabatic effects remain significant, especially for low energetic protons, when compared to the field degrader with the same geometrical and electrical setup without the wire grid (see Fig. 5.27).

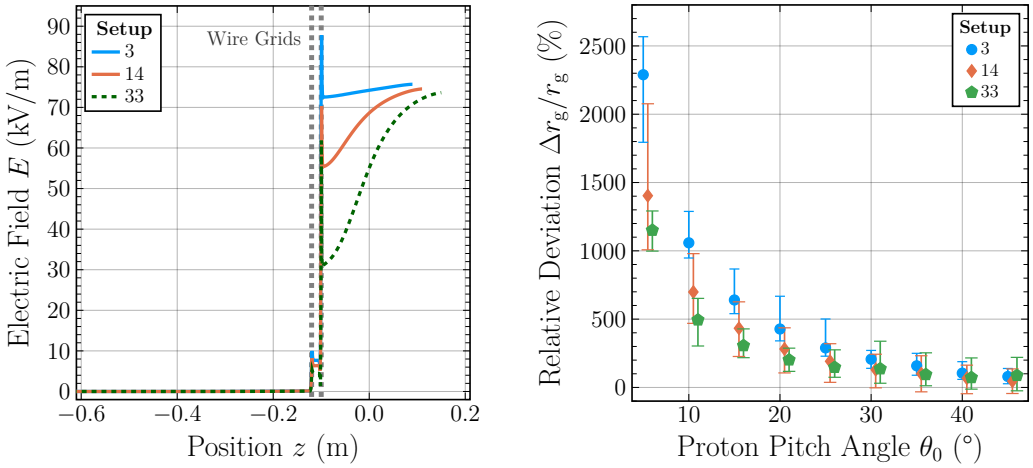
Double Wire Grid System



(a) (b)

Figure 5.30: (a) Electric field E as a function of position z experienced by a proton of initial kinetic energy $T_0 = 10\,\text{eV}$, pitch angle $\theta_0 = 45°$ and phase angle $\varphi_0 = 0°$ accelerated by a wire grid field degrader of various lengths L. (b) Relative deviation $\Delta r_g/r_g$ of the particle gyration radius, evaluated at the end of the particle trajectory, as a function of the electrode length L (corresponding to setups 1 to 3 in Table C.2) for multiple initial kinetic energies T_0 and pitch angles θ_0 of the decay protons. The field degrader has a concentric wire grid attached at the electrode entrance. For a better comparison, data in (a) are shifted by 0.1 m and 0.2 m for the field degrader of length $L = 30\,\text{cm}$ and 40 cm, respectively. Data are shifted by 0.2 cm and 0.4 cm for initial pitch angles θ_0 of 10° and 45° in (b).

Another approach to reduce strong electric fields present in the wire plane is to use a double wire grid system. The two wire grids can be attached to the electrode entrance (wire grid 1) and to the subsequent ring (wire grid 2). The latter should be operated at a small surface potential to shield the wire grid at the electrode entrance from large electrostatic potentials and, thus, electric fields. To avoid large electric fields at the second wire grid, additional adjustments of the number of electrode rings and of their surface potential is required. Simulations were performed for multiple setups of the field degrader with a double wire grid system and inclusions of additional electrode rings. A list of the simulated setups is provided in Tables C.3 to C.5. The setups are divided into three groups based on the number of additional electrode rings considered. The surface potential applied at the electrode rings R1 to R10 increases from $-15\,\text{kV}$ to $-1.5\,\text{kV}$ in steps of 1.5 kV in all setups, while surface potentials applied at the remaining electrode rings are varied. To show trends, non-adiabatic effects are studied for comparable setups (number 3, 14 and 33), one from each setup subgroup. Fig. 5.31a shows the electric field E evaluated along the trajectory of a proton with kinetic energy $T_0 = 10\,\text{eV}$, pitch angle $\theta_0 = 45°$ and phase angle $\varphi_0 = 0°$ for the three setups. Note that for a better comparison, data are shifted in the various setups to match the positions of the electrode entrance. The protons experience significant electric fields, especially at the second wire grid. The peaks of the electric field present at the two wires grids can be reduced if multiple rings are added to the field degrader (one and three additional rings in setup 14 and 33, respectively), which are operated at small surface potentials. The best results are achieved for setup 33. The relative deviation of the particle gyration radius $\Delta r_g/r_g$ evaluated at the end of the trajectory is shown in Fig. 5.31b as a function of the pitch angle θ_0 for a proton of initial kinetic energy $T_0 = 10\,\text{eV}$. Relative changes of the gyration radius and phase angle variations decrease considerably for small proton pitch angles in electrode setup 33. However, non-adiabatic effects remain significant when compared to the field degrader in the standard configuration.



(a) (b)

Figure 5.31: (a) Electric field E as a function of position z for a proton of initial kinetic energy $T_0 = 10\,\text{eV}$, pitch angle $\theta_0 = 45°$ and phase angle $\varphi_0 = 0°$ accelerated by the field degrader in combination with the double wire grid and additional electrode rings (setups listed in Tables C.3 to C.5). (b) Relative deviation $\Delta r_g/r_g$ of the particle gyration radius, evaluated at the end of the particle trajectory, as a function of the initial pitch angle θ_0 of a proton of kinetic energy $T_0 = 10\,\text{eV}$ and multiple setups of the field degrader. Strong electric fields present in the two wire planes and inside the electrode can be reduced if the increment of the electrostatic potential applied at the wire grids and the subsequent electrode rings is small. The best results are obtained for setup 33, especially for low energetic protons with small pitch angles. For a better comparison, data in (a) are shifted by 2 cm and 6 cm in setups 14 and 33, respectively, and by 0.5° and 1° for setups 14 and 33 in (b).

Results have shown that the particle transport is non-adiabatic if the protons are accelerated by the cylinder electrode and field degrader (standard configurations). Effects are, however, significantly smaller in the field degrader setup, where protons cover regions of more homogeneous electric fields and experience smaller field gradients as they gyrate towards the sensor. Although multiple electrode parameters can be adjusted to minimize non-adiabatic effects, further investigations are required to evaluate their influence on the E×B drift effect. Such studies are performed in the following section.

5.5 E×B Drift Effect Studies

Charged particles might experience E×B drifts when they pass regions of crossed electric and magnetic fields. The orientation of the electric field induced by the cylinder electrode and field degrader (standard configurations) inside the detection region was shown in Fig. 5.17. The normal electric field components E_x and E_y contribute to the E×B drift effect. Fig. 5.32 shows the normal field components evaluated in both electrode setups along the trajectory of a proton with initial kinetic energy $T_0 = 10\,\text{eV}$ and pitch angle $\theta_0 = 45°$ which starts 4 cm off-axis. It can be seen that the normal field component E_x is dominant in both setups. Since the proton enters the detection region off-axis, it passes a region of non-uniform electric field while moving towards the electrode entrance. Both E_x and E_y reach a minimum in the vicinity of the cylinder electrode and field degrader entrance. The normal fields experienced by the proton after it enters the electrode differ in the two setups:

- Cylinder electrode: The orientation of the electric field changes as the proton enters the

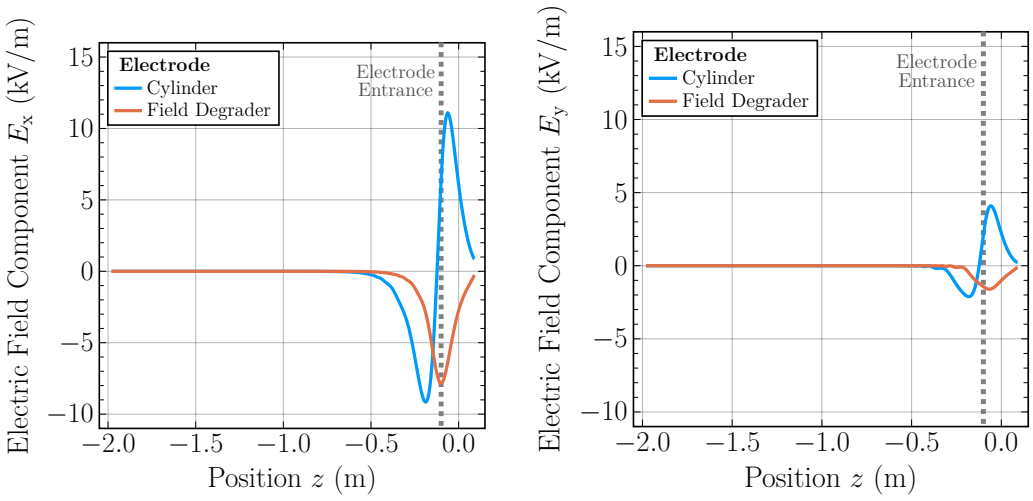


Figure 5.32: Normal electric field components (a) E_x and (b) E_y experienced by a proton of initial kinetic energy $T_0 = 10\,\text{eV}$, pitch angle $\theta_0 = 45°$ and phase angle $\varphi_0 = 0°$ which is accelerated by the cylinder electrode and field degrader. The proton experiences large normal electric fields before it enters the electrode, independent on the chosen electrode. Inside the electrode, both E_x and E_y decrease rapidly towards the proton sensor.

electrode (see Fig. 5.17a). This is reflected by the change in the sign of both normal electric field components. Inside the cylinder, E_x and E_y increase to a maximum close to the electrode entrance and, subsequently, decrease towards the proton sensor.

- Field degrader: Since the electric field inside the field degrader is oriented predominantly in direction z, both normal field components converge towards zero.

To quantify the E×B drifts experienced by the protons, the distance $D^{\text{gc}}_{\text{E×B}}$ by which the particle guiding center has drifted is evaluated at the end of the particle trajectory as described in Section 3.2.3.

Fig. 5.33 shows $D^{\text{gc}}_{\text{E×B}}$ as a function of the initial proton kinetic energy T_0 and pitch angle θ_0 for a fixed angle $\theta_0 = 45°$ and energy $T_0 = 10\,\text{eV}$, respectively, in both detection setups. Here, $D^{\text{gc}}_{\text{E×B}}$ is the mean value evaluated over all simulated phase angles φ_0 for a given proton energy and pitch angle[9]. Variation bars indicate the minimum and maximum deviation from the mean value $D^{\text{gc}}_{\text{E×B}}$. Results obtained for all simulated protons show a similar dependence on the particle kinetic energy and pitch angle. A comparison between the two electrode types shows:

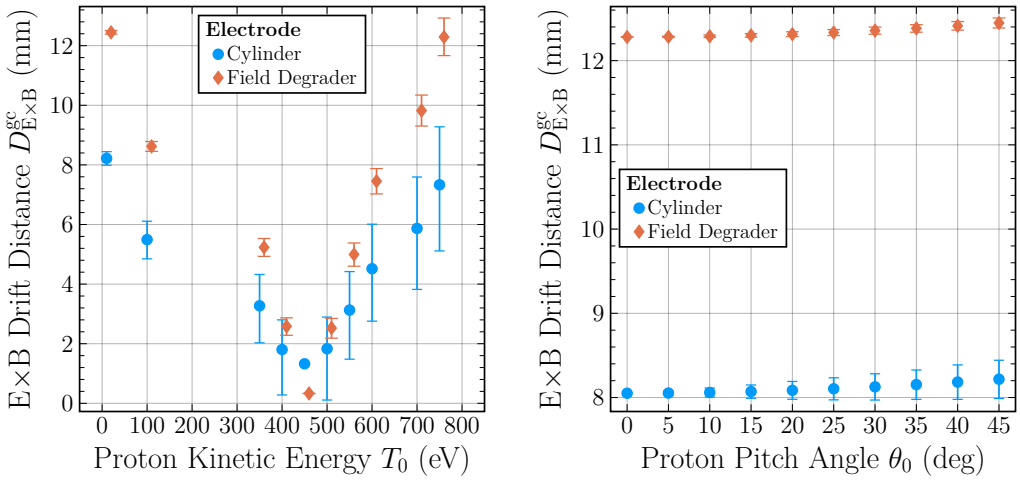
- The drift distance $D^{\text{gc}}_{\text{E×B}}$ is smaller for all proton energies (except for $T_0 = 450\,\text{eV}$) and pitch angles in the cylinder electrode setup. This is caused by the change in orientation of the electric field and, thus, of the E×B drift velocity $\boldsymbol{v}_{\mathbf{E\times B}}$ (see Eq. (2.11)) which results in a compensation of the net drift effect. Phase angle variations are, however, significantly larger since protons gyrate in a strongly non-uniform electric field.

- Protons of initial kinetic energy $T_0 = 450\,\text{eV}$, which enter the detection region on-axis, drift by a smaller amount if they are accelerated by the field degrader. The electric field generated by the field degrader in the regions covered by such protons is more homogeneous and has a lower strength, compared to the cylinder electrode. Since both geometries are axially symmetric, variation bars vanish.

[9]Simulated protons have initial phase angle φ_0 in the range 0° to 360° in steps of 45°.

- A strong dependence of $D^{\mathrm{gc}}_{\mathrm{E\times B}}$ is also observed for the particle kinetic energy T_0 in both setups. Normal electric field components are zero at the central axis z and their strength increases for larger distances from the axis. Hence, protons which enter the detection region off-axis experience larger drifts.

- Phase angle variations from the mean value $D^{\mathrm{gc}}_{\mathrm{E\times B}}$ increase with the particle energy and pitch angle in both setups. Protons of higher energies have larger gyration radii and cover a wider region of strong normal electric fields. The same effect causes an increase of phase angle variations with the particle pitch angle θ_0 for a fixed energy T_0.



(a) $\theta_0 = 45°$ (b) $T_0 = 10\,\mathrm{eV}$

Figure 5.33: Comparison of the drift distance $D^{\mathrm{gc}}_{\mathrm{E\times B}}$ of the particle guiding center, evaluated at the end of the particle trajectory, as a function of the initial proton (a) kinetic energy T_0 and (b) pitch angle θ_0 for the cylinder electrode and the field degrader. Here, $D^{\mathrm{gc}}_{\mathrm{E\times B}}$ is the mean value over all simulated phase angles φ_0 and variation bars indicate the minimum and maximum deviation from the mean value. Although drifts experienced by the protons are larger in the field degrader setup, variation bars are significantly smaller for all proton energies and pitch angles. Low and high energetic protons drift by large distances in both setups. Note that data for the field degrader are shifted in (a) by 10 eV for a better visualization.

E×B drifts experienced by the decay protons in the two setups are significant, especially for protons which enter the detection region at larger distances off-axis. To make a measurement of the decay protons feasible, adjustments of the electrode geometries are required. In the following, the influence of geometrical and electrical parameters of the two electrodes on E×B drifts experienced by the decay protons is studied.

5.5.1 Adjustments to the Cylinder Electrode

Electrode Diameter

The electric field generated by the cylinder electrode decreases in magnitude (as shown in Fig. 5.20a) and becomes more homogeneous across the regions covered by the proton beam if the electrode diameter is increased[10]. Fig. 5.34 shows the normal electric field components E_{x}

[10]Studies performed in Section 5.3.4 have shown that the homogeneity of the electrostatic potential at larger distance from the proton sensor increases if the electrode diameter is large. The opposite is observed in the vicinity of the sensor, however, effects are in the order of 1 % in the studied diameter range.

and E_y along the trajectory of a proton with initial kinetic energy $T_0 = 10\,\text{eV}$ and pitch angle $\theta_0 = 45°$ for multiple diameters D of the cylinder electrode. Results show that the absolute value of both extrema decreases with increasing electrode diameter. Subsequently, E×B drifts experienced by the protons decrease. The drift distance of the particle guiding center $D^{\text{gc}}_{\text{E×B}}$ as a function of the electrode diameter D is shown in Fig. 5.35 for multiple proton initial kinetic energies T_0 and pitch angles θ_0. Results show that phase angle variations also decrease with increasing electrode diameter for all particle energies and pitch angles since the electric field induced by the electrode becomes more homogeneous. However, improvements obtained for low and high energetic protons by increasing the electrode diameter from 24 cm to 28 cm are not sufficient.

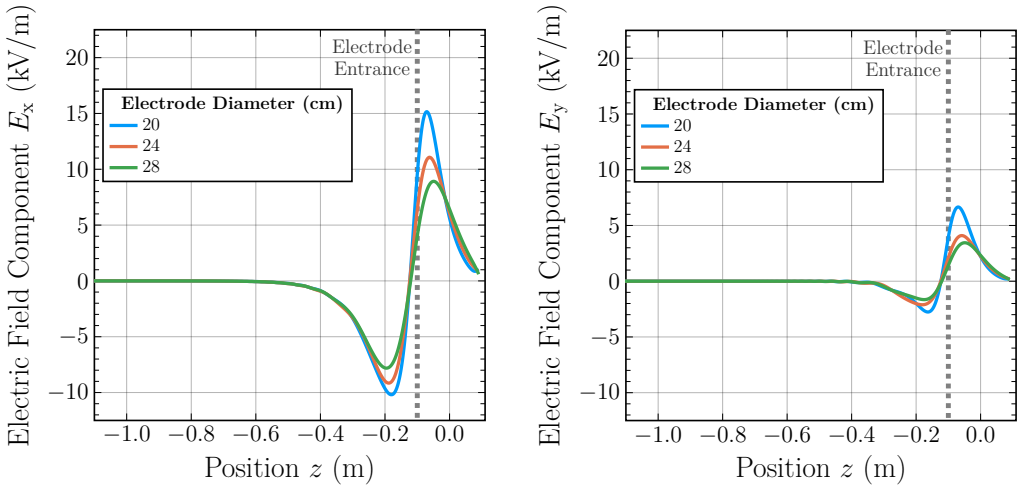


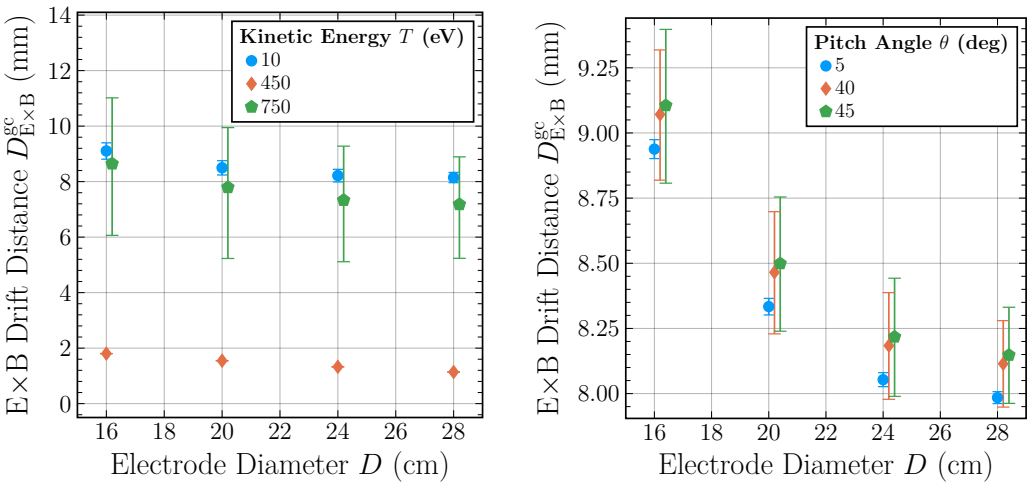
Figure 5.34: Normal electric field components (a) E_x and (b) E_y evaluated along the trajectory of a proton of initial kinetic energy $T_0 = 10\,\text{eV}$, pitch angle $\theta_0 = 45°$ and phase angle $\varphi_0 = 0°$ for multiple diameters D of the cylinder electrode. The normal fields experienced by the proton decrease if the electrode diameter is large.

Proton Post-acceleration Potential

The normal electric field components E_x and E_y and, thus, E×B drifts experienced by the protons can be significantly reduced if a lower post-acceleration potential is chosen (see Fig. D.3). The drift distance of the particle guiding center $D^{\text{gc}}_{\text{E×B}}$ is shown in Fig. 5.36 as a function of the post-acceleration potential $|U_A|$ for multiple proton kinetic energies T_0 and pitch angles θ_0. It can be seen that $D^{\text{gc}}_{\text{E×B}}$ and phase angle variations decrease significantly, independent on the particle energy and pitch angle, if the post-acceleration potential is reduced from 15 kV to 5 kV. In such a setup, all particles drift by distances below 5 mm.

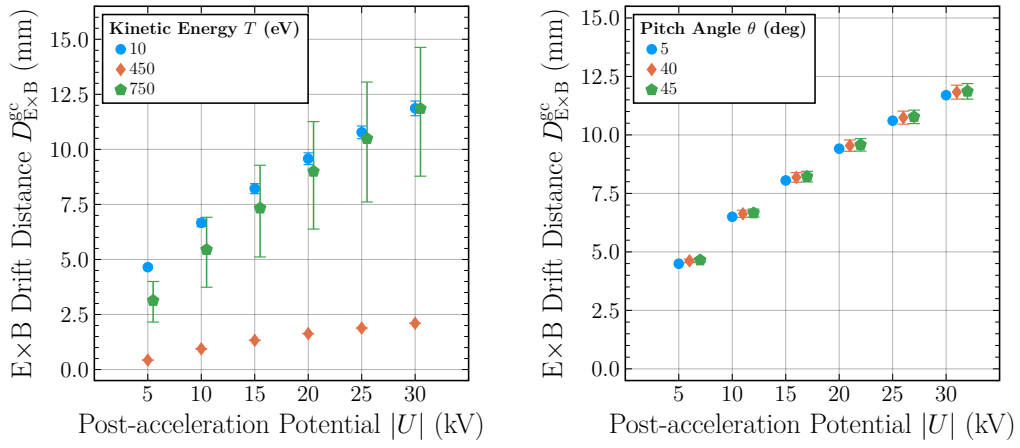
Electrode Length

The homogeneity of the electrostatic potential (see Fig. 5.13) and, thus, of the electric field inside the electrode depends, among other parameters, on the electrode length L. Fig. 5.37 shows the normal electric field components E_x and E_y for multiple electrode lengths L, evaluated along the trajectory of a proton with initial kinetic energy $T_0 = 10\,\text{eV}$ and pitch angle $\theta_0 = 45°$. Results show an increase of the electric field maximum present at the electrode entrance when the electrode length is increased from 10 cm to 20 cm. Additionally, the strength of both E_x and E_y at the end of the particle trajectory decreases. A further increase of the electrode



(a) (b)

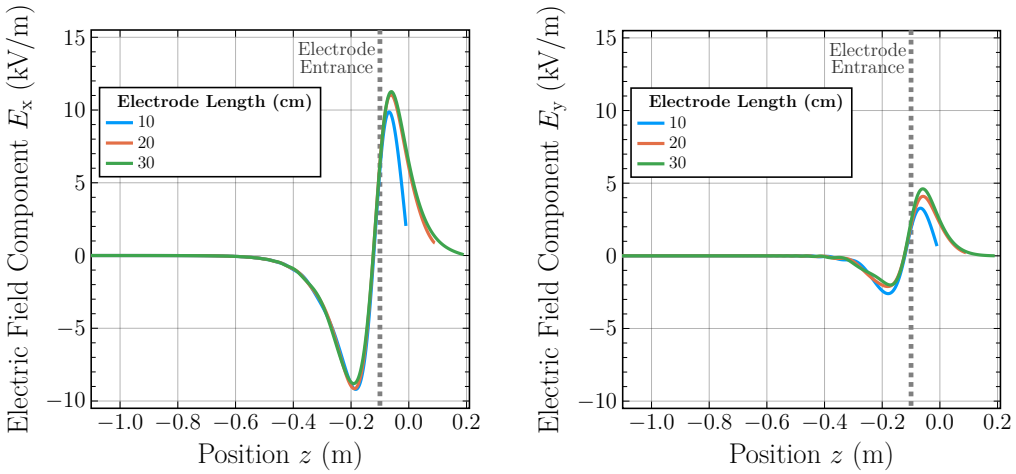
Figure 5.35: Drift distance $D^{gc}_{E\times B}$ of the particle guiding center, evaluated at the end of the particle trajectory, as a function of the cylinder electrode diameter D for multiple initial proton (a) kinetic energies T_0 and (b) pitch angles θ_0. Low and high energetic protons drift by smaller distances if the electrode diameter is large. For a better comparison, data in (a) are shifted by 0.2 cm for $T_0 = 750$ eV. In (b), data for θ_0 of 40° and 45° are shifted by 0.2 cm and 0.4 cm, respectively.



(a) (b)

Figure 5.36: Drift distance $D^{gc}_{E\times B}$ of the particle guiding center, evaluated at the end of the particle trajectory, as a function of the post-acceleration potential $|U_A|$ applied at the cylinder electrode for multiple (a) proton kinetic energies T_0 and (b) pitch angles θ_0. Drifts of the protons can be significantly if small a post-acceleration potential is chosen. Variation bars also decrease considerably. For a better comparison, data in (a) are shifted by 0.5 kV for $T_0 = 750$ eV. In (b), data for θ_0 of 40° and 45° are shifted by 1 kV and 2 kV, respectively.

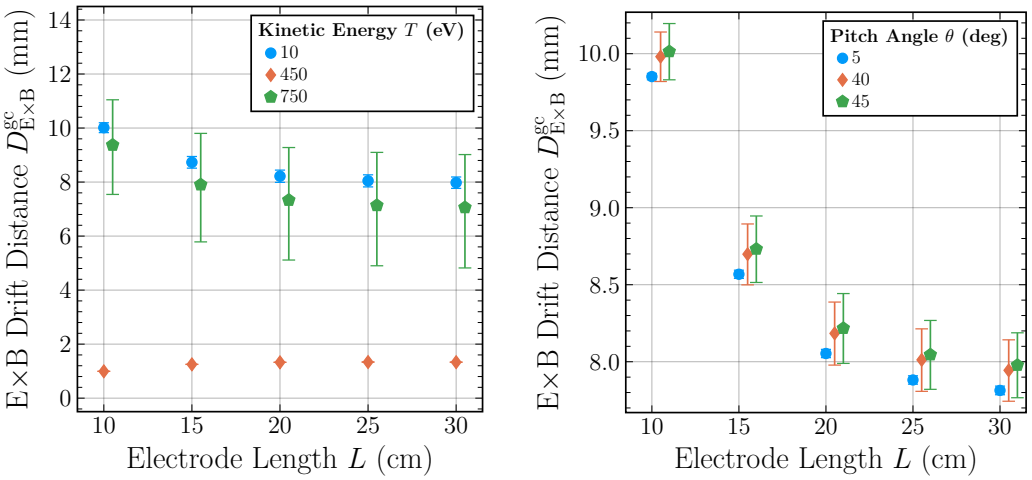
length to 30 cm does not affect the fields at the electrode entrance. However, if the electrode is long enough, both field components converge inside the electrode towards zero. Although normal field components increase inside the electrode for longer electrodes, the net drift experienced by the protons decreases due to larger compensations in the direction of the drift. This is shown in Fig. 5.38, where the drift distance of the particle guiding center $D^{gc}_{E\times B}$ is evaluated as a function of the electrode length L for multiple initial proton kinetic energies T_0 and pitch angles θ_0. Since the magnitude and width of the electric field maximum at the electrode entrance are not



(a) (b)

Figure 5.37: Normal electric field components (a) E_x and (b) E_y, evaluated along the trajectory of a proton of initial kinetic energy $T_0 = 10\,\text{eV}$, pitch angle $\theta_0 = 45°$ and phase angle $\varphi_0 = 0°$ for multiple lengths L of the cylinder electrode. The normal electric fields experienced by the proton inside the electrode decrease if the electrode is short. Note that for a better comparison data are shifted by $-0.1\,\text{m}$ and $0.1\,\text{m}$ for electrode lengths of 10 cm and 30 cm, respectively.

significantly affected by an increase of the electrode length above 20 cm, $D^{\text{gc}}_{\text{E×B}}$ and phase angle variations do not decrease sufficiently for low and high energetic protons, independent on the particle pitch angle θ_0.



(a) (b)

Figure 5.38: Drift distance $D^{\text{gc}}_{\text{E×B}}$ of the particle guiding center, evaluated at the end of the particle trajectory, as a function of the cylinder electrode length L for multiple (a) proton kinetic energies T_0 and (b) pitch angles θ_0. The protons drift by smaller amounts if the electrode is long. For a better comparison, data in (a) are shifted by 0.5 cm for $T_0 = 750\,\text{eV}$. In (b), data for θ_0 of 40° and 45° are shifted by 0.5 cm and 1 cm, respectively.

Results have shown that E×B drifts experienced by the decay protons can not be suppressed by a simple adjustment of the electrode diameter and length. As in the study of the adiabatic particle transport, one effective tool to minimize the distance by which the protons drift as they move towards the detector is the post-acceleration potential applied at the electrode. Further

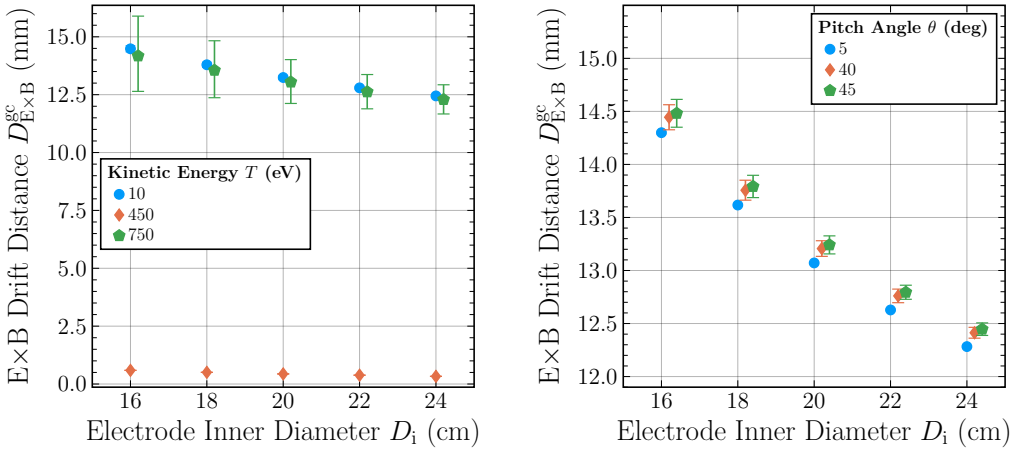
geometrical adjustments are however required to minimize energy and phase angle variations of the E×B drift effect.

5.5.2 Adjustments to the Field Degrader

In the field degrader setup, regions of non-uniform electric fields are present in the vicinity of the entrance ring (see Fig. 5.32). The field degrader should be adjusted such that the extremum of the normal field components E_x and E_y present at the electrode entrance is minimized. In the following, multiple geometrical and electrical adjustments of the field degrader are studied.

Electrode Inner Diameter and Length

Similar to the cylinder electrode, the absolute strength of the normal electric field components and, thus, drifts of the particle guiding center $D^\mathrm{gc}_\mathrm{E\times B}$ decrease for electrodes of larger diameters. In the following, a variation of the electrode inner diameter D_i for an electrode of length $L = 20\,\mathrm{cm}$ and outer diameter $D_\mathrm{o} = 28\,\mathrm{cm}$ is considered. Fig. 5.39 shows $D^\mathrm{gc}_\mathrm{E\times B}$ as a function of the electrode inner diameter for multiple initial kinetic energies T_0 and pitch angles θ_0 of the protons. It can be seen that $D^\mathrm{gc}_\mathrm{E\times B}$ decreases approximately linearly (over the range considered) with increasing electrode diameter for all energies and pitch angles. Since the electric field generated by electrode of larger inner diameter becomes more homogeneous, variations from the mean value $D^\mathrm{gc}_\mathrm{E\times B}$ decrease for protons with different initial phase angles φ_0. The effects are most pronounced for high energetic protons with large pitch angles, which cover wider regions of the electric field, compared to low energetic protons.



(a) (b)

Figure 5.39: Absolute deviation $D^\mathrm{gc}_\mathrm{E\times B}$ of the particle guiding center, evaluated at the end of the particle trajectory, as a function of the field degrader inner diameter D_i for multiple (a) proton kinetic energies T_0 and (b) pitch angles θ_0. A large inner diameter of the field degrader is required to reduce the drifts experienced by the decay protons. For a better comparison, data in (a) are shifted by 0.2 cm for $T_0 = 750\,\mathrm{eV}$. In (b), data for θ_0 of 40° and 45° are shifted by 0.2 kV and 0.4 kV, respectively.

The increment of the surface potential applied at the electrode rings and the number of individual rings can be adjusted to reduce the electric field strength (see Fig. 5.26a) and, thus, the drifts experienced by protons. In the following, a field degrader of length L of 20 cm, 30 cm and 40 cm (labeled as setup 1 to 3) composed of 11, 16 and 21 individual rings combined with an increment of the surface potential applied at the electrode rings of $-1.5\,\mathrm{kV}$, $-1\,\mathrm{kV}$ and $-0.75\,\mathrm{kV}$, respectively, is considered (see Table C.1). All other electrode parameters remain unchanged.

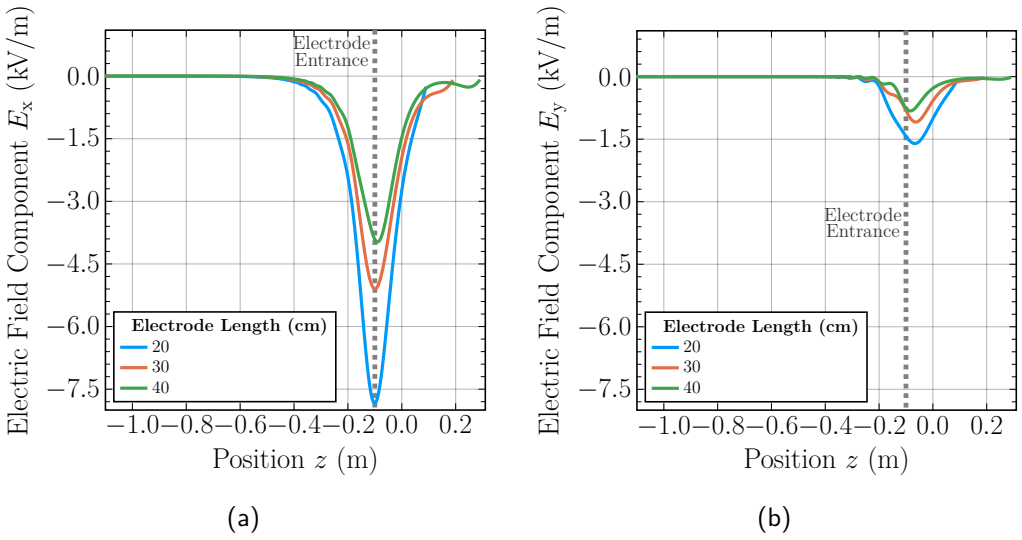


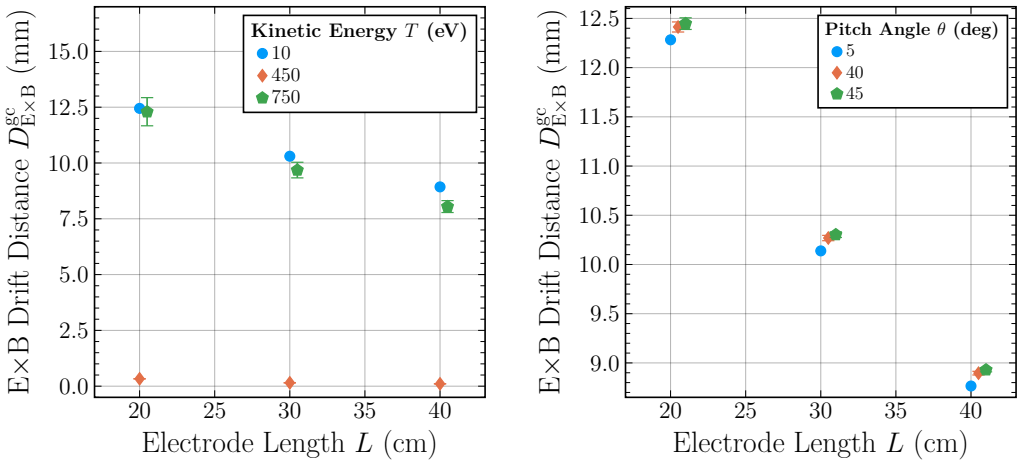
Figure 5.40: Normal electric field components (a) E_x and (b) E_y as a function of position z for a proton of initial kinetic energy $T_0 = 10\,\mathrm{eV}$, pitch angle $\theta_0 = 45°$ and phase angle $\varphi_0 = 0°$ for multiple lengths L of the field degrader. Note that a variation of the electrode length is combined with an adjustment of the surface potential applied at the individual electrode rings according to Table C.1. Additionally, for a better comparison data are shifted by 0.1 m and 0.2 m for electrode lengths of 30 cm and 40 cm, respectively. The normal electric fields experienced by the proton at the electrode entrance decrease if the electrode is long. However, a second minimum forms in regions close to the electrode end plate.

Fig. 5.40 shows the normal electric field components E_x and E_y along the trajectory of a proton of initial kinetic energy $T_0 = 10\,\mathrm{eV}$ and pitch angle $\theta_0 = 45°$ for the multiple lengths L of the electrode. Note that for a better comparison, data are shifted for the various electrode lengths to match the position of the electrode entrance in all setups. It can be seen that the electric field generated by a longer electrode, combined with smaller increments of the surface potential applied between subsequent rings, decreases in (absolut) strength. However, the electric field becomes less uniform in the lower half of the electrode. This is reflected in the presence of a second minimum for an electrode of length $L = 40\,\mathrm{cm}$. Thus, protons might experience additional drifts over this region. The drift distance $D^{\mathrm{gc}}_{\mathrm{E\times B}}$ of the particle guiding center, evaluated at the end of the particle trajectory, is shown in Fig. 5.41 as a function of the electrode length L for multiple initial proton kinetic energies T_0 and pitch angles θ_0. The drift of the proton guiding center decreases for longer electrodes, for all particle energies and pitch angles. As the field becomes more homogeneous for longer electrodes, variations from the mean value $D^{\mathrm{gc}}_{\mathrm{E\times B}}$ also decrease. The effects become, however, smaller for electrodes longer than 30 cm, since the electric field becomes less uniform in regions close to the electrode end plate.

One optional feature of the field degrader is the concentric wire grid, which can be attached at the entrance ring. The E×B drifts experienced by the protons in such a setup are evaluated in the following.

Wire Grid Field Degrader

According to studies performed in Section 5.3.4, the homogeneity of the potential inside the electrode can be improved by attaching the circular wire grid at the electrode entrance ring. This additionally shields the detection region from large electrostatic potentials. The potential generated by the electrode in the wire plane is, however, strongly inhomogeneous. In the following, a



(a) (b)

Figure 5.41: Drift distance $D^{gc}_{E\times B}$ of the particle guiding center, evaluated at the end of the particle trajectory, as a function of the field degrader length L for multiple (a) proton kinetic energies T_0 and (b) pitch angles θ_0. Note that the length of the field degrader is increased by adding rings to the existing electrode setup (see Table C.1). The potential gradient across the electrode rings is linear in each electrode setup. Protons drift by smaller distances if the length of the field degrader is increased and the increment of the surface potential applied to the electrode rings is small. For a better comparison, data in (a) are shifted by 0.5 cm for $T_0 = 750$ eV. In (b), data for θ_0 of 40° and 45° are shifted by 0.5 kV and 1 kV, respectively.

wire grid field degrader described by setup 1 in Table C.2 is considered.

The normal electric field components E_x and E_y evaluated along the trajectory of a proton of energy $T_0 = 10$ eV and pitch angle $\theta_0 = 45°$ are shown in Fig. 5.42. Due to the shielding effect, normal electric fields experienced by the proton before entering the electrode are small. However, both field components increase abruptly when the proton passes the wire grid plane. This is caused by the strong normal electric fields present at the wires (see Fig. D.6). Inside the electrode, both normal field components are small. Fig. 5.43 shows the drift distance of the particle guiding center $D^{gc}_{E\times B}$ as a function of the initial proton kinetic energy T_0 and pitch angle θ_0. A comparison of the field degrader with and without wire grid (see Fig. 5.33) shows that $D^{gc}_{E\times B}$ decreases considerably for all proton energies T_0 and pitch angles θ_0. Additionally, the dependence of $D^{gc}_{E\times B}$ on the particle initial energy is strongly reduced. This is due to the more uniform electric field generated by the field degrader in the electrode region when combined with the wire grid. However, variations of $D^{gc}_{E\times B}$ with the particle phase angle φ_0 become significant. As already mentioned in Section 5.4.2, large variations arise as the distance between the wires and the position of particles of the same energy and pitch angle changes, depending on the initial phase angle φ_0. Geometrical and electrical parameters of the field degrader require adjustments to minimize the E×B drifts experienced by the decay protons.

As in the discussion of non-adiabatic effects (see Section 5.4.2), two approaches to minimize the strong electric fields present in the wire plane are introduced: a combined variation of the number of electrode rings and of the surface potential applied at the rings and a double wire grid system. Studies performed in the following focus on the reduction of E×B drifts experienced by low energetic protons as they are accelerated by a wire grid field degrader.

Length Variation of the Wire Grid Electrode

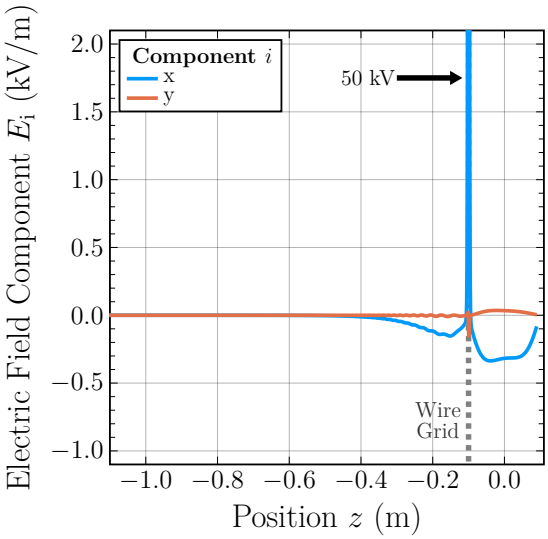
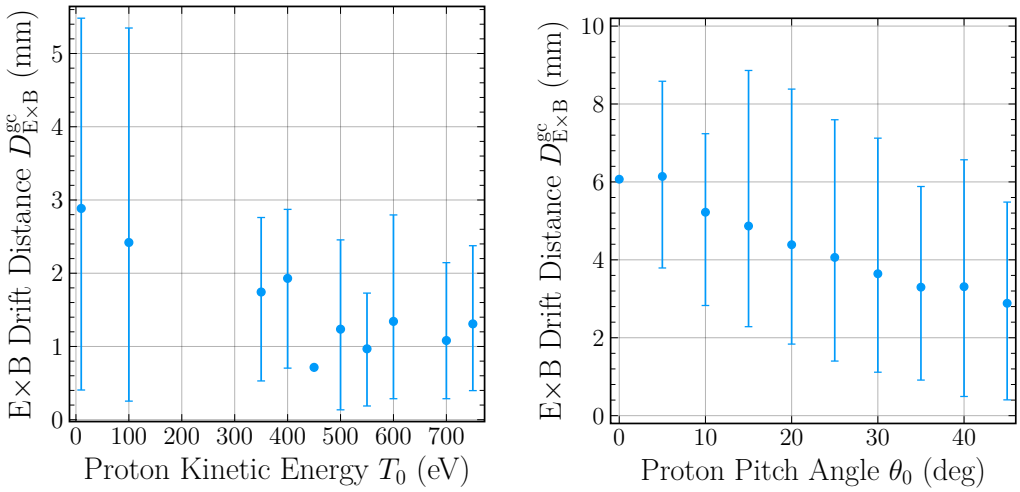


Figure 5.42: Normal electric field components E_x and E_y as a function of position z for a proton of initial kinetic energy $T_0 = 10\,\text{eV}$, pitch angle $\theta_0 = 45°$ and phase angle $\varphi_0 = 0°$ which is accelerated by the field degrader with the concentric wire grid attached at the entrance ring. Normal electric fields experienced by the proton before it enters the electrode are small. However, strong fields are present in the wire plane.



(a) (b)

Figure 5.43: Drift distance of the particle guiding center $D^{gc}_{E\times B}$, evaluated at the end of the particle trajectory, as a function of the initial proton(a) kinetic energy T_0 and (b) pitch angle θ_0, for protons accelerated by the field degrader with the concentric wire grid attached at the entrance ring. Protons experience smaller drifts, compared to the field degrader without the wire grid (see Fig. 5.33). However, variation bars increase considerably.

The variation of the number of electrode rings and of the surface potential applied at the rings is first considered. The wire grid electrodes used for the following studies have length $L =$ 20 cm, 30 cm and 40 cm (labeled as setup 1 to 3) and are composed of 11, 16 and 21 equidistant rings with an increment of the surface potential of -1.5 kV, -1 kV and -0.75 kV at the rings, respectively (see Table C.2). Results presented in Fig. 5.26a have shown that the strength of the electric field generated by the electrode decreases for longer electrodes with a small increment of the surface potential applied at the individual rings. The same is observed for the normal field components E_x and E_y (see Fig. D.7). Note that a second minimum of both E_x and E_y forms in the lower half of the electrode. Fig. 5.45 shows the drift distance of the particle guiding center $D^\mathrm{gc}_\mathrm{E\times B}$ as a function of the electrode length L for multiple initial proton kinetic energies T_0 and pitch angles θ_0. Results show that a long electrode can be effective in the reduction of the drifts experienced by low energetic protons with small initial pitch angles. However, the average drift is not considerably affected by such an adjustment of the electrode and phase angle variations remain significant. This is (partially) due to stronger normal electric fields present in the lower half of the electrode. Thus, further optimizations to the field degrader and wire grid are required to suppress this effect.

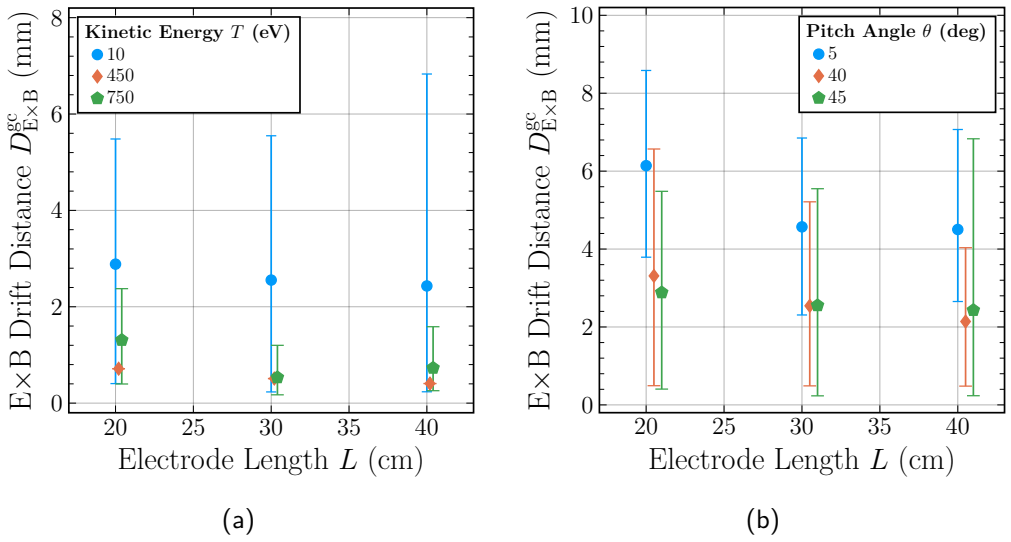
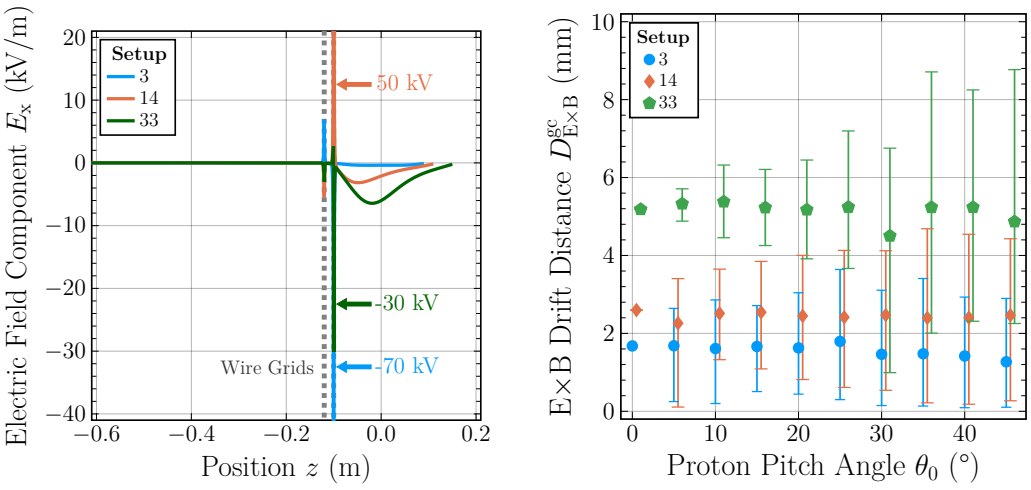


Figure 5.44: Drift distance of the particle guiding center $D^\mathrm{gc}_\mathrm{E\times B}$, evaluated at the end of the particle trajectory, as a function of the initial proton (a) kinetic energy T_0 and (b) pitch angle θ_0, for multiple lengths of the field degrader with the concentric wire grid attached at the entrance ring (see for setup description). For a better comparison, data in (a) are shifted by 0.2 cm and 0.4 cm for T_0 of 450 eV and 750 eV, respectively. In (b), data for θ_0 of 40° and 45° are shifted by 0.5 cm and 1 cm, respectively.

Double Wire Grid System

Results presented in Section 5.4.2 have shown that non-adiabatic effects can be reduced if the field degrader is used in combination with a double wire grid system. Here, the same setups of the post-acceleration electrode, label as 3, 14 and 33 (see Tables C.3 to C.5) are considered and the normal electric fields and E×B drifts experienced by the decay protons are compared. Fig. 5.45a shows the normal electric field component E_x along the trajectory of a proton of energy $T_0 = 10$ eV and pitch angle $\theta_0 = 0°$. Note that for a better comparison of the three setups, data are shifted to match the various positions of the electrode entrances. Results show that strong electric fields are present in the two wire planes, independent on the chosen setup.



(a) (b)

Figure 5.45: (a) Normal electric field component E_x as a function of position z, evaluated for a proton of initial kinetic energy $T_0 = 10\,\text{eV}$, pitch angle $\theta_0 = 45°$ and phase angle $\varphi_0 = 0°$ for multiple setups of the field degrader including a double wire grid system attached at the electrode entrance (see for setup description). (b) Drift distance of the particle guiding center $D^{gc}_{E\times B}$, evaluated at the end of the particle trajectory, as a function of the particle pitch angle θ_0 for $T_0 = 10\,\text{eV}$. For a better comparison, data in (a) are shifted by 2 cm and 6 cm for setups 14 and 33. In (b), data for setups 14 and 33 are shifted by 0.5° and 1°, respectively.

However, the wire grid system is shielded more effectively from large electric fields if additional electrode rings are added to the field degrader, as in setups 14 and 33. Hence, the normal field component E_x experienced by the proton when passing the wire grid system decreases. Such setups come, however, with a disadvantage: the electric field inside the field degrader becomes less uniform and the minimum of the normal field component E_x present inside the electrode increases. Therefore, protons experience larger drifts, compared to setup 3 of the wire grid field degrader. Fig. 5.45b shows the drift distance of the particle guiding $D^{gc}_{E\times B}$ as a function of the initial proton pitch angle θ_0 for a proton of energy 10 eV in the three proposed setups. It can be seen that $D^{gc}_{E\times B}$ is below 2 mm in setup 3, independent on the particle pitch angle. The largest drifts are experienced by protons in setup 33, where $D^{gc}_{E\times B}$ is in the order of 5 mm. Phase angle variations remain, however, significant independent on the chosen field degrader setup.

So far, only variations of geometrical and electrical electrode parameters have been considered in the studies performed for the adiabatic particle transport and E×B drift effects. Promising results have been obtained for the field degrader. To further minimize non-adiabatic effects and drifts of the decay protons, an adjustment of the proton beam can be considered. Studies performed in the following section aim to determine the effect of a particle beam size and position adjustment on the systematic effects mentioned above.

5.6 Further Studies

Results have shown that low and high energetic protons follow trajectories along regions of (strongly) non-uniform electric fields when they are accelerated by the cylinder electrode and field degrader, if they enter the detection region at large distances from the system central axis z. Non-adiabatic effects and E×B drifts experienced by such protons are significant. On the other

hand, effects on protons of initial kinetic energy 450 eV, which gyrate around the central axis z towards the sensor, are suppressed. This is due to vanishing normal electric fields along the axis of symmetry and the relatively homogeneous electric fields experienced by the gyrating protons. This feature of the electric field can be used to minimize non-adiabatic effects and E×B drifts experienced by low energetic protons. Possible geometrical adjustments to achieve this are: a reduction of the proton beam size by an increase of the magnetic field or a radial shift of the particle beam and, thus, of the proton sensor. Since the most promising result obtained so far have been achieved for the field degrader, investigations presented in this section consider only this electrode type. The focus lies on studies of non-adiabatic effects and E×B drifts.

5.6.1 Proton Beam Size

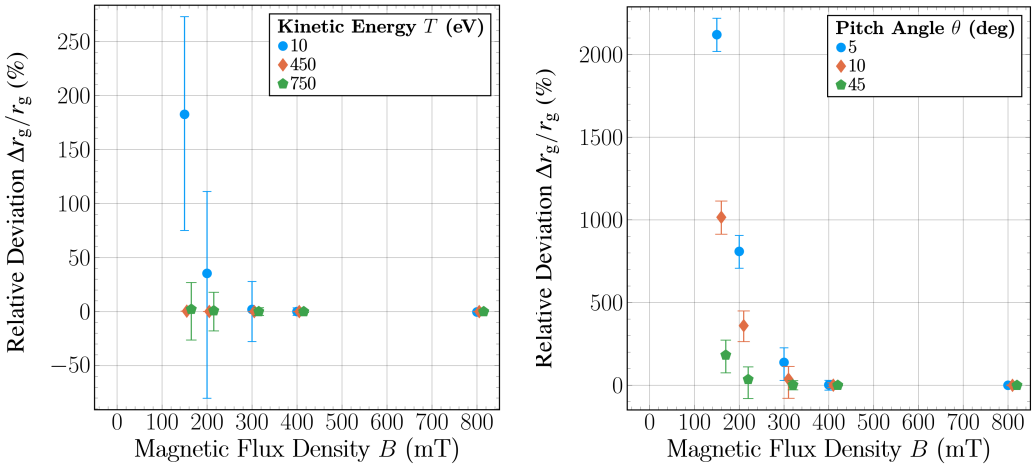
The proton beam size is determined (among other parameters) on the one hand by the aperture and on the other hand by the magnetic flux density of the guiding field. The magnetic field determines the gyrations radius of a particle of energy T and pitch angle θ. Particles moving in larger magnetic fields follow helical orbits of smaller gyration radii and pitch heights (see Eq. (2.5)). Therefore, protons cover narrower regions of the electric field and experience smaller field gradients. The magnetic flux density also affects the distance by which the particles drift inside the R×B drift region. An increase of the magnetic field results in a decrease of the width of the drift distance spectrum (and, thus, beam size) as shown in Fig. 4.17a. In a smaller beam size, low and high energetic protons follow trajectories closer to the symmetry axis, where the electric field is more homogeneous and normal components are smaller. Simulations presented in the following were performed for the field degrader in the standard configuration (see Section 5.1.2).

Adiabatic Particle Transport

A significant reduction of non-adiabatic effects can be achieved by increasing the magnetic flux density B of the guiding field. The influence of the magnetic flux density B on the relative deviation of the particle gyration radius $\Delta r_\mathrm{g}/r_\mathrm{g}$, including phase angle variations, is shown in Fig. 5.46 for multiple proton energies T_0 and pitch angles θ_0. Results show that $\Delta r_\mathrm{g}/r_\mathrm{g}$ and variation bars decreases with $1/B$ for all energies and pitch angles. Non-adiabatic effects are strongly suppressed for magnetic flux densities above 400 mT.

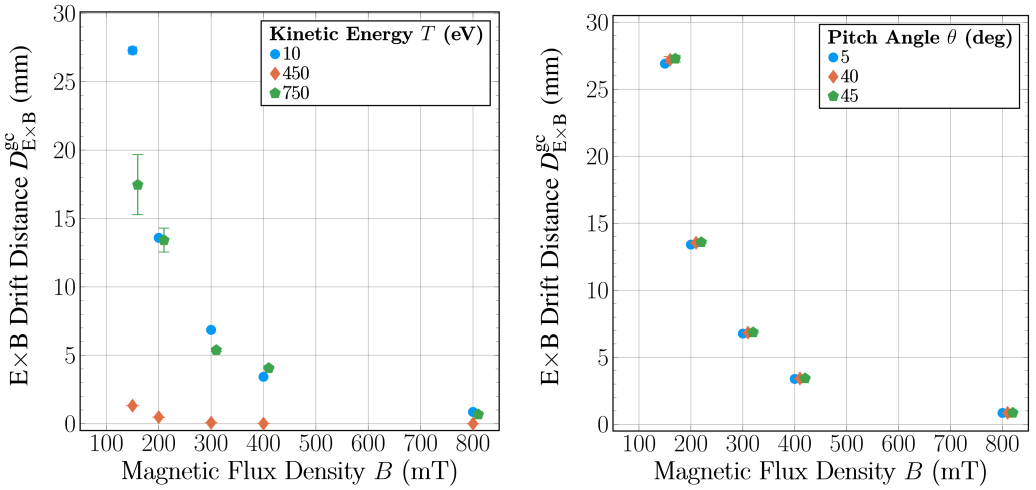
E×B Drift Effect

In addition to the effects of the magnetic field on the proton beam size mentioned previously, an increase of the magnetic flux density B affects the E×B drift velocity $\boldsymbol{v}_\mathrm{ExB}$ of the protons (see Eq. (2.11)). The drift velocity is indirectly proportional to B. Thus, drifts experienced by protons as they gyrate towards the sensor can be minimized by increasing the magnetic field. Fig. 5.47 shows the drift distance $D^\mathrm{gc}_\mathrm{E\times B}$ of the particle guiding center, including phase angle variations, as a function of the magnetic flux density B for multiple proton kinetic energies T_0 and pitch angles θ_0, evaluated at the end of the particle trajectory. For a magnetic field of 800 mT, $D^\mathrm{gc}_\mathrm{E\times B}$ is below 2.5 mm for all particle energies and pitch angles. It can be seen that variation bars also decrease significantly for larger magnetic fields.



(a) $\theta_0 = 45°$ (b) $T_0 = 10\,\text{eV}$

Figure 5.46: Relative deviation $\Delta r_g/r_g$ of the particle gyration radius, evaluated at the end of the particle trajectory, as a function of the initial proton (a) kinetic energy T_0 and (b) pitch angle θ_0 for multiple magnetic flux densities B. Non-adiabatic effects of the protons are suppressed for magnetic flux densities B above 400 mT.



(a) $\theta_0 = 45°$ (b) $T_0 = 10\,\text{eV}$

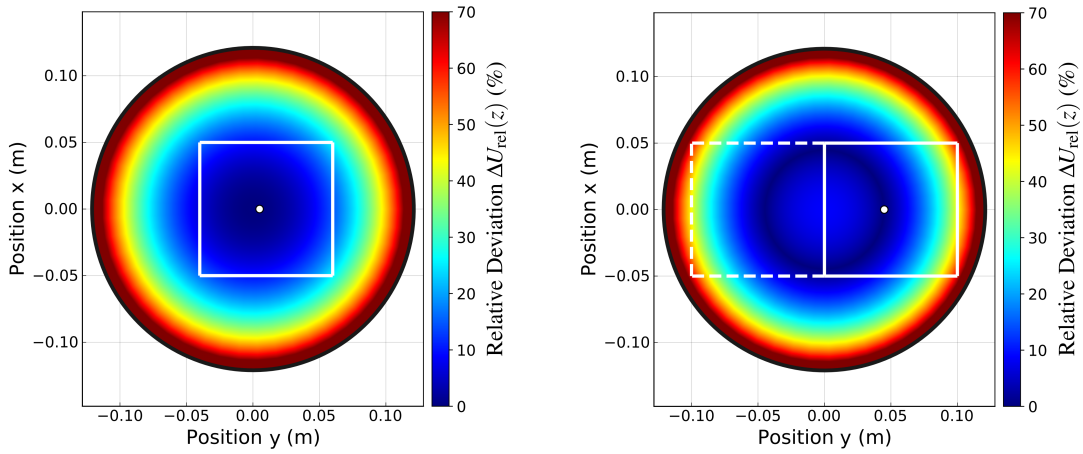
Figure 5.47: Drift distance $D^{gc}_{E\times B}$ of the particle guiding center, evaluated at the end of the particle trajectory, as a function of the magnetic flux density B for multiple proton (a) kinetic energies T_0 and (b) pitch angles θ_0. Drifts of the decay protons are in the order of 1 mm for a magnetic field of 800 mT.

5.6.2 Proton Beam Shift

In Section 5.4, results have shown that non-adiabatic effects and E×B drifts experienced by medium energetic protons which follow trajectories close to the axis of symmetry z are significantly smaller, compared to low (and high) energetic protons which enter the detection region at larger radial distances. To minimize effects observed for low energetic protons, a shift of the proton beam and, thus, of the proton detector can be considered. A shift of the proton beam in positive direction y translates to a shift of low energetic protons closer to the axis of symmetry z. The opposite holds for high energetic protons. The location of the proton detector needs to be adjusted accordingly. The following studies consider a shift Δy of the proton beam in the

range between 0 mm to 40 mm in steps of 10 mm, corresponding to a shift Δy of the simulated proton spectrum shown Fig. 5.1. Note that a beam shift of 40 mm yields the proton spectrum considered in the simultaneous measurement of electrons and protons in Chapter 4 (see Fig. 4.17). Thus, in such a geometry, a second sensor (of same size) can be fitted into the electrode for the measurement of decay electrons. In this section, the effect of the proton beam shift on the particle transport and E×B drifts experienced by protons are studied. A field degrader of length $L = 40$ cm composed of 21 individual rings with an increment of the surface potential applied between subsequent electrode rings of -0.75 kV (see setup 3 in Table C.1) and a magnetic field of 220 mT are considered. This electrode setup is chosen for the following investigations, since it provided the best results in the evaluation of the adiabatic particle transport.

To illustrate the effect of a beam shift, the relative change of the electrostatic potential ΔU_{rel} across the proton beam for a beam shift of Δy of 0 mm and 40 mm is first compared. Fig. 5.48 shows ΔU_{rel} in the x-y-plane at $x = 0$ m for both beam setups, evaluated at a distance of 20 cm above the sensor, corresponding to the location of the electrode entrance. The reference potential U_{ref} is evaluated at the center of the proton beam[11]. It can be seen that for a beam shift of Δy = 40 mm, a second sensor (withe, dashed rectangle) can be fitted at the electrode end plate next to the proton sensor (withe, solid rectangle) for the detection of decay electrons. Results show that relative variations of the electrostatic potential increase considerably in the regions covered by high energetic protons. The maximum relative potential deviation ΔU_{rel} increases by 195 % to about 62 % at a distance of 40 cm from the sensor for $\Delta y = 40$ mm, compared to the initial beam setup. Further evaluations of the relative potential at smaller distances from the sensor also yield an increase of ΔU_{rel} with larger proton beam shifts. However, effects remain small in the vicinity of the proton sensor. At a distance of 1 cm from the sensor, variations of the electrostatic potential remain below 0.5 % across the proton beam for a shift $\Delta y = 40$ mm of the proton beam.



(a) Input data: $U_{\mathrm{ref}} = -1.3$ kV

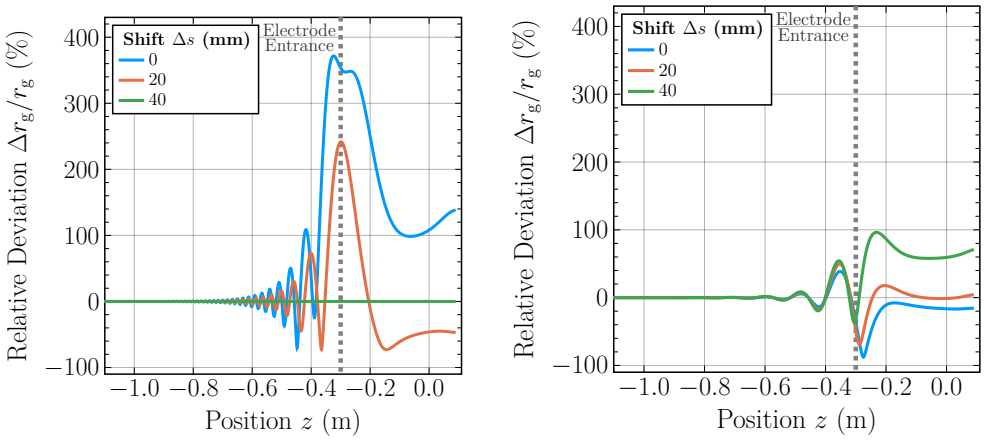
(b) Input data: $U_{\mathrm{ref}} = -1.2$ kV

Figure 5.48: Relative deviation ΔU_{rel} of the electrostatic potential evaluated in the x-y-plane at a distance of 1 cm above the proton sensor for shifts Δy of (a) 0 mm and (b) 40 mm of the proton beam. The proton sensor and the inner edge of the electrode are marked by the withe rectangle and black circle, respectively. The potential reference value U_{ref} is evaluated at the center of the proton beam (marked by the withe dot). If the proton beam (and, thus, the proton sensor) is shifted by 40 mm in positive direction y, the electron detector (withe, dashed rectangle) can be fitted into the electrode for a simultaneous measurement of the decay particles. However, high energetic protons cover regions of strongly inhomogeneous potentials as they gyrate towards the proton sensor.

[11] The center of the proton beam is located at position $y = 0.5$ cm and $y = 4.5$ cm for a beam shift of Δy of 0 mm and 40 mm, respectively.

Adiabatic Particle Transport

In the following, effects of the proton beam shift on the adiabaticity of the particle transport are studied. Fig. 5.49 shows the relative change of the particle gyration radius $\Delta r_\mathrm{g}/r_\mathrm{g}$ along the trajectory of a proton of pitch angle 5° and an initial kinetic energy T_0 of 10 eV and 750 eV for multiple shifts Δy of the proton beam. Oscillations of $\Delta r_\mathrm{g}/r_\mathrm{g}$ for the 10 eV proton decrease for larger shifts of the proton beam. Effects are suppressed when the beam is shifted by 40 mm. However, if such a setup is considered, relative changes $\Delta r_\mathrm{g}/r_\mathrm{g}$ of the gyration radius of a 750 eV proton increase considerably inside the electrode.



(a) $T_0 = 10$ eV (b) $T_0 = 750$ eV

Figure 5.49: Relative change of the particle gyration radius $\Delta r_\mathrm{g}/r_\mathrm{g}$ as a function of position y for a proton of initial pitch angle $\theta_0 = 5°$ and kinetic energy T_0 of (a) 10 eV and (b) 750 eV. The location of the electrode entrance is marked by the gray, dashed vertical line. (a) Oscillations of the gyration radius are suppressed if the proton beam is shifted by 40 mm as the proton enters the detection region on-axis. (b) The proton gyrates towards the sensor at large distances from the axis of symmetry for larger shifts of the beam. Non-adiabatic effects increase considerably for such protons.

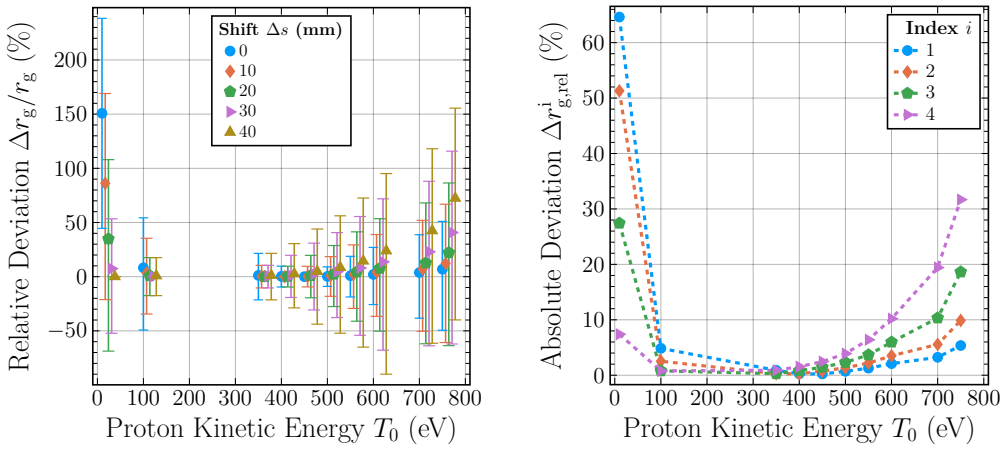
The relative deviation of the particle gyration radius $\Delta r_\mathrm{g}/r_\mathrm{g}$ at the end of the particle trajectory is shown in Fig. 5.50a as a function of the proton kinetic energy T_0, at a fixed pitch angle $\theta_0 = 5°$, for multiple shifts Δy of the proton beam. Results show that:

- Relative deviations $\Delta r_\mathrm{g}/r_\mathrm{g}$ and φ_0-variations can be considerably reduced for protons with initial kinetic energies up to 350 eV for shifts of the proton beam below 30 mm.
- For kinetic energies above 450 eV, $\Delta r_\mathrm{g}/r_\mathrm{g}$ and φ_0-variations increase for all beam shifts Δy. This is due to significant potential and electric field gradients experienced by the protons, which enter the detection at larger distances from the central axis z.
- Relative changes of the gyration radius for medium energetic protons (which are most abundant) are less affected by the shift of the proton beam.

This behavior is also reflected in the absolute deviation of the particle gyration radius $\Delta r^\mathrm{i}_\mathrm{g,rel}$ between two consecutive beam shifts Δy^i and $\Delta y^{\mathrm{i}-1}$, defined as

$$\Delta r^\mathrm{i}_\mathrm{g,rel} = |\Delta r^i_\mathrm{g}/r^i_\mathrm{g} - \Delta r^{i-1}_\mathrm{g}/r^{i-1}_\mathrm{g}|, \tag{5.1}$$

as shown in Fig. 5.50b.



(a) (b)

Figure 5.50: (a) Relative deviation of the particle gyration radius $\Delta r_g/r_g$ as a function of the initial proton kinetic energy T_0 for a pitch angle $\theta_0 = 5°$, evaluated at the end of the particle trajectory. (b) Absolute deviation of the particle gyration radius $\Delta r^i_{g,rel}$ between consecutive shifts of the proton beam as a function of the initial proton energy T_0 for $\theta_0 = 5°$. Non-adiabatic effects are minimized for protons of kinetic energies up to 350 eV for shifts of the proton beam below 30 mm. However, effects increase considerably for higher energetic protons.

Additional information on systematic effects introduced by a misalignment between the proton beam and proton detector can be obtained from Fig. 5.50b. Absolute deviations $\Delta r^i_{g,rel}$ are small for protons of initial kinetic energy 350 eV for misalignments of up to 40 mm between the proton beam and sensor. Effects become, however, significant for low (10 eV) and high (750 eV) energetic protons.

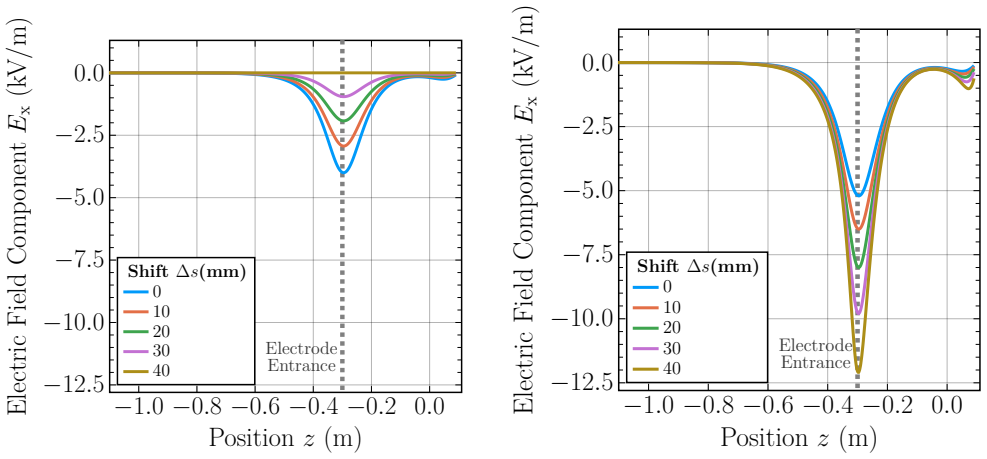
E×B Drift Effect

Normal electric fields experienced by a decay proton are weaker if the particles gyrates towards the sensor at small distances from the axis of symmetry z. Fig. 5.51 shows E_x evaluated along the trajectory of a proton with pitch angle $\theta_0 = 0°$ and a kinetic energy T_0 of 10 eV and 750 eV. The normal electric field experienced by the low energetic proton decreases significantly with increasing beam shift Δy and vanishes for $\Delta y = 40$ mm, when the proton enters the detection region on-axis. The high energetic proton, on the other hand, follows trajectories at larger distances from the axis of symmetry, where the normal field components are large. The minima present at the electrode entrance and in the lower electrode half increase significantly with Δy. This causes larger drifts for higher energetic protons.

The drift distance of the particle guiding center $D^{gc}_{E\times B}$, evaluated at the end of the particle trajectory, is shown in Fig. 5.52 as a function of the initial proton kinetic energy T_0 for a pitch angle θ_0 of 45°. E×B drifts experienced by particles of energies below 400 eV decrease considerably for shifts of the proton beam up to 40 mm. This trend is observed for all proton pitch angles θ_0. For such protons, drifts of the guiding center $D^{gc}_{E\times B}$ are below 5 mm. For protons of energies above 400 eV, $D^{gc}_{E\times B}$ and variation bars increase for all (positive) shifts Δy.

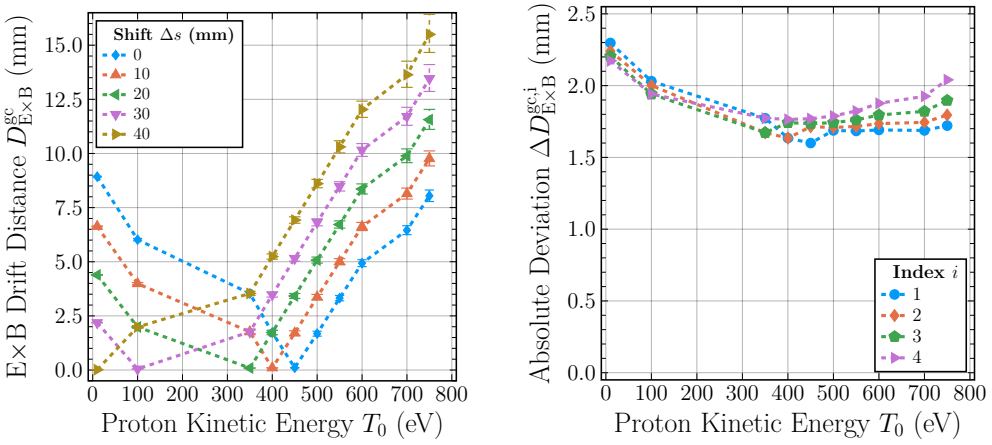
As in the adiabatic particle transport, a misalignment between the proton beam and sensor introduces uncertainties in the determination of the distance by which the protons drift. Fig. 5.52b shows the absolute deviation $\Delta D^{gc,i}_{E\times B}$ of the particle guiding center between two consecutive shifts of the proton beam Δy^i and Δy^{i-1}, which is defined as

$$\Delta D^{gc,i}_{E\times B} = |D^{gc,i}_{E\times B} - D^{gc,i-1}_{E\times B}|, \tag{5.2}$$



(a) $T_0 = 10\,\text{eV}$ (b) $T_0 = 750\,\text{eV}$

Figure 5.51: Normal electric field component E_x as a function of position z for a proton with a pitch angle $\theta_0 = 45°$ and kinetic energy T_0 of (a) 10 eV and (b) 750 eV, evaluated for multiple beam shifts Δy. Low energetic protons follow trajectories closer to the axis of symmetry z, where normal electric field components are small, if the beam is shifted by larger amounts. The opposite holds for high energetic protons.



(a) (b)

Figure 5.52: (a) Drift distance of the particle guiding center $D^{\text{gc}}_{\text{E×B}}$ as a function of the proton initial kinetic energy T_0 for a pitch angle $\theta_0 = 45°$ and multiple shifts Δy of the proton beam, evaluated at the end of the particle trajectory. (b) Absolute deviation of the particle guiding center $\Delta D^{\text{g,i}}_{\text{E×B}}$ between consecutive shifts of the proton beam as a function of the proton energy T_0 for $\theta_0 = 45°$. While protons with initial kinetic energies up to 350 eV drift by smaller amounts for larger shifts of the proton beam, protons of higher energies experience significant drifts.

as a function of the particle initial kinetic energy T_0 for a pitch angle $\theta_0 = 45°$. Results show that the effect of a misalignment is largest for low energetic protons. The uncertainty in the E×B drift is, however, below 0.25 mm for a misalignment of 1 mm between the proton beam and sensor.

5.7 Summary

The NoMoS experiment aims to measure the spectra of the electron and protons emitted in the decay of the free neutron. Since the decay protons are low energetic, a high voltage electrode is required to post-accelerate the protons to detectable energies prior to detection. The main focus of this chapter were investigations of systematic effects introduced by the high voltage post-acceleration electrode, based on the electrode requirements presented in Section 3.2, in the context of an individual measurement of the decay protons.

Studies performed in this chapter assume a symmetrical distribution of the proton drift distance spectrum around the central axis z at the end of the R×B drift region. For the proton post-acceleration, two electrode types were proposed: cylinder and field degrader. A comparison of the geometrical and electrical features of the two electrode types was presented in Sections 5.1 and 5.2. The cylinder electrode can be operated in two distinct modes, depending on the materials used in the manufacturing process. If the cylinder is a conductor, the electrode is operated at a constant surface potential U_{A}. Alternatively, a resistive foil can be used to induce a potential gradient across the cylinder surface when a potential difference is applied between the electrode entrance (ground potential) and end plate (U_{A}). A similar effect can be achieved using a field degrader. Such an electrode is composed of one circular end plate and multiple rings, which can be operated at distinct surface potentials. This introduces more flexibility in the design of the electrostatic potential and electric field generated by the field degrader inside the detection region, compared to the cylinder electrode. One optional feature of the field degrader is the concentric wire grid, which can be attached at the electrode entrance to further shape and restrict the electrostatic potential generated by the electrode.

Investigations of the electrode requirements discussed in Section 3.2 have shown that the two proposed electrodes do not fulfill all design criteria. The main findings are summarized in the following.

- **Electrostatic potential at large distances from the electrode**

  It was found that the electrostatic potential reaches wide into the detection region for both electrode types. The minimum length of the detection region, required to avoid potentials above -10 mV in the R×B drift region, was obtained for the resistive cylinder and the wire grid field degrader, with a minimum length of about 1.1 m and 0.9 m, respectively.

- **Penning traps**

  A Penning trap is present above the grounded entrance ring of the field degrader. Although the trap is not directly located in the regions covered by the decay protons, its depth is significant ($\Delta U = 484$ V). Its elimination is crucial for the suppression of background effects. It was found that the trap depth can be minimized by increasing the electrode inner diameter or by tilting the entrance ring away from the central axis z. For a tilt of 90°, ΔU was reduced to 260 V.

  Additional Penning traps ($\Delta U = 105$ V) are present above the individual wires, when the field degrader is used in combination with the concentric wire grid. Results have shown that a dense wire grid, with wires of large diameters, is required to minimize the trap depth ΔU.

- **Homogeneity of the electrostatic potential**

  Investigations of radial variations of the electrostatic potential at small distances from the proton sensor have shown that the potential is most homogeneous ($|\Delta U_{\mathrm{rel}}^{\mathrm{max}}| \ll 1$) when either the resistive cylinder or the wire grid field degrader is considered. Good results were obtained also for a cylinder electrode of length $L = 30\,\mathrm{cm}$.

  Potential inhomogeneities increase at larger distances from the proton detector in both detection setups. A large electrode inner diameter is required to achieve a better potential homogeneity in these regions, independent on the electrode type. For the field degrader, it was found that a gradual rotation of the individual electrode rings reduces inhomogeneities of the electrostatic potential at the electrode entrance. Both electrodes require, however, further adjustments to minimize radial potential variations at

  When used in combination with a wire grid, significant potential inhomogeneities arise in the wire plane of the field degrader. Results have shown that a sparse wire grid composed of thin wires is required to achieve a better homogeneity of the electrostatic potential in this plane.

- **Adiabatic particle transport**

  It was found that the particle transport, especially of protons with low initial kinetic energy and small pitch angles, is non-adiabatic in both setups. Protons experience large electric field gradients within one gyration period which cause oscillations of the particle gyration radius. Non-adiabatic effects are, however, significantly smaller in the field degrader setup. When used in combination with the wire grid, protons experience strong electric fields in the wire plane and relative changes of the particle gyration radius are significant. The following adjustments to the electrode have been found effective in the reduction of non-adiabatic effects:

  - Cylinder electrode: Reduction of the post-acceleration potential U_{A} applied to the electrode surface to $-5\,\mathrm{kV}$. Relative deviations of the particle gyration radius remain, however, significant for low energetic protons with small initial pitch angles.
  - Field degrader: Increase of the number of electrode rings combined with a small increment of the surface potential applied between consecutive rings. The best results were obtained for a field degrader composed of 21 rings with an increment of the surface potential of 0.75 kV (setup 3 in Table C.1).
  - Wire grid field degrader: Increase of the number of electrode rings combined with a double wire grid system. The surface potential applied at the two wire grids and to the additional rings should decrease in small steps. Improved results were obtained for setup 33 of the wire grid field degrader listed in Table C.5.

- **E×B drift effect**

  Results have shown that low and high energetic protons, which follow trajectories at large distances from the central axis z, experience large normal electric fields as they gyrate towards the sensor in both setups. This causes significant drifts of the protons. Although protons drift by smaller distances when they are accelerated by the cylinder electrode, effects show a strong dependence on the initial proton phase angle. The field degrader can be used in combination with the wire grid to obtain a more uniform electric field in the regions covered by the decay protons and to minimize the dependence of the E×B drift on the initial proton kinetic energy (and, thus, entry position) and pitch angle. The following adjustments of the various electrode types have been found most effective in the reduction of E×B drift effects:

- Cylinder electrode: Post-acceleration potential U_{A}: Independent on the initial kinetic energy and pitch angle, drifts of the protons are below 5 mm if the post-acceleration potential is reduced to -5 kV.
- Field degrader: Increase of the number of electrode rings in combination with a small increment of the surface potential applied between subsequent rings. Improved results were obtained for a field degrader of length $L = 40$ cm composed of 21 rings with an increment of the surface potential of 0.75 kV (see setup 3 in Table C.1).
- Wire grid field degrader: Increase of the number of electrode rings combined with a double wire grid system. The increment of the surface potential applied at the two wire grids and to the additional rings should be small. The best results were obtained for setup 3 of the wire grid field degrader listed in Table C.3. Here, drifts of the protons are in the order of 2 mm.

Additional investigations of the adiabatic particle transport and E×B drift effects have been performed in Section 5.6 considering variations of the magnetic field (and, thus, of the particle beam size) and shifts of the proton beam relative to the electrode. The studies were performed for the field degrader in the standard configuration (see Section 5.6.1) and for a field degrader composed of 21 rings with an increment of the surface potential applied at the individual rings of 0.75 kV (see Section 5.6.2), respectively. It was found that:

- Non-adiabatic effects are suppressed for magnetic flux densities above 400 mT. A suppression of E×B drifts was achieved for a magnetic flux density of 800 mT.
- The smallest mean relative change of the particle gyration radius was obtained for a beam shift of 30 mm. E×B drifts experienced by medium and high energetic protons increase considerably if the proton beam is shifted.

Finding suggest that a measurement of decay protons might be feasible in a detection setup composed of the field degrader if a magnetic field of 800 mT is considered. Protons follow trajectories closer to the axis of symmetry z, where normal electric fields and relative changes of the electric field within one particle gyration are small. However, further adjustments of the field degrader are required to eliminate Penning traps present above the grounded entrance ring. Additionally, superconducting coils are required for the generation of the strong magnetic field. This increases manufacturing costs considerably.

Promising results have also been achieved for the field degrader used in combination with a double wire grid system. The mean drift distance experienced by protons of kinetic energy 10 eV is below 2 mm for all initial particle pitch angles. However, non-adiabatic effects remain significant for low energetic protons with small initial pitch angles. Further optimizations of the wire grids and the surface potential applied at the grids are required to eliminate Penning traps present above the the individual wires.

Chapter 6

Conclusions and Outlook

The free neutron beta decay, described in the framework of the Standard Model of particle physics (SM), is a useful tool to test the weak interaction and to set limits on various extensions of the SM. A variety of precision experiments have been designed to measure several parameters of the decay. NoMoS is a new experiment which aims to perform precise measurements of the spectra of the charged decay products (electrons and protons) and to determine the angular coefficient a and Fierz interference term b (Section 2.1). The charged decay particles are separated according to their momentum prior to detection using the R×B drift effect present in curved magnetic fields. The resulting drift distance spectra are than measured on spatially resolving detectors. An overview of the experimental setup was given in Section 3.1. Protons emerge from the neutron decay with a maximum kinetic energy of 751 eV and need to be post-accelerated to higher energies to produce a detectable signal in the sensor. The required electric field is provided by the high voltage post-acceleration electrode. The focus of this thesis were studies of multiple electrode designs and of systematic effects induced by the electrode for the simultaneous and single measurement of electrons and protons, which should serve as a base for future design studies.

The post-acceleration electrode introduces systematic effects which need to be investigated and understood to make a measurement of the decay particles feasible and to achieve the desired measurement sensitivity. An overview of such effects and requirements to the electrode design were given in Section 3.2. Two crucial factors in the design of the post-acceleration electrode are the adiabatic transport of the decay particles inside the experiment and the suppression of E×B drift effects. The latter might either lead to a detection of protons at detector positions which are not representative of the given proton energy or protons might even miss the sensor. Investigations of systematic effects rely on detailed numeric simulations of the electrostatic potential and electric field generated by the post-acceleration electrode and on particle-tracking simulations. The methods employed for the various simulations were described in Section 3.3.

The NoMoS experiment enables multiple options for the measurement of the decay electrons and protons. The charged decay particles can be measured either simultaneously or independently. Two detection setups for the simultaneous measurement of electrons and protons were proposed in Chapter 4. In these two setups, electrons and protons are either measured on a common detector surface (setup A, see Fig. 4.1) or on individual sensors which are spatially separated (setup B, see Fig. 4.3). Cylinder electrodes have been considered for the proton post-acceleration in both setups. The electrode and the proton detector are operated at a common surface potential U_{A} (-15 kV) in both setups while the electron sensor is either operated at potential U_{A} (-15 kV) or connected to ground potential in setup A and B, respectively. Further geometrical electrode parameters are described in Section 4.2. Results have shown that a simultaneous measurement of the charged decay particles is difficult to achieve. It was found that the electric fields induced by the two cylinder electrodes are non-uniform and decay protons experience significant E×B

drifts. Normal electric fields vanish at the central axis z and increase at larger distances from the axis in the axially symmetric setup A. In setup B, normal electric fields increase with the distance from the central electrode axis. Approximations of the E×B drift distance $D_{\mathrm{E\times B}}$ for the proton spectrum described in Fig. 4.17 (for a magnetic field of 220 mT) have shown that low and medium energetic protons experience smaller E×B drifts (≤ 1 cm) in setup A. This is due to lower normal electric fields experienced by these protons, which enter the detection region closer to the central axis z (which coincides with the central electrode axis). In setup B, strong normal electric fields are induced by the grounded electron detector. This causes significant drifts of low energetic protons. High energetic protons cover regions of strong normal electric fields and drift by significant amounts in both setups. The drift experienced by a 750 eV proton was estimated (overestimation) to about 3 cm and 2 cm in setup A and B, respectively.

Multiple geometrical and electrical parameters of the two detection setups have been studied for the reduction of E×B drift effects. In setup A it was found that the proton beam and, thus, the proton detector can be shifted in negative direction y to reduce mean drifts experienced by protons. Drifts experienced by medium and high energetic protons decrease significantly if the beam is shifted by 3 cm such that protons with an initial kinetic energy of 400 eV, which are most abundant, enter the detection region on-axis. In such a setup, drifts experienced by protons of 400 eV are suppressed, while protons of energy 750 eV drift by about 2 cm.

In setup B, results have shown that a large axial distance between the electrode and the grounded electron sensor is required to minimize drifts experienced by low energetic protons. It was found that drifts experienced by a proton of 50 eV can be considerably reduced from about 5 cm to 1 cm when the distance between the electrode entrance and electron detector is increased from 10 cm (initial setup) to 50 cm. This setup adjustment comes with an additional advantage: the Penning trap, present both in the path of decay electrons and protons when the grounded electron detector is located at a small distance from the electrode entrance, vanishes.

Studies of E×B drift effects in dependence of the post-acceleration potential applied at the electrode and of the magnetic field used to guide the decay particles have shown that small post-acceleration potentials or large magnetic fields are required to suppress drift effects. To avoid the requirement of large magnetic fields, a small post-acceleration potential $|U_{\mathrm{A}}| < -5$ kV can be considered to reduce E×B drifts below 1.5 cm and 3 cm for all protons in setups A and B, respectively. If large post-acceleration potentials are required for the proton detection, magnetic fields larger than 400 mT should be considered to suppress E×B drift effects. Further adjustments of the post-acceleration electrodes in setups A and B are required to suppress systematic effects and to fulfill all requirements to the electrode design.

For the individual measurement of decay protons, two post-acceleration electrodes, cylinder (Fig. 5.2) and field degrader (Fig. 5.3), were proposed in Chapter 5 and systematic effects induced by the electrodes have been studied. The geometry of the detection region is axially symmetric in both setups. Tracking-simulations have shown that protons experience large electric field gradients within one gyration period in both setups. This makes the particle transport non-adiabatic, especially that of low energetic protons with small initial pitch angles. Such protons enter the detection region off the central axis z and follow trajectories in regions of non-uniform electric fields. Additionally, low and high energetic particles experience significant E×B drifts as they gyrate towards the sensor in both setups. Non-adiabatic effects are significantly smaller when the protons are accelerated by the field degrader, while the opposite holds for E×B drift effects. Both systematic effects additionally show a strong dependence on the initial pitch and phase angles of the decay protons. However, variations of non-adiabatic effects and E×B drifts with the initial phase angle are significantly smaller in the field degrader setup, since the electric field induced by this electrode is more homogeneous.

Although multiple parameters of the cylinder electrode, such as the electrode diameter or the post-acceleration potential applied at the electrode, can be adjusted to reduce non-adiabatic

effects, effects remain significant compared to the field degrader. E×B drifts and phase angle variations thereof decrease considerably if the post-acceleration potential $|U_{\mathrm{A}}|$ applied at the cylinder electrode is decreased from 15 kV to 5 kV. In such a setup, drifts experienced by 10 eV and 750 eV protons are reduced from 8 mm and 7.5 mm to about 5 mm and 3 mm.

For the reduction of non-adiabatic effects in the field degrader setup it was found that a large number of electrode rings combined with a small increment of the surface potential applied at subsequent rings is required. Alternatively, a large magnetic field (> 400 mT) and, thus, a narrower proton beam are required to suppress non-adiabatic effects. These adjustments to the field degrader have been found useful also in the reduction of E×B drifts experienced by the decay protons as they gyrate towards the sensor. Drifts experienced by protons of initial kinetic energy 10 eV and 750 eV are reduced from 12.5 mm to about 8 mm and 9 mm when the number of electrode rings is increased from 11 to 21 (see setups 1 and 3 in Table C.1 for the corresponding electrical setup). An increase of the magnetic field (corresponding to a decrease of the proton beam size) to 800 mT leads to the suppression of E×B drift effects, independent on the initial particle energy or pitch angle.

One optional feature of the field degrader is the circular wire grid which can be attached at the electrode entrance. Such an electrode has shown multiple benefits. It can be used to obtain a more homogeneous electric field inside the electrode, to shield the detection region from large electrostatic potentials and to minimize E×B drift effects and their dependence on the initial proton energy and pitch angle. However, a careful design of the wire grid field degrader is required to avoid large electric fields in the wire plane and the formation of Penning traps in regions covered by the decay protons. Promising results have been obtained for a field degrader composed of 12 individual rings in combination with a double wire grid system (see setup 3 in Table C.5 for the electrical setup) in the reduction of E×B drift effects. Drifts experienced by the decay protons when accelerated by this electrode are in the order of 2 mm. The maximum tolerated E×B drift of the decay protons mainly depends on the detector technology used for the proton measurement and on its spatial resolution. Further adjustments of this electrode are, however, required to minimize the dependence of the E×B drifts on the initial particle phase angle and to suppress non-adiabatic effects.

Results suggest that a field degrader combined with a double wire grid system might be used to make a measurement of the decay protons in a low magnetic field environment feasible. One advantage of low magnetic fields are reduced manufacturing costs. A wire grid field degrader might additionally enable a simultaneous measurement of the decay electrons and protons. Alternatively, a simple field degrader and a narrow particle beam might be considered for the simultaneous measurement of the decay particles to suppress non-adiabatic effects and E×B drifts. This might constitute the object of future investigations.

Outlook

In Chapter 5, we proposed a cylinder electrode made of a resistive foil which generates a similar electric field to the field degrader inside the detection region. Due to software restrictions, particle-tracking simulations were not performed for the resistive cylinder in this thesis. Future work should include such simulations to evaluate the adiabatic particle transport and E×B drifts effects for both the single and simultaneous measurement of the decay particles.

For the simultaneous measurement of electrons and protons, the resistive cylinder electrode might be used in combination with a wire grid to obtain a homogeneous electric field inside the electrode and to shield the electron detector in setup B from large electrostatic potentials and electric fields and, thus, eliminate the Penning trap present at the sensor. Alternatively, the surface potential applied to the electron detector might be chosen according to the electrostatic potential induced by the electrode in the sensor plane. Such an adjustment does, however,

affect the number of detected electrons, since a fraction of electrons might be reflected by the electrostatic potential.

Studies performed for the cylinder electrode have shown that a small electrode diameter is required to obtain a homogeneous electrostatic potential in the vicinity of the proton sensor, while the opposite hold for larger distances from the sensor. To balance effects in these two regions and improve the overall potential homogeneity, a conical electrode might be considered.

Although promising results have been achieved using the field degrader, further optimizations of the electrode are required to make a measurement of the decay protons feasible. We propose multiple aspects of the field degrader which should be considered in future investigations, both in the context of an individual and a simultaneous measurement of the decay particles:

- Proton post-acceleration potential: Studies of the adiabatic particle transport and of $E \times B$ drift effects performed for the cylinder electrode have shown that effects increase with the square root of the post-acceleration potential applied at the electrode. Similar studies should be conducted for the field degrader. A low post-acceleration potential might also increase the fraction of detected electrons in a simultaneous particle measurement, since less electrons might be reflected by the electrostatic potential.

- Surface potential applied at the entrance ring and the wire grid: It was found that a Penning trap is present above the electrode entrance ring (and at the wires) when the ring is operated at ground potential. Investigations of the Penning trap depth for multiple surface potentials of the entrance ring should be considered in future studies.

- Wire grid shape: Due to software limitations, studies presented in this thesis only include circular wire grids. Future work should consider multiple shapes of the wire grid (e.g., rectangular grid) and their influence on the decay protons.

- Distance between consecutive electrode rings: Studies performed in this thesis consider only equidistant electrode rings. The electrostatic potential and electric field induced by the electrode might be considerably affected by this electrode parameter. The distance between two electrode rings should be, however, large enough to avoid strong electric fields between the rings.

- Number of wires and wire diameter: One key aspect in the wire grid design is the transmissibility which is in first order determined by the area covered by the wires. Results have shown that a sparse wire grid is required to obtain a more homogeneous electrostatic potential in the wire plane. The wire diameter might affect the electric field strength at the wires. Future studies should investigate the influence of the wire diameter and the wire grid density on the adiabatic particle transport and $E \times B$ drift effects.

- Field emission studies: Sharp edges should be avoided in the design of the electrode to avoid the emission of secondary electrons and vacuum breakdown.

Studies presented in this thesis were performed for a fixed setup of the vacuum tube. The electrostatic potential and electric field generated by the electrode inside the detection region is affected, among other parameters, by the grounded vaccum tube. Investigations of systematic effects introduced by the post-acceleration electrode should be conducted for various diameters of the grounded vacuum tube. A wider vacuum tube enables the construction of a wider electrode. This might be a useful parameter for the suppression of multiple systematic effects, especially in the simultaneous measurement of the decay particles.

Ultimately, future simulations should be conducted in a more realistic setup including

- the electrode fixation system and insulators,

- a more realistic magnetic field environment in the detection region,
- the R$\times$B drift region and
- the exact drift distance spectra obtained after the particles have drifted in the R$\times$B drift region.

Appendix A

E×B Drift

This appendix contains the derivation of the analytical distance $D_{\mathrm{E\times B}}$ by which charged particles drift due to non-aligned electric and magnetic fields.

An approximation of the drift distance $D_{\mathrm{E\times B}}$ can be derived by integration of $\boldsymbol{v}_{\mathrm{E\times B}}$ (see Eq. (2.11)) over a time interval $[t_0, t_1]$, assuming that the drift velocity is constant. For simplicity, a magnetic field B which points in the direction of the central axis z

$$\boldsymbol{B} = B_{\mathrm{z}} \cdot \hat{\mathbf{e}}_z \tag{A.1}$$

and an electric field E

$$\boldsymbol{E} = E_{\mathrm{r}} \cdot \hat{\mathbf{e}}_y + E_{\mathrm{z}} \cdot \hat{\mathbf{e}}_z, \tag{A.2}$$

are considered. Here, $\hat{\mathbf{e}}_{\mathbf{i}}$ denote unit vectors. The drift velocity $\boldsymbol{v}_{\mathrm{E\times B}}$ can be written a

$$\boldsymbol{v}_{\mathrm{E\times B}} = c \cdot \frac{E_{\mathrm{r}}}{B_{\mathrm{z}}} \cdot \hat{\mathbf{e}}_x. \tag{A.3}$$

A charged particle of mass m moving in this electromagnetic field with a pitch angle $\theta_0 = 0°$ drifts by the distance

$$\begin{aligned} D_{\mathrm{E\times B}} &= c \cdot \int_{t_0}^{t_1} \boldsymbol{v}_{\mathrm{E\times B}} dt \\ &= c \cdot \frac{E_{\mathrm{r}}}{B_{\mathrm{z}}} \cdot \Delta t \cdot \hat{\mathbf{e}}_x = c \cdot \frac{E_{\mathrm{r}}}{B_{\mathrm{z}}} \cdot \frac{\Delta s}{v_{\parallel}} \cdot \hat{\mathbf{e}}_x, \end{aligned} \tag{A.4}$$

in the time interval $\Delta t = t_1 - t_0$ over the distance $\Delta s = \Delta t \cdot v_{\parallel}$ in the direction of the magnetic field vector $\boldsymbol{B}$. The longitudinal particle velocity is denoted by $v_{\parallel}$[1] and is assumed to not be significantly affected by E×B drift effects. To obtain the drift distance, an expression for the particle velocity $v_{\parallel}$ is required. In the following, a particle pitch angle θ of zero is assumed. The absolute energy of a particle moving from a region of electrostatic potential U_0 to a region of potential U is conserved

$$T_{\mathrm{p}} + V_{\mathrm{p}} = T_{\mathrm{p}} + q \cdot U = T_0 + q \cdot U_0 = T_0 + V_0. \tag{A.5}$$

Here, T_{p} and V_{p} denote the final kinetic and potential energy of the particle and T_0 and V_0 represent the initial particle kinetic and potential energy, respectively. Solving for the final kinetic energy T_{p} yields

$$T_{\mathrm{p}} = T_0 - q \cdot (U - U_0) = \frac{1}{2} m v_{\parallel}^2. \tag{A.6}$$

[1] Since the drift distance is derived for a particle with initial pitch angle 0°, the particle transversal velocity $v_{\perp}$ is zero.

The longitudinal velocity component $v_{\parallel}$ can be written as

$$v_{\parallel} = \sqrt{\frac{2[T_0 - e(U - U_0)]}{m}} \tag{A.7}$$

and Eq. (A.4) yields

$$D_{\mathrm{E\times B}} = c \cdot \frac{1}{B_{\mathrm{z}}} \cdot \frac{E_{\mathrm{r}}}{\sqrt{\frac{2[T_0 - q(U-U_0)]}{m}}} \cdot \Delta s \cdot \hat{\mathbf{e}}_x. \tag{A.8}$$

Appendix B

Particle-Tracking Simulations

This appendix contains descriptions of the proton initialization in particle-tracking simulations (Appendix B.1) and of the routines used for data post-processing (Appendix B.2).

B.1 Particle Initialization

Particle-tracking simulations presented in this thesis were performed using multiple software packages developed by F. Glück. A comprehensive description of the software and its methods is provided in [23]. In the following, parameters which are required for the initialization of tracking-simulations performed for this thesis are described.

The following input parameters, which are stored in the file `settings.ini`, are required to initialize the trajectory computation using `Maintraj.cc`:

`r_start` (cm)	radial coordinate of the particle starting position $r_{\mathrm{E\times B}}$
`z_a`, `z_b`, `z_step` (m)	axial coordinate of the particle starting position z in the interval $[z_{\mathrm{a}},\, z_{\mathrm{b}}]$ with a step size z_{step}
`T_start` (eV)	initial particle kinetic energy T
`phi_a`, `phi_b`, `phi_step` (°)	initial particle phase angle φ in the interval $[\varphi_{\mathrm{a}},\, \varphi_{\mathrm{b}}]$ with step size φ_{step}
`theta_a`, `theta_b`, `theta_step` (°)	initial particle pitch angle θ in the interval $[\theta_{\mathrm{a}},\, \theta_{\mathrm{b}}]$ whit a step size θ_{step}
`efield`	scaling factor for the electric field: off (0) or on (1)
`gc`	boolean describing the method used to initialize the starting position

Two methods are available for the initialization of the proton starting position using the parameters `r_start` and `gc`:

- **`gc` = 0**: The parameter `r_start` denotes the radius of a circle centered at the axis of symmetry z. The starting position of a proton is determined by:

$$x_{\mathrm{start}} = r_{\mathrm{start}} \cos(\delta), \tag{B.1}$$

$$y_{\mathrm{start}} = r_{\mathrm{start}} \sin(\delta), \tag{B.2}$$

$$z_{\mathrm{start}} = z_{\mathrm{a}}. \tag{B.3}$$

- `gc` = 1: The position of the particle guiding center at the start of the trajectory is determined by $P_{\mathrm{gc}} = (r_{\mathrm{start}}, 0, z_{\mathrm{start}})$. To construct the starting position of a proton, the particle gyration radius r_{g} is first determined at position P_{gc} using the initial particle properties defined in the initialization file and the local magnetic field. The coordinates at which a proton of initial phase angle φ_0 is initialized are determined using:

$$x_{\mathrm{start}} = r_{\mathrm{start}} + r_{\mathrm{g}} \cos(\varphi_0), \tag{B.4}$$

$$y_{\mathrm{start}} = r_{\mathrm{g}} \sin(\varphi_0), \tag{B.5}$$

$$z_{\mathrm{start}} = z_{\mathrm{a}}. \tag{B.6}$$

In this thesis, tracking-simulations are performed for a given electrode and coil geometry for multiple spatial distributions of the proton drift distance spectrum both in the absence (`efield` = 0) and the presence (`efield` = 1) of electric fields. The axial coordinate of the initial particle position `z_a` is chosen to coincide with the axial position z where the magnetic field generated by the coil reaches a maximum.

B.2 Data Post-Processing

Output Files

The cartesian coordinates of the particle position are written to file after each Runge-Kutta step together with multiple properties of the tracked particle and of the electromagnetic field environment. The output is divided into multiple files as follows:

- `simfile`: contains the initial parameters of each tracked proton described in the previous section and the total number of Runge-Kutta steps.
- `trajfile`: contains various particle properties, such as position, velocity and kinetic erergy and properties of the electromagnetic field environment which are stored after each Runge-Kutta step.
- `detfile`: contains the same parameters as the `trajfile`, however, only evaluated at the last Runge-Kutta step of the particle trajectory.

Post-processing

Particle-tracking simulation are performed for studies of E×B drift effects and of the adiabatic transport of decay protons. Using the programs `trajanalyzed.cc` and `detanalyzed.cc`, the longitudinal kinetic energy and pitch angle of tracked protons is calculated from the parameters stored into the files `trajfile.txt` and `detfile.txt` in the adiabatic approximation (see Section 2.2.3). These are than used to compute absolute and relative variations of the longitudinal proton kinetic energy and pitch angle according to tracking and those obtained in the adiabatic approximation. Additionally, the particle gyration radius and relative deviations thereof (see Section 3.2.1) are evaluated at every point of the trajectory using Eq. (2.5).

For the computation of the E×B drift distance $D^{\mathrm{gc}}_{\mathrm{E\times B}}$ of the particle guiding center as described in Section 3.2.3, the position of the guiding center

$$\boldsymbol{G} = \boldsymbol{x} - r_{\mathrm{g}} \frac{\boldsymbol{v} \times \boldsymbol{B}}{\|\boldsymbol{v} \times \boldsymbol{B}\|} \tag{B.7}$$

is calculated at the last step of the particle trajectory using `detanalyzed.cc`. Here, $\boldsymbol{x}$ and $\boldsymbol{v}$ denote the final particle position and velocity vector, respectively, and the particle gyration radius

is represented by r_{g}. The magnetic field vector is denoted by $\boldsymbol{B}$. The magnetic field inside the detection region of NoMoS is designed to be predominantly aligned in the direction of axis z, thus, $\boldsymbol{B} = (0, 0, b_{\mathrm{z}})$. This yields

$$\boldsymbol{v} \times \boldsymbol{B} = b_{\mathrm{z}} \begin{pmatrix} v_{\mathrm{y}} \\ -v_{\mathrm{x}} \\ 0 \end{pmatrix} \tag{B.8}$$

and

$$\|\boldsymbol{v} \times \boldsymbol{B}\| = b_{\mathrm{z}} \cdot \sqrt{v_{\mathrm{x}}^2 + v_{\mathrm{y}}^2}. \tag{B.9}$$

Inserting Eq. (B.8) and Eq. (B.9) in Eq. (B.7) yields

$$\boldsymbol{G} = \boldsymbol{x} - \frac{r_{\mathrm{g}}}{\sqrt{v_{\mathrm{x}}^2 + v_{\mathrm{y}}^2}} \begin{pmatrix} v_{\mathrm{y}} \\ -v_{\mathrm{x}} \\ 0 \end{pmatrix}. \tag{B.10}$$

Appendix C

Electrode Setups

This appendix lists various setups of the field degrader with and without a wire grid system considered in Chapter 5. The following holds for all electrode setups. The inner and outer electrode diameter are fixed in all setups to 24 cm and 28 cm, respectively. The distance between two subsequent electrode rings is $d_{\mathrm{n}} = 2\,\mathrm{cm}$. The surface potential applied at individual electrode rings increases in steps of ΔU from the electrode end plate ($-15\,\mathrm{kV}$) towards the entrance ring ($0\,\mathrm{kV}$).

C.1 Field Degrader

Field degrader setups considered in Chapter 5 are listed in Table C.1.

Table C.1: Field degrader setups: The electrode is composed of N rings and has a length L. The surface potential applied at individual rings surface. Note that in Chapter 5 setup 1 is referred to as the standard configuration of the field degrader.

	Setup		
Description	1	2	3
Number of rings N	11	16	21
Length L (cm)	20	30	40
Potential Step ΔU (kV)	1.50	1.00	0.75

C.2 Wire Grid Field Degrader

C.2.1 Single Wire Grid

Setups of the wire grid field degrader considered in Chapter 5 are listed in Table C.2. The wire grid is composed of 22 equidistant ($d_{\mathrm{wire}} = 5.14\,\mathrm{mm}$) circular wires of diameter $D_{\mathrm{wire}} = 200\,\mu\mathrm{m}$ and is connected to ground potential.

Table C.2: Setups of the wire grid field degrader: The electrode is composed of N rings and has a length L. The surface potential applied at individual rings surface. Note that in Chapter 5 setup 1 is referred to as the standard configuration of the field degrader.

	Setup		
Description	1	2	3
Number of rings N	11	16	21
Length L (cm)	20	30	40
Potential Step ΔU (kV)	1.50	1.00	0.75

C.2.2 Double Wire Grid

Multiple setups of the field degrader with a double wire grid system considered in Chapter 5 are listed in Tables C.3 to C.5. The two wire grids have identical geometrical properties. These corresponds to the ones described in Appendix C.2.1. The two wire grids are attached at the electrode entrance and at the subsequent ring, respectively.

Table C.3: Setups of the field degrader with a double wire grid system: The electrode is composed of multiple rings $\mathrm{R_i}$ each operated at a surface U_i. Electrode rings are labeled as in the numbering scheme considered in Fig. 5.3. The surface potential applied at the the two wire grids is highlighted in blue.

	Setup			
	1	2	3	4
Ring ID	Surface Potential U_i (kV)			
1	−15.00	−15.00	−15.00	−15.00
2	−13.50	−13.50	−13.50	−13.50
3	−12.00	−12.00	−12.00	−12.00
4	−10.50	−10.50	−10.50	−10.50
5	−9.00	−9.00	−9.00	−9.00
6	−7.50	−7.50	−7.50	−7.50
7	−6.00	−6.00	−6.00	−6.00
8	−4.50	−4.50	−4.50	−4.50
9	−3.00	−3.00	−3.00	−3.00
10	−1.50	−1.50	−1.50	−1.50
11	−0.005	−0.01	−0.05	−0.10
12	0.00	0.00	0.00	0.00

Table C.4: Setups of the field degrader with a double wire grid system: The electrode is composed of multiple rings R_i each operated at a surface U_i. Electrode rings are labeled as in the numbering scheme considered in Fig. 5.3. The surface potential applied at the the two wire grids is highlighted in blue.

	Setup													
	5	6	7	8	9	10	11	12	13	14	15	16	17	18
Ring ID	Surface Potential U_i (kV)													
1	−15.00	−15.00	−15.00	−15.00	−15.00	−15.00	−15.00	−15.00	−15.00	−15.00	−15.00	−15.00	−15.00	−15.00
2	−13.50	−13.50	−13.50	−13.50	−13.50	−13.50	−13.50	−13.50	−13.50	−13.50	−13.50	−13.50	−13.50	−13.50
3	−12.00	−12.00	−12.00	−12.00	−12.00	−12.00	−12.00	−12.00	−12.00	−12.00	−12.00	−12.00	−12.00	−12.00
4	−10.50	−10.50	−10.50	−10.50	−10.50	−10.50	−10.50	−10.50	−10.50	−10.50	−10.50	−10.50	−10.50	−10.50
5	−9.00	−9.00	−9.00	−9.00	−9.00	−9.00	−9.00	−9.00	−9.00	−9.00	−9.00	−9.00	−9.00	−9.00
6	−7.50	−7.50	−7.50	−7.50	−7.50	−7.50	−7.50	−7.50	−7.50	−7.50	−7.50	−7.50	−7.50	−7.50
7	−6.00	−6.00	−6.00	−6.00	−6.00	−6.00	−6.00	−6.00	−6.00	−6.00	−6.00	−6.00	−6.00	−6.00
8	−4.50	−4.50	−4.50	−4.50	−4.50	−4.50	−4.50	−4.50	−4.50	−4.50	−4.50	−4.50	−4.50	−4.50
9	−3.00	−3.00	−3.00	−3.00	−3.00	−3.00	−3.00	−3.00	−3.00	−3.00	−3.00	−3.00	−3.00	−3.00
10	−1.50	−1.50	−1.50	−1.50	−1.50	−1.50	−1.50	−1.50	−1.50	−1.50	−1.50	−1.50	−1.50	−1.50
11	−0.01	−0.05	−0.10	−0.30	−0.75	−0.05	−0.10	−0.30	−0.75	−0.10	−0.30	−0.75	−0.30	−0.75
12	−0.005	−0.005	−0.005	−0.005	−0.005	−0.01	−0.01	−0.01	−0.01	−0.05	−0.05	−0.05	−0.10	−0.10
13	0.00	0.00	0.00	0.00	0.00	0.00	0.00	0.00	0.00	0.00	0.00	0.00	0.00	0.00

Table C.5: Setups of the field degrader with a double wire grid system: The electrode is composed of multiple rings R_i each operated at a surface U_i. Electrode rings are labeled as in the numbering scheme considered in Fig. 5.3. The surface potential applied at the the two wire grids is highlighted in blue.

	Setup														
	19	20	21	22	23	24	25	26	27	28	29	30	31	32	33
Ring ID	Surface Potential U_i (V)														
1	−15.00	−15.00	−15.00	−15.00	−15.00	−15.00	−15.00	−15.00	−15.00	−15.00	−15.00	−15.00	−15.00	−15.00	−15.00
2	−13.50	−13.50	−13.50	−13.50	−13.50	−13.50	−13.50	−13.50	−13.50	−13.50	−13.50	−13.50	−13.50	−13.50	−13.50
3	−12.00	−12.00	−12.00	−12.00	−12.00	−12.00	−12.00	−12.00	−12.00	−12.00	−12.00	−12.00	−12.00	−12.00	−12.00
4	−10.50	−10.50	−10.50	−10.50	−10.50	−10.50	−10.50	−10.50	−10.50	−10.50	−10.50	−10.50	−10.50	−10.50	−10.50
5	−9.00	−9.00	−9.00	−9.00	−9.00	−9.00	−9.00	−9.00	−9.00	−9.00	−9.00	−9.00	−9.00	−9.00	−9.00
6	−7.50	−7.50	−7.50	−7.50	−7.50	−7.50	−7.50	−7.50	−7.50	−7.50	−7.50	−7.50	−7.50	−7.50	−7.50
7	−6.00	−6.00	−6.00	−6.00	−6.00	−6.00	−6.00	−6.00	−6.00	−6.00	−6.00	−6.00	−6.00	−6.00	−6.00
8	−4.50	−4.50	−4.50	−4.50	−4.50	−4.50	−4.50	−4.50	−4.50	−4.50	−4.50	−4.50	−4.50	−4.50	−4.50
9	−3.00	−3.00	−3.00	−3.00	−3.00	−3.00	−3.00	−3.00	−3.00	−3.00	−3.00	−3.00	−3.00	−3.00	−3.00
10	−1.50	−1.50	−1.50	−1.50	−1.50	−1.50	−1.50	−1.50	−1.50	−1.50	−1.50	−1.50	−1.50	−1.50	−1.50
11	−0.10	−0.30	−0.75	−0.30	−0.75	−0.75	−0.30	−0.75	−0.75	−0.75	−0.30	−0.75	−0.75	−0.75	−0.75
12	−0.05	−0.05	−0.05	−0.10	−0.10	−0.30	−0.10	−0.10	−0.30	−0.30	−0.10	−0.10	−0.30	−0.30	−0.30
13	−0.01	−0.01	−0.01	−0.01	−0.01	−0.01	−0.05	−0.05	−0.05	−0.10	−0.05	−0.05	−0.05	−0.10	−0.10
14	−0.005	−0.005	−0.005	−0.005	−0.005	−0.005	−0.005	−0.005	−0.005	−0.005	−0.01	−0.01	−0.01	−0.01	−0.05
15	0.00	0.00	0.00	0.00	0.00	0.00	0.00	0.00	0.00	0.00	0.00	0.00	0.00	0.00	0.00

Appendix D

Additional Plots

This appendix provides additional plots for studies performed in Chapter 5.

D.1 Magnetic Field

The magnetic field used in particle-tracking simulations was designed to fulfill the adiabatic condition $\Delta B/B \ll 1$ within one gyration period of a tracked proton. Fig. D.1 shows the relative change of the magnetic field $\Delta B/B$ along the trajectory of a proton of initial kinetic energy $T_0 = 10\,\text{eV}$, pitch angle $\theta_0 = 45°$ and phase angle $\varphi_0 = 0°$ moving in a magnetic field $B = 220\,\text{mT}$. Here, $\Delta B/B$ is evaluated after each complete gyration of the proton. Results show that variations of the magnetic field are well below $1\,\%$. There are no evaluation points beyond the electrode entrance since the proton does not complete a gyration inside the electrode anymore (see Section 5.4).

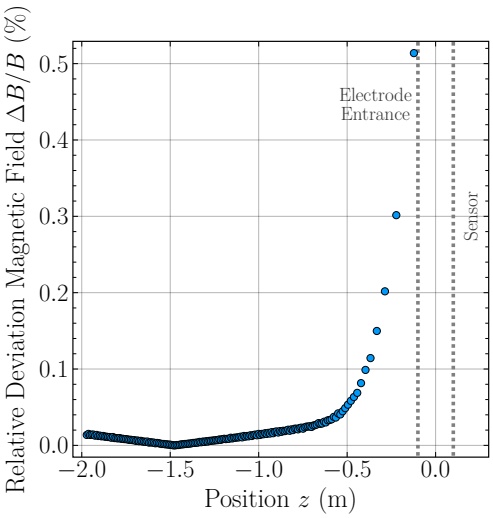


Figure D.1: Relative deviation of the magnetic field $\Delta B/B$ experienced by a proton within one gyration period. Input: $T_0 = 10\,\text{eV}$, $\theta_0 = 45°$, $\varphi_0 = 0°$, $B = 220\,\text{mT}$.

D.2 Cylinder Electrode

This section provides additional plots for studies performed in Section 5.4.1 which consider variations of the post-acceleration potential U_A applied at the cylinder electrode. The electrode has diameter $D = 24\,\text{cm}$ and length $L = 20\,\text{cm}$ (see also Section 5.2).

The electric field norm E experienced by a proton of initial kinetic energy $T_0 = 10\,\text{eV}$, pitch angle $\theta_0 = 45°$ and phase angle $\varphi_0 = 0°$ when accelerated by the electrode is shown in Fig. D.2 for multiple post-acceleration potential $|U_\text{A}|$. The geometrical setup of the cylinder electrode is described in Section 5.2. The maximum of E present at the electrode entrance decreases linearly with the post-acceleration potential.

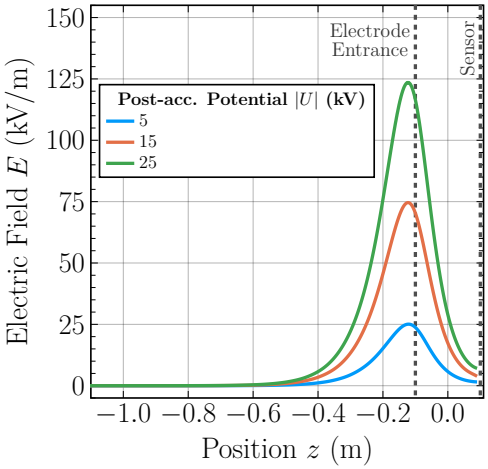
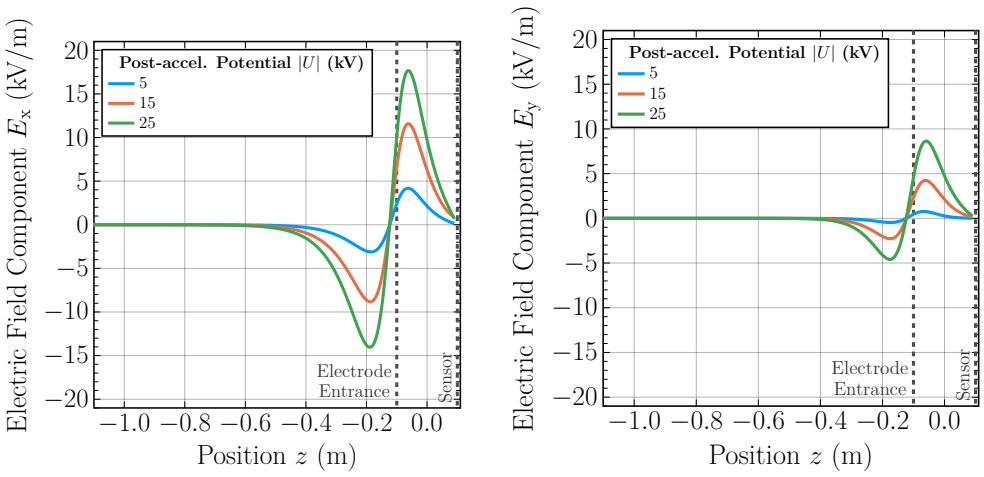


Figure D.2: Electric field norm E experienced by a proton when accelerated by the cylinder electrode operated at the surface potential $|U_\text{A}|$. Input data: $T_0 = 10\,\text{eV}$, $\theta_0 = 45°$, $\varphi_0 = 0°$ and $B = 220\,\text{mT}$.

Fig. D.3 shows the normal electric field components E_x and E_y along the trajectory of a proton of initial kinetic energy $T_0 = 10\,\text{eV}$, pitch angle $\theta_0 = 0°$ and phase angle $\varphi_0 = 0°$ which is accelerated by the cylinder electrode, evaluated for multiple post-acceleration potential $|U_\text{A}|$. A lower post-acceleration potential can be chosen to minimize the normal electric field and, thus, the E×B drifts experienced by the proton as it gyrates towards the sensor (see Fig. 5.36).



(a) (b)

Figure D.3: Normal electric field components E_x and E_y experienced by a proton when accelerated by the cylinder electrode operated at various post-acceleration potentials U_A. Input data: $T_0 = 10\,\text{eV}$, $\theta_0 = 0°$, $\varphi_0 = 0°$ and $B = 220\,\text{mT}$

D.3 Wire Grid Field Degrader

D.3.1 Transmission

The transmission T of a circular wire grid can be obtained from the ratio between the total surface area covered by the wire grid A_{wg} and the interior area A_{el} described by the electrode of inner diameter D_{el} as follows:

$$T = 1 - \frac{A_{\mathrm{wg}}}{A_{\mathrm{el}}}. \tag{D.1}$$

The surface area A_{wg} is determined by the sum over all areas A_i enclosed by each of the N individual wires of diameter D_{wire}:

$$A_{\mathrm{wg}} = \sum_{i=1}^{N} A_i = \sum_{i=1}^{N} \frac{\pi D_{\mathrm{wire}}(2i-1)(D_{\mathrm{el}} + D_{\mathrm{wire}})}{2N+1}. \tag{D.2}$$

For this thesis, a field degrader of inner diameter $D_{\mathrm{el}} = 24\,\mathrm{cm}$ has been considered in combination with a circular wire grid composed of 22 wires of diameter $D_{\mathrm{wire}} = 200\,\mu\mathrm{m}$. The transmission T for this electrode yields $T = 0.964$.

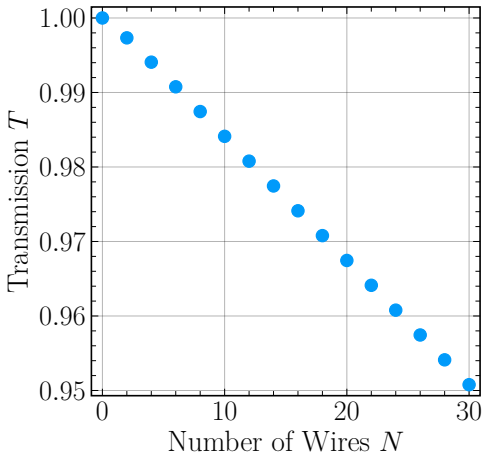


Figure D.4: Transmission T as a function of the number N of concentric grid wires located at the entrance of an electrode of diameter $D_{\mathrm{el}} = 24\,\mathrm{cm}$. Wires have a diameter $D_{\mathrm{wire}} = 0.2\,\mathrm{mm}$.

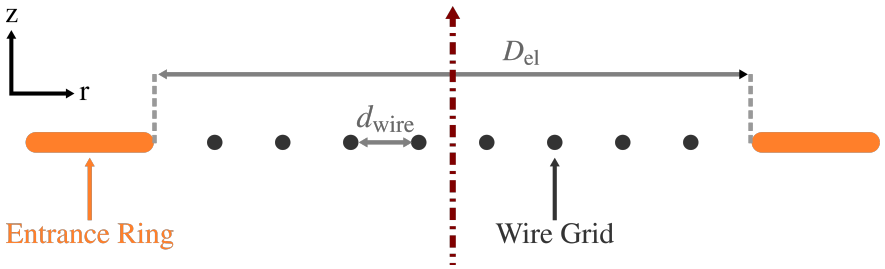


Figure D.5: Sketch of a wire grid composed of N equidistant (d_{wire}), circular wires of diameter D_{wire} which is attached at the entrance ring of a an electrode of inner diameter D_{el}.

D.3.2 Electric Field

The field degrader can be used in combination with a circular wire grid to shield the detection region from large electric fields and to obtain a homogeneous electric field inside the electrode.

This section provides additional plots to studies performed in Chapter 5 using a wire grid field degrader. In the following, a field degrader with an inner and outer diameter of 24 cm and 28 cm is considered. The electrode is composed of 11 rings which are separated by the distance d_{n}. The geometrical setup of the wire grid is described in Appendix C.2.1. Table C.2 gives an overview of the surface potential applied at individual electrode rings.

The orientation of the electric field generated by the wire grid field degrader inside the detection region is shown in Fig. D.6. It can be seen that such an electrode generates a uniform electric field inside the electrode region, especially in the areas covered by decay protons. One disadvantage of the wire grid electrode are, however, strong normal electric fields present at the wires.

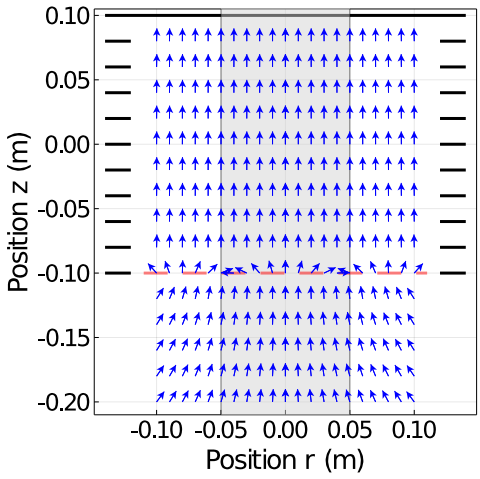
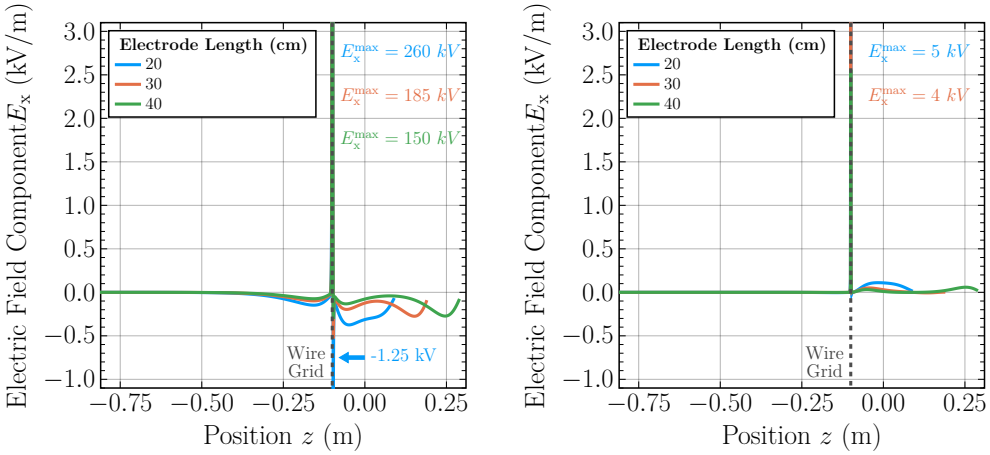


Figure D.6: Electric field E generated by the wire grid field degrader combined with a circular wire grid which is attached at the electrode entrance ($z = -0.10\,\mathrm{m}$). Note that the plot gives information only about the orientation of the electric field and not about its magnitude. The proton beam and the location of the wire grid are marked by the gray area and the dashed, red line, respectively. It can be seen that the electric field at the electrode entrance is strongly inhomogeneous.



(a) (b)

Figure D.7: Normal electric fields E_{x} and E_{y} experienced by a proton when accelerated by the wire grid field degrader of length L of 20 cm, 30 cm and 40 cm (see text for an exact geometrical description). Input data: $T_0 = 10\,\mathrm{eV}$, $\theta_0 = 0°$, $\varphi_0 = 0°$ and $B = 220\,\mathrm{mT}$.

These strong normal field components present at the wire grid can be reduced if a smaller

surface potential is applied at the electrode ring which is subsequent to the entrance ring where the wire grid is attached. Fig. D.7 shows the normal electric fields E_{x} and E_{y} experienced by a proton of initial kinetic energy $T_0 = 10\,\mathrm{eV}$, pitch angle $\theta_0 = 0°$ and phase angle $\varphi_0 = 0°$ when accelerated by a field degrader of length L of 20 cm, 30 cm and 40 cm composed of 11, 16 and 21 rings (see setups 1 to 3 in Table C.2), respectively. The increment of the surface potential applied between two subsequent electrode rings is adapted to the total number of rings according to $U_{\mathrm{A}}/(N-1)$. Here, U_{A} is $-15\,\mathrm{kV}$ and N represents the total number of electrode rings. It can be seen that the normal field experienced by the proton before entering the electrode and at the wire grid decreases for longer electrodes with a smaller increment of the surface potential applied at the electrode rings. Inside the electrode, the absolute values of E_{x} and E_{y} remain well bellow $0.5\,\mathrm{kV/m}$ in the chosen setups.

Bibliography

[1] D. Dubbers and M. G. Schmidt, "The neutron and its role in cosmology and particle physics," *Reviews of Modern Physics*, vol. 83, pp. 1111–1171, Oct. 2011. Publisher: American Physical Society.

[2] S. Baeßler, F. Guardia, M. Borg, F. Glück, W. Heil, G. Konrad, I. Konorov, R. Munoz, G. Petzoldt, D. Rich, M. Simson, Y. Sobolev, H. Wirth, and O. Zimmer, "First measurements with the neutron decay spectrometer aSPECT," *European Physical Journal A*, vol. 38, pp. 17–26, 10 2008.

[3] O. Zimmer, J. Byrne, M. van der Grinten, W. Heil, and F. Glück, "aSPECT – a new spectrometer for the measurement of the angular correlation coefficient a in neutron beta decay," *Nucl. Instrum. Meth. A*, vol. 440, no. 3, pp. 548–556, 2000.

[4] D. Pocanic, R. Alarcon, L. Alonzi, S. Baessler, S. Balascuta, D. Bowman, M. Bychkov, J. Byrne, J. Calarco, V. Cianciolo, C. Crawford, E. Frlez, M. Gericke, G. Greene, R. Grzywacz, V. Gudkov, F. Hersman, A. Klein, J. Martin, and G. Young, "Nab: Measurement principles, apparatus and uncertainties," *Nuclear Instruments and Methods in Physics Research Section A: Accelerators, Spectrometers, Detectors and Associated Equipment*, vol. 611, 10 2008.

[5] Wietfeldt, F.E., Byron, W.A., Collett, B., Darius, G., DeAngelis, C.R., Dewey, M.S., Hassan, M.T., Jones, G., Komives, A., Mendenhall, M.P., Nico, J.S., and Stephenson, E.J., "aCORN: Measuring the electron-antineutrino correlation in neutron beta decay," *EPJ Web Conf.*, vol. 219, p. 04008, 2019.

[6] X. Wang, G. Konrad, and H. Abele, "R×B drift momentum spectrometer with high resolution and large phase space acceptance," *Nucl. Instrum. Meth. A*, vol. 701, pp. 254–261, 2013.

[7] G. Konrad, "NoMoS: Beyond the Standard Model Physics in Neutron Decay," *PoS*, vol. EPS-HEP2015, p. 592, 2015.

[8] R. P. Feynman and M. Gell-Mann, "Theory of the fermi interaction," *Phys. Rev.*, vol. 109, pp. 193–198, Jan 1958.

[9] E. C. G. Sudarshan and R. E. Marshak, "Chirality invariance and the universal fermi interaction," *Phys. Rev.*, vol. 109, pp. 1860–1862, Mar 1958.

[10] "Neutron Decay at the quark level." `https://www.pngegg.com/en/png-oojky`. Accessed: 2020-07-22.

[11] J. D. Jackson, S. B. Treiman, and H. W. Wyld, "Possible tests of time reversal invariance in beta decay," *Phys. Rev.*, vol. 106, pp. 517–521, May 1957.

[12] S. Baeßler, J. D. Bowman, S. Penttilä, and D. Počanić, "New precision measurements of free neutron beta decay with cold neutrons," *Journal of Physics G: Nuclear and Particle Physics*, vol. 41, p. 114003, oct 2014.

[13] P. Zyla *et al.*, "Review of Particle Physics," *Progress of Theoretical and Experimental Physics*, vol. 2020, 08 2020. 083C01.

[14] J. S. Nico, "Neutron beta decay," *Journal of Physics G: Nuclear and Particle Physics*, vol. 36, p. 104001, sep 2009.

[15] A. Ivanov, M. Pitschmann, and N. Troitskaya, "Neutron $\beta-$ decay as a laboratory for testing the standard model," *Physical Review D*, vol. 88, pp. 73002–, 10 2013.

[16] J. D. Jackson, *Classical electrodynamics*. New York, NY: Wiley, 3rd ed. ed., 1999.

[17] F. F. Chen, "Single-Particle Motions," in *Introduction to Plasma Physics and Controlled Fusion*, pp. 19–49, Cham: Springer International Publishing, 2016.

[18] F. Glück, S. Baeßler, J. Byrne, M. Grinten, J. Hartmann, W. Heil, I. Konorov, G. Petzoldt, Y. Sobolev, and O. Zimmer, "The neutron decay retardation spectrometer aSPECT: Electromagnetic design and systematic effects," *European Physical Journal A*, vol. 23, pp. 135–146, 01 2005.

[19] G. Konrad, *Measurement of the Proton Recoil Spectrum in Neutron Beta Decay with the Spectrometer aSPECT: Study of Systematic Effects*. PhD thesis, Mainz U., 08 2011.

[20] D. Moser. PhD thesis, Technische Universität Wien, 2021. In progress.

[21] COMSOL, "Comsol multiphysics® 5.3a." `https://www.comsol.com`.

[22] F. Glück *et al.*, "EM field, tracking and scattering simulations for the KATRIN experiment," *Journal of Physics: Conference Series*, vol. 410, p. 012039, feb 2013.

[23] D. Furse, S. Groh, N. Trost, M. Babutzka, J. P. Barrett, J. Behrens, N. Buzinsky, T. Corona, S. Enomoto, M. Erhard, J. A. Formaggio, F. Glück, F. Harms, F. Heizmann, D. Hilk, W. Käfer, M. Kleesiek, B. Leiber, S. Mertens, N. S. Oblath, P. Renschler, J. Schwarz, P. L. Slocum, N. Wandkowsky, K. Wierman, and M. Zacher, "Kassiopeia: a modern, extensible C++ particle tracking package," *New Journal of Physics*, vol. 19, p. 053012, may 2017.

[24] F. Glück, "Axisymmetric magnetic field calculation with zonal harmonic expansion," *Progress In Electromagnetics Research B*, vol. 32, pp. 351–388, 01 2011.

[25] K. Valerius, *Spektrometeruntergrund und seine Unterdrückung beim KATRIN Experiment*. PhD thesis, Westfälische Wilhelms-Universität Münster.

[26] W. Khalid. PhD thesis, Technische Universität Wien, 2021. In progress.

Acknowledgements

The completion of my thesis would not have been possible without the support and guidance of many people.

First I would like to express my deepest appreciation to my supervisor Prof. Dr. Johann Zmeskal for the patient guidance, encouragement and advice he has provided throughout my time as his student.

I would also like to extend my deepest gratitude to the NoMoS group at the Stefan Meyer Institute of Subatomic Physics. I wish to thank Dr. Gertrud Konrad, who has been an outstanding co-supervisor, for always asking insightful questions and offering invaluable advice which helped me improve. I would like to thank Daniel Moser for always taking his time for numerous scientific discussions and, especially, for proofreading my thesis. Thanks also to Waleed Khalid for providing me with additional simulations which have helped me explain various important aspects in the design of the detection system. Thanks should also go to Dr. Manfred Valentan for his help with programming and other computer related issues and for the introduction to particle detectors. It has been a pleasure to work with you all.

I am also grateful to Dr. Ferenc Glück for providing multiple software packages for electromagnetic field computations and particle-tracking simulations which have been crucial for studies presented in this work.

I would like to thank my parents, brother and grandparents for their continuous support, help and understanding. I am extremely grateful to my parents for giving me the opportunity to move and study abroad. They have always encouraged me to explore new directions in life and to seek my own destiny. This work is dedicated to them.

Lastly, I would like to thank my wonderful partner Daniel for his support and patience which cannot be underestimated. He has always encouraged me to do my best and always helped me in difficult moments.